Научном већу Института за физику у Београду

Предмет: Молба за покретање поступка за избор у звање истраживач сарадник

Молим Научно веће Института за физику у Београду да у складу са Правилником о поступку и начину вредновања и квантитативном исказивању научно-истраживачких резултата истраживача покрене поступак за мој избор у звање истраживач приправник.

У прилогу достављам:

1. мишљење руководиоца лабораторије са предлогом чланова комисије за избор у звање;
2. стручну биографију;
3. преглед научне активности;
4. списак објављених научних радова и других публикација;
5. копије објављених научних радова;
6. уверење о последњем уписаном и овереном семестру на докторским студијама;
7. фотокопије уверења о завршеним основним и мастер студијама на Физичком факултету Универзитета у Београду;
8. потврду о прихватању теме докторске дисертације;

У Београду, 12.10.2021.

С поштовањем,

Сања Ђурђић Мијин

Sanja Đurđić Mijin

Научном већу Института за физику у Београду

Предмет: Мишљење руководиоца лабораторије о избору Сање Ђурђић Мијин у звање истраживач приправник, са предлогом чланова комисије за избор у звање

Сања Ђурђић Мијин, студент докторских студија на Физичком факултету Универзитета у Београду, у Центру за физику чврстог стања и нове материјале Института за физику у Београду запослена је од 03.12.2018. године. Од децембра 2018. до децембра 2019. године била је ангажована на пројекту **„Наноструктурни мултифункционални наноматеријали и нанокомпозити"** (III450018) Министарства просвете, науке и технолошког развоја Републике Србије под руководством академика Зорана В. Поповића. Од августа 2020. ангажована је на PROMIS пројекту „**StrainedFeSC"** (број: 6062656) Фонда за науку Републике Србије под руководством др Ненада Лазаревића.

У звање истраживач приправник изабрана је у децембру 2018. године. У истраживачком раду бави се изучавањем динамике решетке магнетних квази-2Д материјала. С обзиром на то да испуњава све предвиђене услове у складу са Правилником о поступку, начину вредновања и квантитативном исказивању научноистраживачких резултата истраживача МПНТР, сагласан сам са покретањем поступка за избор Сање Ђурђић Мијин у звање истраживач сарадник

За састав комисије за избор Сање Ђурђић Мијин у звање истраживач сарадник предлажем:

1. др Ненада Лазаревића, вишег научног сарадника, Института за физику у Београду
2. др Бојану Вишић, вишег научног сарадника, Института за физику у Београду
3. др Ђорђа Спасојевића, редовног професора Физичког факултета Универзитета у Београду

академик Зоран В. Поповић

_____

научни саветник,
руководилац лабораторије
за физику чврстог стања

Стручна биографија Сање Ђурђић Мијин

Сања Ђурђић Мијин рођења је у Београду 29.09.1993. године. Након завршене основне школе и гиманзије, 2012. године уписује Физички факултет Универзитета у Београд, смер *Примењена и компјутерска физика*, на коме дипломира 2016. године, са просечном оценом 9.57. Након успешно завршених основних студија, исте године уписује мастер студије на Физичом факултету, смер *Теоријска и експерименална физика*. У оквиру пројекта 2015-2-ES01-KA107-022648 програма ERASMUS+ мастер тезу под називом „Компаративна студија поларизоване оптичке емисије из поларних и неполарних квантних тачака у GaN/InGaN наножицама“ ради на Техничком Универзитету у Мадриду, под менторством др Жарка Гачевића, и на Самосталном Универзитету у Мадриду, под менторством др Снежане Лазић. Мастер рад, под менторством др Славице Малетић и коменторством др Снежане Лазић, брани 5. јула 2017. године, чиме завршава мастер студије са просечном оценом 10.00. У фебруару 2018. свој научно-истраживачки рад наставља на Институту за физику у Београду, у Центру за чврсто стање и нове материјале у групи др Зорана В. Поповића. Докторске студије на Физичком факултету у Београду, ужа научна област *Физика кондензоване материје и статистичка физика*, уписује у октобру 2018. године, под менторством др Ненада Лазаревића. На пројекту МПНТР ,,**Наноструктурни мултифункционални наноматеријали и нанокомпозити**“ (III450018) којим је руководио академик Зоран В. Поповић била је ангажована од децембра 2018. до децембра 2019. године. Од августа 2020. године ангажована је на пројекту Фонда за науку Републике Србије ,,**StrainedFeSC**“ (број: 6062656) чији је руководилац др Ненад Лазаревић. У досадашњој каријери Сања Ђурђић Мијин је публиковала 4 научна рада: 1 из категорије М21а и 3 из катерогије М21, од којих је наведена као први аутор на 3 рада, као и саопштења са међународих скупова штампаних у изводу (М34).

Преглед научне активности Сање Ђурђић Мијин

Током докторских студија, под руководством др Ненада Лазаревића, Сања Ђурђић Мијин се бави испитивањем вибрационих особина магнетних квази-2Д материјала методом Раманове спектроскопије.

Успешна синтеза графена при амбијенталним условма 2004. године отворила је потпуно нову област експерименталне физике чврстог стања- квази-2Д материјале. Откриће нових и егзотичних феномена у овој врсти материјала, а који су одсутни код њихових 3Д анологона, заслужно је за неисцрпно интересовање које уживају. Оно што је посебно занимљиво и корисно код ове групе материјала јесте могућност контролисања њихових физичких и хемијских карактеристика применом спољашњих утицаја. Експериментална потврда феромагнетног уређења у квази-2Д ван дер Валсовим материјала значајно је проширила област њихове могуће примене и усмерила интересовање научника ка испитивању магнетног уређења у ново синтетисаним квази-2Д материјалима. У оквиру њеног истраживања, Сања Ђурђић Мијин испитивала је материјале из две велике фамилије квази-2Д материјала – трихалиде прелазних метала и дихалкогениде прелазних метала.

Истраживања у оквиру трихалида прелазних метала фокусирана су испитивање динамике решетке хром-јодида (CrI_3) и ванадијум-јодида (VI_3). Главни резултати ових радова јесу потврда структурног фазног прелаза првог реда у хром-јодиду (из нискотемпературске ромбоедарске $\bar{R}3$ структуре у високотемепратурску моноклиничну *C2/m* структуру), на температури нижој од оне која се помиње у стручној литератури, и краткодометно уређење кристалне структуре VI_3. Додатно, спектри добијени на запреминским кристалима хром-јодида не указују на претходно пријављену коегзистенцију нискотемпературске и високотемпературске фазе. Што се тиче Раманових спектара добијених на ванадијум-јодиду, поларизациона зависност експерименталних фононских мода показала је неслагање са поларизационом зависношћу теоријом предвиђених Раман активних мода за симетрију добијену XRD експериментом. Да би се открио узрок неслагања Рамановог и XRD експеримента, урађен је синхротронски XRD експеримент, чиме је утврђено да кристална решетка VI_3 има различито дугодометно ($\bar{R}3$) и краткодометно уређење ($P\bar{3}1c$).

Резултати добијени на 1T структури тантал-дисулфида, испитиваног дихалкогенида прелазног метала, показали су да електронска Раманова спектроскопија може да се користи као експериментална техника за одређивање Мотовог процепа у материјала у којима долази до метал-изолатор прелаза. Поред потврђеног отварања Мотовог процепа у овом материјалу, на који су сугерисали претходно објављене ARPES студије, у овом раду је по први пут представљана динамика решетке несамерљиве (incommensurate) фазе таласа густине наелектрисања. Како таласи густине наелектрисања представљају још увек необјашњив физички феномен, овај рад покушао је да пружи основу за његово боље разумевање.

Списак публикација Сање Ђурђић Мијин

Радови у међународним часописима изузетних вредности (M21a):

- **S. Djurdjić Mijin**, A.M. Milinda Abeykoon, A. Šolajić, A. Milosavljević, J. Pešić, Yu Liu, C. Petrovic, Z. V. Popović, N. Lazarević*, Short-range order in VI_3,* Inorg Chem. **59** (22):16265-16271 (2020), DOI: 10.1021/acs.inorgchem.0c02060, IF (2019): 4.852, ISSN: 0020-1669

Радови у врхунским међународним часописима (M21):

- **S. Djurdjić Mijin**, A. Šolajić, J. Pešić, M. Šćepanović, Y. Liu, A. Baum, C. Petrovic, N. Lazarević, and Z. V. Popović, Lattice dynamics and phase transition in CrI_3 single crystals, Phys. Rev. **B** 98, 104307 (2018), DOI: 10.1103/PhysRevB.98.104307, IF (2018): 3.736, ISSN: 2469-9950
- A. Milosavljević, A. Šolajić, **S. Djurdjić Mijin**, J. Pešić, B. Višić, Yu Liu, C. Petrovic, N. Lazarević, Z.V. Popović*, Lattice dynamics and phase transitions in $Fe_{3-x}GeTe_2$*, Phys. Rev. **B 99**, 214304 (2019), DOI: 10.1103/PhysRevB.99.214304, IF (2018): 3.736, ISSN: 2469-9950
- **S. Djurdjić Mijin**, A. Baum, J. Bekaert, A. Šolajić, J. Pešić, Y. Liu, Ge He, M. V. Milošević, C. Petrovic, Z. V. Popović, R. Hackl, and N. Lazarević, *Probing charge density wave phases and the Mott transition in 1T−TaS_2 by inelastic light scattering*. Physical Review **B 103**(24), 245133 (2021), DOI: 10.1103/PhysRevB.99.214304, IF (2018): 3.736, ISSN: 2469-9950

Саопштења са међународног скупа штампана у изводу (категорија M34):

- **S. Djurdjić**, A. Šolajić, J. Pešić, M. Šćepanović, Y. Liu, A. Baum, Č. Petrović, N. Lazarević, Z. V. Popović, *Raman Spectroscopy Study on phase transition in CrI_3 single crystals,* Seventeenth Young Researchers Conference – Materials Science and Engineering December 5-7, 2018, Belgrade, Serbia
- **S. Djurdjić Mijin**, A. Šolajić, J. Pešić, M. Šćepanović, Y. Liu, A. Baum, C. Petrovic, N. Lazarević, and Z. V. Popović, *The Vibrational Properties of CrI_3 Single Crystals,* The 20th Symposium on Condensed Matter Physics BOOK OF ABSTRACTS, pp. 21 - 21, Belgrade, 7. - 11. Oct, 2019
- A. Milosavljević, A. Šolajić, **S. Djurdjić Mijin**, J. Pešić, B. Višić, Y. Liu, C. Petrovic, N. Lazarević, Z. V. Popović *Lattice dynamics and phase transitions in $Fe_{3-x}GeTe_2$*, The 20th Symposium on Condensed Matter Physics BOOK OF ABSTRACTS, pp. 84 - 84, Belgrade, 7. - 11. Oct, 2019
- **S. Djurdjić Mijin**, J. Bekaert, A. Šolajić, J. Pešić, Y. Liu, M. V. Milosevic, C. Petrovic, N. Lazarević, and Z. V. Popović, *Probing subsequent charge density waves in 1T-TaS_2 by inelastic light scattering,* Eighteenth Young Researchers Conference – Materials Science and Engineering December 4-6, 2019, Belgrade, Serbia

Lattice dynamics and phase transition in CrI_3 single crystals

S. Djurdjić-Mijin,[1] A. Šolajić,[1] J. Pešić,[1] M. Šćepanović,[1] Y. Liu (刘育),[2] A. Baum,[3,4] C. Petrovic,[2] N. Lazarević,[1] and Z. V. Popović[1,5]

[1]*Center for Solid State Physics and New Materials, Institute of Physics Belgrade, University of Belgrade, Pregrevica 118, 11080 Belgrade, Serbia*

[2]*Condensed Matter Physics and Materials Science Department, Brookhaven National Laboratory, Upton, New York 11973-5000, USA*

[3]*Walther Meissner Institut, Bayerische Akademie der Wissenschaften, 85748 Garching, Germany*

[4]*Fakultät für Physik E23, Technische Universität München, 85748 Garching, Germany*

[5]*Serbian Academy of Sciences and Arts, Knez Mihailova 35, 11000 Belgrade, Serbia*

(Received 9 July 2018; published 18 September 2018)

The vibrational properties of CrI_3 single crystals were investigated using Raman spectroscopy and were analyzed with respect to the changes of the crystal structure. All but one mode are observed for both the low-temperature $R\bar{3}$ and the high-temperature $C2/m$ phase. For all observed modes the energies and symmetries are in good agreement with DFT calculations. The symmetry of a single layer was identified as $p\bar{3}1/m$. In contrast to previous studies we observe the transition from the $R\bar{3}$ to the $C2/m$ phase at 180 K and find no evidence for coexistence of both phases over a wide temperature range.

DOI: 10.1103/PhysRevB.98.104307

I. INTRODUCTION

Two-dimensional layered materials have gained attention due to their unique properties, the potential for a wide spectrum of applications, and the opportunity for the development of functional van der Waals heterostructures. CrI_3 is a member of the chromium-trihalide family which are ferromagnetic semiconductors [1]. Recently they have received significant attention as candidates for the study of magnetic monolayers. The experimental realization of CrI_3 ferromagnetic monolayers [1] motivated further efforts towards their understanding. CrI_3 features electric field controlled magnetism [2] as well as a strong magnetic anisotropy [3,4]. With the main absorption peaks lying in the visible part of the spectrum, it is a great candidate for low-dimensional semiconductor spintronics [5]. In its ground state, CrI_3 is a ferromagnetic semiconductor with a Curie temperature of 61 K [1,6] and a band gap of 1.2 eV [6]. It was demonstrated that the magnetic properties of CrI_3 mono- and bilayers can be controlled by electrostatic doping [2]. Upon cooling, CrI_3 undergoes a phase transition around 220 K from the high-temperature monoclinic ($C2/m$) to the low-temperature rhombohedral ($R\bar{3}$) phase [3,7]. Although the structural phase transition is reported to be first order, it was suggested that the phases may coexist over a wide temperature range [3]. Raman spectroscopy can be of use here due to its capability to simultaneously probe both phases in a phase-separated system [8–10].

A recent theoretical study predicted the energies of all Raman active modes in the low-temperature and high-temperature structure of CrI_3 suggesting a near degeneracy between the A_g and B_g modes in the monoclinic ($C2/m$) structure. Their energies match the energies of E_g modes in the rhombohedral ($R\bar{3}$) structure [7].

In this article we present an experimental and theoretical Raman scattering study of CrI_3 lattice dynamics. In both phases all but one of the respective modes predicted by symmetry were observed. The energies for all modes are in good agreement with the theoretical predictions for the assumed crystal symmetry. Our data suggest that the first-order transition occurs at $T_s \approx 180$ K without evidence for phase coexistence over a wide temperature range.

II. EXPERIMENT AND NUMERICAL METHOD

The preparation of the single crystal CrI_3 sample used in this study is described elsewhere [11]. The Raman scattering experiment was performed using a Tri Vista 557 spectrometer in backscattering micro-Raman configuration with a 1800/1800/2400 groves/mm diffraction grating combination. The 532 nm line of a Coherent Verdi G solid state laser was used for excitation. The direction of the incident light coincides with the crystallographic c axis. The sample was oriented so that its principal axis of the $R\bar{3}$ phase coincides with the x axis of the laboratory system. A KONTI CryoVac continuous helium flow cryostat with a 0.5-mm-thick window was used for measurements at all temperatures under high vacuum (10^{-6} mbar). The sample was cleaved in air before being placed into the cryostat. The obtained Raman spectra were corrected by the Bose factor and analyzed quantitatively by fitting Voigt profiles to the data whereby the Gaussian width $\Gamma_{\text{Gauss}} = 1\ \text{cm}^{-1}$ reflects the resolution of the spectrometer.

The spin polarized density functional theory (DFT) calculations have been performed in the Quantum Espresso (QE) software package [12] using the Perdew-Burke-Ernzehof (PBE) exchange-correlation functional [13] and PAW pseudopotentials [14,15]. The energy cutoffs for the wave functions and the charge density were set to be 85 and 425 Ry, respectively, after convergence tests. For k-point sampling, the Monkhorst-Pack scheme was used with a $8 \times 8 \times 8$ grid centered around the Γ point. Optimization of the atomic positions in the unit cell was performed until the interatomic forces

were smaller than 10^{-6} Ry/Å. To treat the van der Waals (vdW) interactions a Grimme-D2 correction [16] is used in order to include long-ranged forces between the layers, which are not properly captured within LDA or GGA functionals. This way, the parameters are obtained more accurately, especially the interlayer distances. Phonon frequencies were calculated at the Γ point using the linear response method implemented in QE. The phonon energies are compiled in Table III together with the experimental values. The eigenvectors of the Raman active modes for both the low- and high-temperature phase are depicted in Fig. 5 of the Appendix.

III. RESULTS AND DISCUSSION

CrI_3 adopts a rhombohedral $R\bar{3}$ (C_{3i}^2) crystal structure at low temperatures and a monoclinic $C2/m$ (C_{2h}^3) crystal structure at room temperature [3], as shown in Fig. 1. The main difference between the high- and low-temperature crystallographic space groups arises from different stacking sequences with the CrI_3 layers being almost identical. In the rhombohedral structure the Cr atoms in one layer are placed above the center of a hole in the Cr honeycomb net of the two adjacent layers. When crossing the structural phase transition at T_s to the monoclinic structure the layers are displaced along the a direction so that every fourth layer is at the same place as the first one. The interatomic distances, mainly the interlayer distance, and the vdW gap, are slightly changed by the structural transition. The crystallographic parameters for both phases are presented in Table I. The numerically obtained values are in good agreement with reported x-ray diffraction data [11].

The vibrational properties of layered materials are typically dominated by the properties of the single layers composing the crystal. The symmetry of a single layer can be described by one of the 80 diperiodic space groups (DG) obtained by lifting translational invariance in the direction perpendicular to the layer [17]. In the case of CrI_3, the symmetry analysis revealed that the single layer structure is fully captured by the $p\bar{3}1/m$ (D_{3d}^1) diperiodic space group DG71, rather than by $R\bar{3}2/m$ as proposed in Ref. [7].

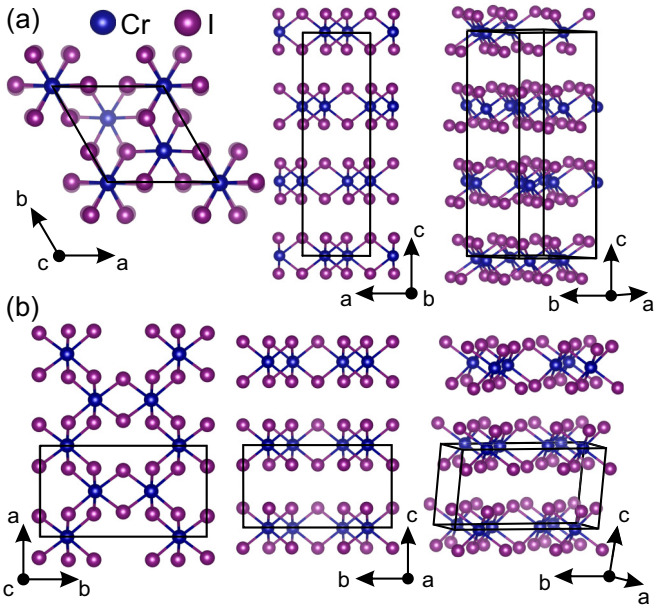

FIG. 1. Schematic representation of (a) the low-temperature $R\bar{3}$ and (b) the high-temperature $C2/m$ crystal structure of CrI_3. Black lines represent unit cells.

TABLE I. Calculated and experimental [11] parameters of the crystallographic unit cell for the low-temperature $R\bar{3}$ and high-temperature $C2/m$ phase of CrI_3.

	Space group $R\bar{3}$		Space group $C2/m$	
T (K)	Calc.	Expt. [11]	Calc.	Expt. [11]
a (Å)	6.87	6.85	6.866	6.6866
b (Å)	6.87	6.85	11.886	11.856
c (Å)	19.81	19.85	6.984	6.966
α (deg)	90	90	90	90
β (deg)	90	90	108.51	108.68
γ (deg)	120	120	90	90

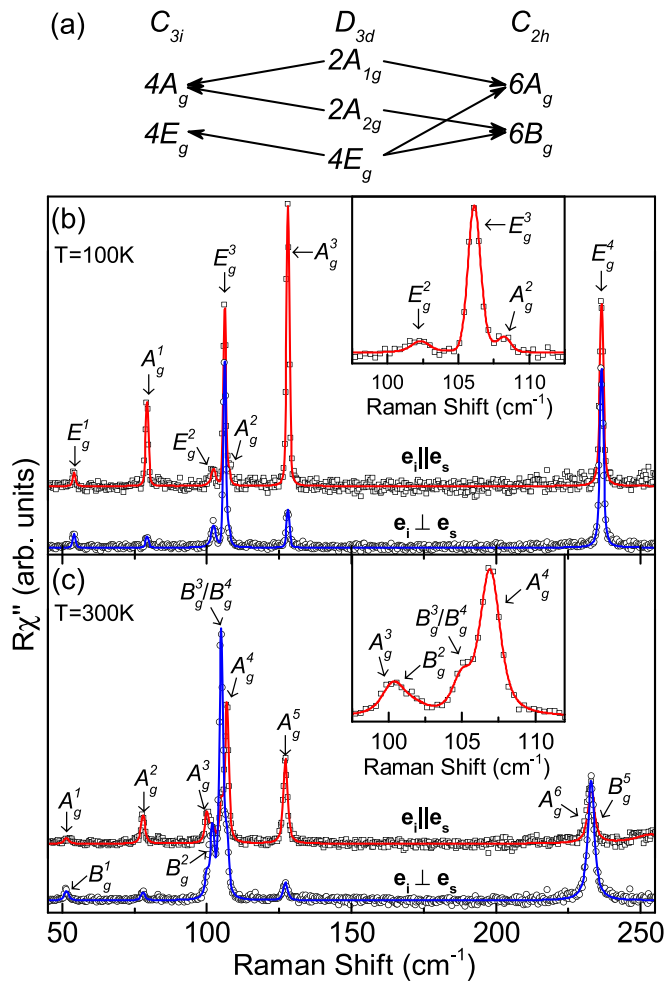

FIG. 2. (a) Compatibility relations for the CrI_3 layer and the crystal symmetries. Raman spectra of (b) the low-temperature $R\bar{3}$ and (c) the high-temperature $C2/m$ crystal structure measured in parallel (open squares) and crossed (open circles) polarization configurations at 100 and 300 K, respectively. Red and blue solid lines represent fits of Voigt profiles to the experimental data.

TABLE II. Wyckoff positions of the two types of atoms and their contributions to the Γ-point phonons for the $R\bar{3}$ and $C2/m$ as well as the $p\bar{3}1/m$ diperiodic space group. The second row shows the Raman tensors for the corresponding space groups.

Space group $R\bar{3}$		Diperiodic space group $p\bar{3}1/m$		Space group: C2/m	
Atoms	Irreducible representations	Atoms	Irreducible representations	Atoms	Irreducible representations
Cr (6c)	$A_g+A_u+E_g+E_u$	Cr (2c)	$A_{2g}+A_{2u}+E_g+E_u$	Cr (4g)	$A_g+A_u+2B_g+2B_u$
I (18f)	$3A_g+3A_u+3E_g+3E_u$	I (6k)	$2A_{1g}+A_{1u}+A_{2g}+2A_{2u}+3E_g+3E_u$	I (4i)	$2A_g+2A_u+B_g+B_u$
				I (8j)	$3A_g+3A_u+3B_g+3B_u$
$A_g=\begin{pmatrix} a & & \\ & a & \\ & & b \end{pmatrix}$		$A_{1g}=\begin{pmatrix} a & & \\ & a & \\ & & b \end{pmatrix}$		$A_g=\begin{pmatrix} a & & d \\ & c & \\ d & & b \end{pmatrix}$	
${}^1E_g=\begin{pmatrix} c & d & e \\ d & -c & f \\ e & f & \end{pmatrix}$	${}^2E_g=\begin{pmatrix} d & -c & -f \\ -c & -d & e \\ -f & e & \end{pmatrix}$	${}^1E_g=\begin{pmatrix} c & & \\ & -c & d \\ & d & \end{pmatrix}$	${}^2E_g=\begin{pmatrix} & -c & -d \\ -c & & \\ -d & e & \end{pmatrix}$	$B_g=\begin{pmatrix} & e & \\ e & & f \\ & f & \end{pmatrix}$	

According to the factor group analysis (FGA) for a single CrI_3 layer, six modes ($2A_{1g}+4E_g$) are expected to be observed in the Raman scattering experiment (see Table II). By stacking the layers the symmetry is reduced and, depending on the stacking sequence, FGA yields a total of eight Raman active modes ($4A_g+4E_g$) for the $R\bar{3}$ and 12 Raman active modes ($6A_g+6B_g$) for the $C2/m$ crystal symmetry. The correlation between layer and crystal symmetries for both cases is shown in Fig. 2(a) [18,19].

Figure 2(b) shows the CrI_3 single crystal Raman spectra measured at 100 K in two scattering channels. According to the selection rules for the rhombohedral crystal structure (Table II) the A_g modes can be observed only in the parallel polarization configuration, whereas the E_g modes appear in both parallel and crossed polarization configurations. Based on the selection rules the peaks at about 78, 108, and 128 cm^{-1} were identified as A_g symmetry modes, whereas the peaks at about 54, 102, 106, and 235 cm^{-1} are assigned as E_g symmetry. The weak observation of the most pronounced A_g modes in crossed polarizations [Fig. 2(b)] is attributed to the leakage due to a slight sample misalignment and/or the presence of defects in the crystal. The energies of all observed modes are compiled in Table III together with the energies predicted by our calculations and by Ref. [7], and are found to be in good agreement for the E_g modes. The discrepancy is slightly larger for the low energy A_g modes. Our calculations in general agree with those from Ref. [7]. The A_g^4 mode of the rhombohedral phase, predicted by calculation to appears at about 195 cm^{-1}, was not observed in the experiment, most likely due to its low intensity.

When the symmetry is lowered in the high-temperature monoclinic $C2/m$ phase [Fig. 2(c)] the E_g modes split into an A_g and a B_g mode each, whereas the rhombohedral A_g^2 and A_g^4 modes are predicted to switch to the monoclinic B_g symmetry. The correspondence of the phonon modes across the phase transition is indicated by the arrows in Table III. The selection rules for $C2/m$ (see Table II) predict that A_g and B_g modes can be observed in both parallel and crossed polarization configurations. Additionally, the sample forms three types of domains which are rotated with respect to each other. We

TABLE III. Phonon symmetries and phonon energies for the low-temperature $R\bar{3}$ and high-temperature $C2/m$ phase of CrI_3. The experimental values were determined at 100 and 300 K, respectively. All calculations were performed at zero temperature. Arrows indicate the correspondence of the phonon modes across the phase transition.

Space group $R\bar{3}$					Space group C2/m			
Symm.	Expt. (cm^{-1})	Calc. (cm^{-1})	Calc. (cm^{-1}) [7]		Symm.	Expt. (cm^{-1})	Calc. (cm^{-1})	Calc. [7] (cm^{-1})
E_g^1	54.1	59.7	53	$\rightarrow$	B_g^1	52.0	57.0	52
				$\rightarrow$	A_g^1	53.6	59.8	51
A_g^1	73.33	89.6	79	$\rightarrow$	A_g^2	78.6	88.4	79
E_g^2	102.3	99.8	98	$\rightarrow$	A_g^3	101.8	101.9	99
				$\rightarrow$	B_g^2	102.4	101.8	99
E_g^3	106.2	112.2	102	$\rightarrow$	B_g^3	106.4[a]	108.9	101
				$\rightarrow$	A_g^4	108.3	109.3	102
A_g^2	108.3	98.8	88	$\rightarrow$	B_g^4	106.4[a]	97.8	86
A_g^3	128.1	131.1	125	$\rightarrow$	A_g^5	128.2	131.7	125
A_g^4	–	195.2	195	$\rightarrow$	B_g^5	–	198.8	195
E_g^4	236.6	234.4	225	$\rightarrow$	A_g^6	234.6	220.1	224
				$\rightarrow$	B_g^6	235.5	221.1	225

[a]Observed as two peak structure.

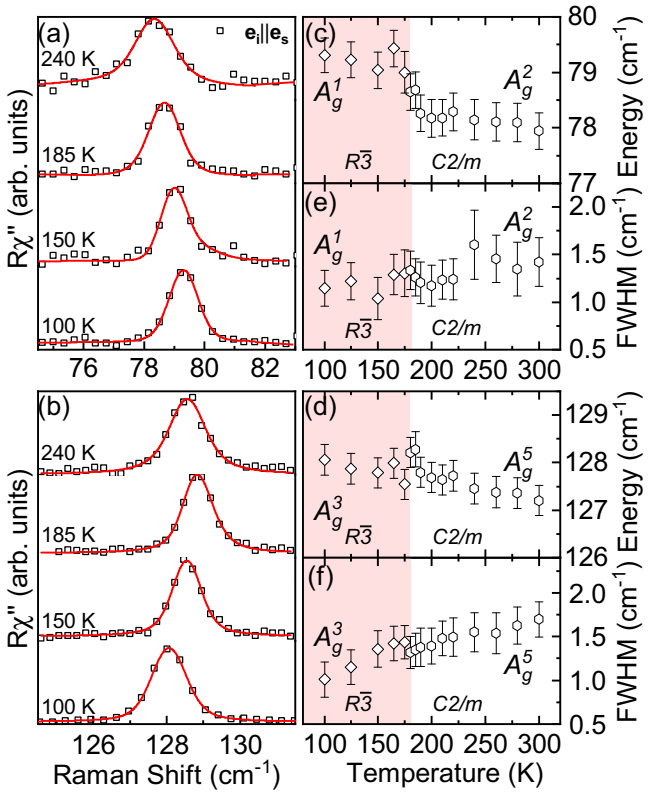

FIG. 3. Temperature dependence of the A_g^1 and A_g^3 phonon modes of the rhombohedral structure and the corresponding A_g^2 and A_g^5 modes of the monoclinic structure, respectively. (a) and (b) Raman spectra at temperatures as indicated. The spectra are shifted for clarity. Solid red lines represent Voigt profiles fitted to the data. (c) and (d) and (e) and (f) Temperature dependence of the phonon energies and linewidths, respectively. Both modes show an abrupt change in energy at the phase transition at 180 K.

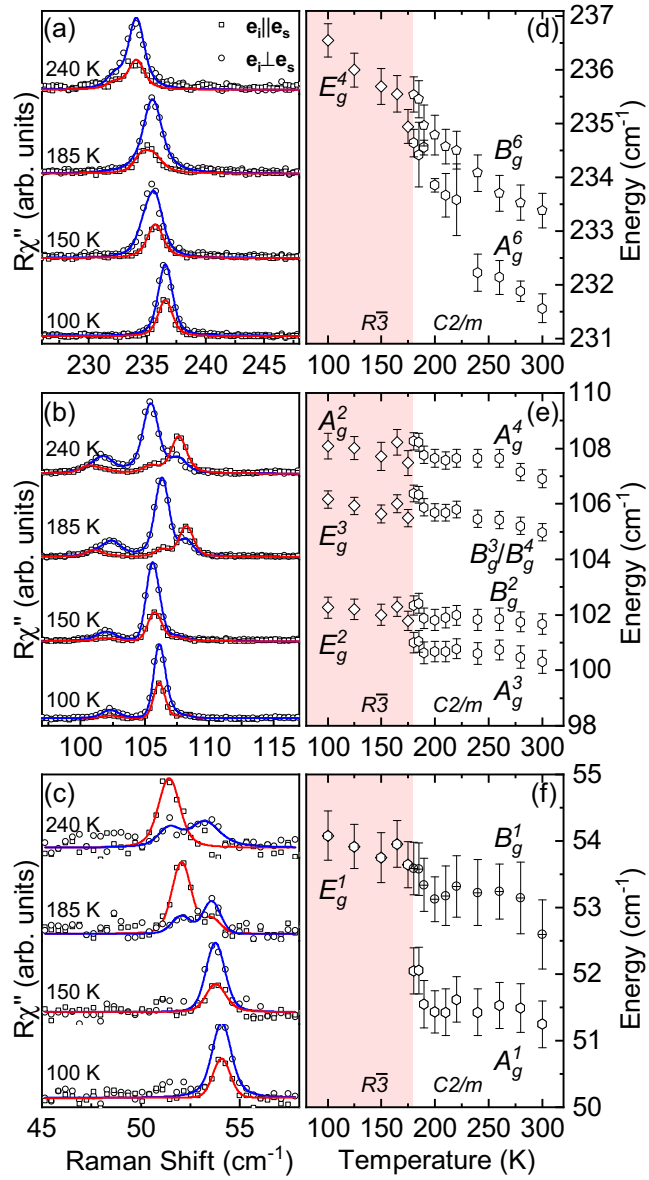

FIG. 4. Temperature dependence of the rhombohedral A_g^4 and E_g modes. (a)–(c) Raman spectra in parallel (open squares) and crossed (open circles) light polarizations at temperatures as indicated. The spectra are shifted for clarity. Blue and red solid lines are fits of Voigt profiles to the data. Two spectra were analyzed simultaneously in two scattering channels with the integrated intensity as the only independent parameter. (d)–(f) Phonon energies obtained from the Voigt profiles. Each E_g mode splits into an A_g and a B_g mode above 180 K.

therefore identify the phonons in the $C2/m$ phase in relation to the calculations and find again good agreement of the energies. The B_g^3 and B_g^4 modes overlap and therefore cannot be resolved separately. As can be seen from the temperature dependence shown below [Fig. 4(b)] the peak at 106 cm^{-1} broadens and gains spectral weight in the monoclinic phase in line with the expectance that two modes overlap. The missing rhombohedral A_g^4 mode corresponds to the monoclinic B_g^5 mode, which is likewise absent in the spectra.

The temperature dependence of the observed phonons is shown in Figs. 3 and 4. In the low-temperature rhombohedral phase all four E_g modes as well as A_g^1 and A_g^2 soften upon warming, whereas A_g^3 hardens up to $T \approx 180$ K before softening again. Crossing the first-order phase transition from $R\bar{3}$ to $C2/m$ crystal symmetry is reflected in the spectra as a symmetry change and/or renormalization for the nondegenerate modes and lifting of the degeneracy of the E_g modes as shown in Table II. In our samples, this transition is observed at $T_s \approx 180$ K. The splitting of the E_g phonons into A_g and B_g modes at the phase transition is sharp (Fig. 4). The rhombohedral A_g^1 and A_g^3 phonons show a jump in energy and a small discontinuity in the linewidth at T_s (Fig. 3). Our spectra were taken during warming in multiple runs after cooling to 100 K each time. We found that the temperature dependence for the phonon modes obtained this way was smooth in each phase. McGuire *et al.* [3,20] reported T_s in the range of 220 K, a coexistence of both phases and a large thermal hysteresis. However, they also noted that the first and second warming cycle showed identical behavior and only found a shift of the transition temperature to higher values for cooling cycles. We therefore consider the difference between the reported transition around 220 K and our $T_s \approx 180$ K significant. To some extent this difference may be attributed

to local heating by the laser. More importantly, we find no signs of phase coexistence in the observed temperature range. The spectra for the low-temperature and high-temperature phases are distinctly different (Fig. 2) and the E_g modes exhibit a clearly resolved splitting which occurs abruptly at T_s. We performed measurements in small temperature steps (see Figs. 3 and 4). This limits the maximum temperature interval where the phase coexistence could occur in our samples to approximately 5 K, much less than the roughly 30 to 80 K reported earlier [3,20]. We cannot exclude the possibility that a small fraction of the low-temperature phase could still coexist with the high-temperature phase over a wider temperature range, whereby weak peaks corresponding to the remains of the low-temperature $R\bar{3}$ phase might be hidden under the strong peaks of the $C2/m$ phase.

IV. CONCLUSION

We studied the lattice dynamics in single crystalline CrI_3 using Raman spectroscopy supported by numerical calculations. For both the low-temperature $R\bar{3}$ and the high-temperature $C2/m$ phase, all except one of the predicted

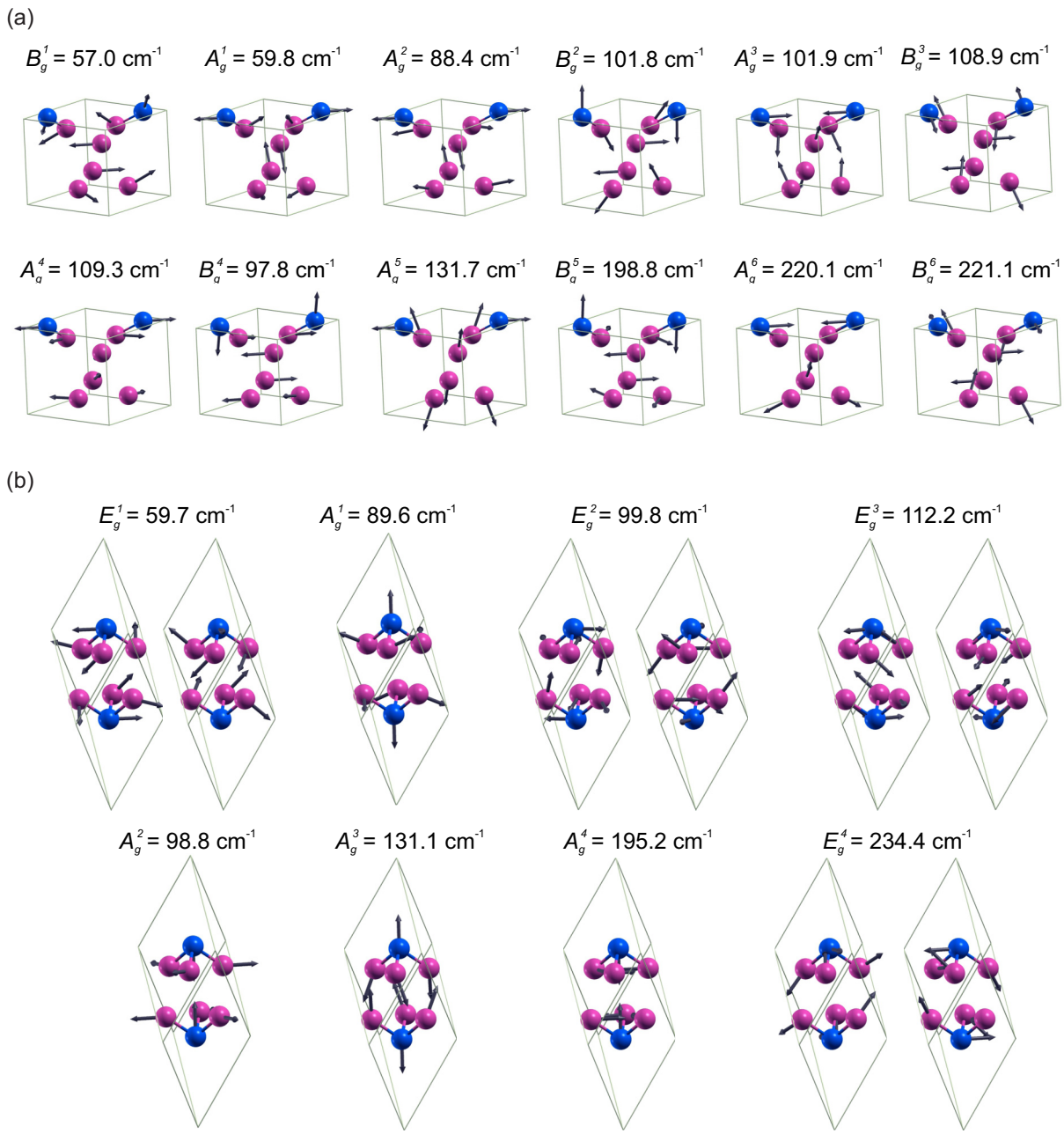

FIG. 5. Raman-active phonons in CrI_3 for (a) the monoclinic phase hosting A_g and B_g modes and for (b) the rhombohedral phase hosting A_g and E_g modes. Blue and violet spheres denote Cr and I atoms, respectively. Solid lines represent primitive unit cells. Arrow lengths are proportional to the square root of the interatomic forces. The given energies are calculated for zero temperature.

phonon modes were identified and the calculated and experimental phonon energies were found to be in good agreement. We determined that the symmetry of the single CrI_3 layers is $p\bar{3}1/m$. Abrupt changes to the spectra were found at the first-order phase transition which was located at $T_s \approx 180$ K, lower than in previous studies. In contrast to the prior reports we found no sign of phase coexistence over temperature ranges exceeding 5 K.

S.Dj.M. and N.L. conceived the experiment, performed the experiment, analyzed and discussed the data, and wrote the paper. A.Š. and J.P. calculated the phonon energies, analyzed and discussed the data, and wrote the paper. Y.L. and C.P. synthesized and characterized the samples. M.Š. performed the experiment and analyzed and discussed the data. A.B. and Z.V.P. analyzed and discussed the data and wrote the paper. All authors commented on the manuscript.

ACKNOWLEDGMENTS

The work was supported by the Serbian Ministry of Education, Science and Technological Development under Projects No. III45018 and No. OI171005. DFT calculations were performed using computational resources at Johannes Kepler University, Linz, Austria. Work at Brookhaven is supported by the U.S. DOE under Contract No. DE-SC0012704.

APPENDIX: EIGENVECTORS

In addition to the phonon energies we also calculated the phonon eigenvectors which are shown in Fig. 5(a) for the high-temperature monoclinic phase and in Fig. 5(b) for the low-temperature rhombohedral phase. The energies, as given, are calculated for zero temperature. The relative displacement of the atoms is denoted by the length of the arrows.

[1] E. Navarro-Moratalla, B. Huang, G. Clark *et al.*, Layer-dependent ferromagnetism in a van der Waals crystal down to the monolayer limit, Nature (London) **546**, 270 (2017).

[2] S. Jiang, L. Li, Z. Wang, K. F. Mak, and J. Shan, Controlling magnetism in 2D CrI_3 by electrostatic doping, Nat. Nanotechnol. **13**, 549 (2018).

[3] M. A. McGuire, H. Dixit, V. R. Cooper, and B. C. Sales, Coupling of crystal structure and magnetism in the layered, ferromagnetic insulator CrI_3, Chem. Mater. **27**, 612 (2015).

[4] J. L. Ladno and J. Fernández-Rossier, On the origin of magnetic anisotropy in two dimensional CrI_3, 2D Mater. **4**, 035002 (2017).

[5] W.-B. Zhang, Q. Qu, P. Zhu, and C.-H. Lam, Robust intrinsic ferromagnetism and half semiconductivity in stable two-dimensional single-layer chromium trihalides, J. Mater. Chem. C **3**, 12457 (2015).

[6] J. F. Dillon, Jr. and C. E. Olson, Magnetization, resonance, and optical properties of the ferromagnet CrI_3, J. Appl. Phys. **36**, 1259 (1965).

[7] D. T. Larson and E. Kaxiras, Raman Spectrum of CrI_3: An *ab initio* study, Phys. Rev. B **98**, 085406 (2018).

[8] N. Lazarević, M. Abeykoon, P. W. Stephens, H. Lei, E. S. Bozin, C. Petrovic, and Z. V. Popović, Vacancy-induced nanoscale phase separation in $K_xFe_{2-y}Se_2$ single crystals evidenced by Raman scattering and powder x-ray diffraction, Phys. Rev. B **86**, 054503 (2012).

[9] H. Ryu, M. Abeykoon, K. Wang, H. Lei, N. Lazarevic, J. B. Warren, E. S. Bozin, Z. V. Popovic, and C. Petrovic, Insulating and metallic spin glass in Ni-doped $K_xFe_{2-y}Se_2$ single crystals, Phys. Rev. B **91**, 184503 (2015).

[10] H. Ryu, K. Wang, M. Opacic, N. Lazarevic, J. B. Warren, Z. V. Popovic, E. S. Bozin, and C. Petrovic, Sustained phase separation and spin glass in Co-doped $K_xFe_{2-y}Se_2$ single crystals, Phys. Rev. B **92**, 174522 (2015).

[11] Y. Liu and C. Petrovic, Three-dimensional magnetic critical behavior in CrI_3, Phys. Rev. B **97**, 014420 (2018).

[12] P. Giannozzi, S. Baroni, N. Bonini, M. Calandra, R. Car, C. Cavazzoni, D. Ceresoli, G. L. Chiarotti, M. Cococcioni, I. Dabo, A. D. Corso, S. de Gironcoli, S. Fabris, G. Fratesi, R. Gebauer, U. Gerstmann, C. Gougoussis, A. Kokalj, M. Lazzeri, L. Martin-Samos, N. Marzari, F. Mauri, R. Mazzarello, S. Paolini, A. Pasquarello, L. Paulatto, C. Sbraccia, S. Scandolo, G. Sclauzero, A. P. Seitsonen, A. Smogunov, P. Umari, and R. M. Wentzcovitch, Quantum espresso: A modular and open-source software project for quantum simulations of materials, J. Phys. Condens. Matter **21**, 395502 (2009).

[13] J. P. Perdew, K. Burke, and M. Ernzerhof, Generalized Gradient Approximation Made Simple, Phys. Rev. Lett. **77**, 3865 (1996).

[14] P. E. Blöchl, Projector augmented-wave method, Phys. Rev. B **50**, 17953 (1994).

[15] G. Kresse and D. Joubert, From ultrasoft pseudopotentials to the projector augmented-wave method, Phys. Rev. B **59**, 1758 (1999).

[16] S. Grimme, Semiempirical GGA-type density functional constructed with a long-range dispersion correction, J. Comput. Chem. **27**, 1787 (2006).

[17] E. A. Wood, The 80 diperiodic groups in three dimensions, Bell Syst. Tech. J. **43**, 541 (1964).

[18] W. G. Fateley, N. T. McDevitt, and F. F. Bentley, Infrared and raman selection rules for lattice vibrations: The correlation method, Appl. Spectrosc. **25**, 155 (1971).

[19] N. Lazarević, Z. V. Popović, R. Hu, and C. Petrovic, Evidence of coupling between phonons and charge-density waves in $ErTe_3$, Phys. Rev. B **83**, 024302 (2011).

[20] M. A. McGuire, G. Clark, S. KC, W. M. Chance, G. E. Jellison, V. R. Cooper, X. Xu, and B. C. Sales, Magnetic behavior and spin-lattice coupling in cleavable van der Waals layered $CrCl_3$ crystals, Phys. Rev. Mater. **1**, 014001 (2017).

Lattice dynamics and phase transitions in $Fe_{3-x}GeTe_2$

A. Milosavljević,[1] A. Šolajić,[1] S. Djurdjić-Mijin,[1] J. Pešić,[1] B. Višić,[1] Yu Liu (刘育),[2] C. Petrovic,[2] N. Lazarević,[1] and Z. V. Popović[1,3]

[1]*Center for Solid State Physics and New Materials, Institute of Physics Belgrade, University of Belgrade, Pregrevica 118, 11080 Belgrade, Serbia*

[2]*Condensed Matter Physics and Materials Science Department, Brookhaven National Laboratory, Upton, New York 11973-5000, USA*

[3]*Serbian Academy of Sciences and Arts, Knez Mihailova 35, 11000 Belgrade, Serbia*

(Received 23 April 2019; published 17 June 2019)

We present Raman spectroscopy measurements of the van der Waals bonded ferromagnet $Fe_{3-x}GeTe_2$, together with lattice dynamics. Four out of eight Raman active modes are observed and assigned, in agreement with numerical calculations. The energies and linewidths of the observed modes display an unconventional temperature dependence at about 150 and 220 K, followed by the nonmonotonic evolution of the Raman continuum. Whereas the former can be related to the magnetic phase transition, the origin of the latter anomaly remains an open question.

DOI: 10.1103/PhysRevB.99.214304

I. INTRODUCTION

A novel class of magnetism hosting van der Waals bonded materials has recently become of great interest, since the materials are suitable candidates for numbers of technical applications [1–5]. Whereas $CrXTe_3$ (X = Si, Ge, Sn) and CrX_3 (X = Cl, Br, I) classes maintain low phase transition temperatures [1,6–9] even in a monolayer regime [10], $Fe_{3-x}GeTe_2$ has a high bulk transition temperature, between 220 and 230 K [11,12], making it a promising applicant.

The $Fe_{3-x}GeTe_2$ crystal structure consists of $Fe_{3-x}Ge$ sublayers stacked between two sheets of Te atoms, and a van der Waals gap between neighboring Te layers [13,14]. Although the structure contains two different types of Fe atoms, it is revealed that vacancies take place only in the Fe2 sites [13,15].

Neutron diffraction, thermodynamic and transport measurements, and Mössbauer spectroscopy were used to analyze the magnetic and functional properties of $Fe_{3-x}GeTe_2$, with an Fe atom deficiency of $x \approx 0.1$ and $T_C = 225$ K. It is revealed that at a temperature of 1.5 K, magnetic moments of $1.95(5)\mu_B$ and $1.56(4)\mu_B$ are directed along the easy magnetic c axes [16]. In chemical vapor transport (CVT) grown Fe_3GeTe_2 single crystals, besides the ferromagnetic (FM)-paramagnetic (PM) transition at a temperature of 214 K, FM layers order antiferromagnetically at 152 K [17]. Close to a ferromagnetic transition temperature of 230 K, a possible Kondo lattice behavior, i.e., coupling of traveling electrons and periodically localized spins, is indicated at $T_K = 190 \pm 20$ K, which is in good agreement with theoretical predictions of 222 K [18].

Lattice parameters, as well as the magnetic transition temperature, vary with Fe ion concentration. Lattice parameters a and c follow the opposite trend, whereas the Curie temperature T_C decreases with an increase of Fe ion concentration [15]. For flux-grown crystals, the critical behavior was investigated by bulk dc magnetization around the ferromagnetic phase transition temperature of 152 K [13]. The anomalous Hall effect was also studied, where a significant amount of defects produces bad metallic behavior [19].

Theoretical calculations predict a dynamical stability of Fe_3GeTe_2 single-layer, uniaxial magnetocrystalline anisotropy that originates from spin-orbit coupling [20]. Recently, anomalous Hall effect measurements on single-crystalline metallic Fe_3GeTe_2 nanoflakes with different thicknesses are reported, with a T_C near 200 K and strong perpendicular magnetic anisotropy [21].

We report $Fe_{3-x}GeTe_2$ single-crystal lattice dynamic calculations, together with Raman spectroscopy measurements. Four out of eight Raman active modes were observed and assigned. Phonon energies are in a good agreement with theoretical predictions. Analyzed phonon energies and linewidths reveal fingerprint of a ferromagnetic phase transition at a temperature around 150 K. Moreover, discontinuities in the phonon properties are found at temperatures around 220 K. Consistently, in the same temperature range, the Raman continuum displays nonmonotonic behavior.

II. EXPERIMENT AND NUMERICAL METHOD

$Fe_{3-x}GeTe_2$ single crystals were grown by the self-flux method as previously described [13]. Samples for scanning electron microscopy (SEM) were cleaved and deposited on graphite tape. Energy dispersive spectroscopy (EDS) maps were collected using a FEI Helios NanoLab 650 instrument equipped with an Oxford Instruments EDS system, equipped with an X-max SSD detector operating at 20 kV. The surface of the as-cleaved $Fe_{3-x}GeTe_2$ crystal appears to be uniform for several tens of microns in both directions, as shown in Fig. 4 of Appendix A. Additionally, the elemental composition maps of Fe, Ge, and Te show a distinctive homogeneity of all the three elements (Fig. 5 of Appendix A).

For Raman scattering experiments, a Tri Vista 557 spectrometer was used in the backscattering micro-Raman configuration. As an excitation source, a solid state laser with a 532 nm line was used. In our scattering configuration, the plane of incidence is the ab plane, where $|a| = |b|$ ($\measuredangle(a, b) = 120°$), with the incident (scattered) light propagation direction

TABLE I. Top panel: The type of atoms, Wyckoff positions, each site's contribution to the phonons in the Γ point, and corresponding Raman tensors for the $P6_3/mmc$ space group of $Fe_{3-x}GeTe_2$. Bottom panel: Phonon symmetry, calculated optical Raman active phonon frequencies (in cm^{-1}) for the magnetic (M) phase, and experimental values for Raman active phonons at 80 K.

Space group $P6_3/mmc$ (No. 194)	
Fe1 (4*e*)	$A_{1g} + E_{1g} + E_{2g} + A_{2u} + E_{1u}$
Fe2 (2*c*)	$E_{2g} + A_{2u} + E_{1u}$
Ge (2*d*)	$E_{2g} + A_{2u} + E_{1u}$
Te (2*c*)	$A_{1g} + E_{1g} + E_{2g} + A_{2u} + E_{1u}$

Raman tensors

$$A_{1g} = \begin{pmatrix} a & 0 & 0 \\ 0 & a & 0 \\ 0 & 0 & b \end{pmatrix} \quad E_{1g} = \begin{pmatrix} 0 & 0 & -c \\ 0 & 0 & c \\ -c & c & 0 \end{pmatrix} \quad E_{2g} = \begin{pmatrix} d & -d & 0 \\ -d & -d & 0 \\ 0 & 0 & 0 \end{pmatrix}$$

Raman active modes

Symmetry	Calculations (M)	Experiment (M)
E^1_{2g}	50.2	
E^1_{1g}	70.3	
E^2_{2g}	122.2	89.2
A^1_{1g}	137.2	121.1
E^2_{1g}	209.5	
E^3_{2g}	228.6	214.8
A^2_{1g}	233.4	239.6
E^4_{2g}	334.3	

along the *c* axes. Samples were cleaved in the air, right before being placed in the vacuum. All the measurements were performed in the high vacuum (10^{-6} mbar) using a KONTI CryoVac continuous helium flow cryostat with a 0.5 mm thick window. To achieve laser beam focusing, a microscope objective with ×50 magnification was used. A Bose factor correction of all spectra was performed. More details can be found in Appendix C.

Density functional theory (DFT) calculations were performed with the QUANTUM ESPRESSO (QE) software package [22]. We used the projector augmented-wave (PAW) pseudopotentials [23,24] with the Perdew-Burke-Ernzerhof (PBE) exchange-correlation functional [25]. The electron wave function and charge density cutoffs of 64 and 782 Ry were chosen, respectively. The *k* points were sampled using the Monkhorst-Pack scheme, with an $8 \times 8 \times 4$ Γ-centered grid. Both magnetic and nonmagnetic calculations were performed, using the experimentally obtained lattice parameters and the calculated values obtained by relaxing the theoretically proposed structure. In order to obtain the lattice parameters accurately, a treatment of the van der Waals interactions is introduced. The van der Waals interaction was included in all calculations using the Grimme-D2 correction [26]. Phonon frequencies in the Γ point are calculated within the linear response method implemented in QE.

III. RESULTS AND DISCUSSION

$Fe_{3-x}GeTe_2$ crystallizes in a hexagonal crystal structure, described with the $P6_3/mmc$ (D^4_{6h}) space group. The atom type, site symmetry, each site's contribution to the phonons in the Γ point, and corresponding Raman tensors for the $P6_3/mmc$ space group are presented in Table I.

Calculated displacement patterns of Raman active modes, which can be observed in our scattering configuration, are presented in Fig. 1(a). Since the Raman tensor of the E_{1g} mode contains only the *z* component (Table I), by selection rules, it cannot be detected when measuring from the *ab* plane in the backscattering configuration. Whereas A_{1g} modes include vibrations of Fe and Te ions along the *c* axis, E_{2g} modes include in-plane vibrations of all four atoms. The Raman spectra of $Fe_{3-x}GeTe_2$ in the magnetic phase (M), at 80 K, and nonmagnetic phase (NM), at 280 K, in a parallel scattering configuration ($\mathbf{e}_i \parallel \mathbf{e}_s$), are presented in Fig. 1 (b). As it can be seen, four peaks at 89.2, 121.1, 214.8, and 239.6 cm^{-1} can be clearly observed at 80 K. According to numerical calculations (see Table I), peaks at 89.2 and 239.6 cm^{-1} correspond to two out of four E_{2g} modes, whereas peaks at 121.1 and 239.6 cm^{-1} can be assigned as two A_{1g} symmetry modes. One should note that numerical calculations performed by using experimentally obtained lattice parameters in the magnetic phase yield a better agreement with experimental values. This is not surprising since the calculations are performed for the stoichiometric compound as opposed to the nonstoichiometry of the sample. Furthermore, it is known that lattice parameters strongly depend on the Fe atom deficiency [15]. All calculated Raman and infrared phonon frequencies, for the magnetic and nonmagnetic phase of $Fe_{3-x}GeTe_2$, using relaxed and experimental lattice parameters, together with experimentally observed Raman active modes, are summarized in Table II of Appendix D.

After assigning all observed modes we focused on their temperature evolution. Having in mind finite instrumental

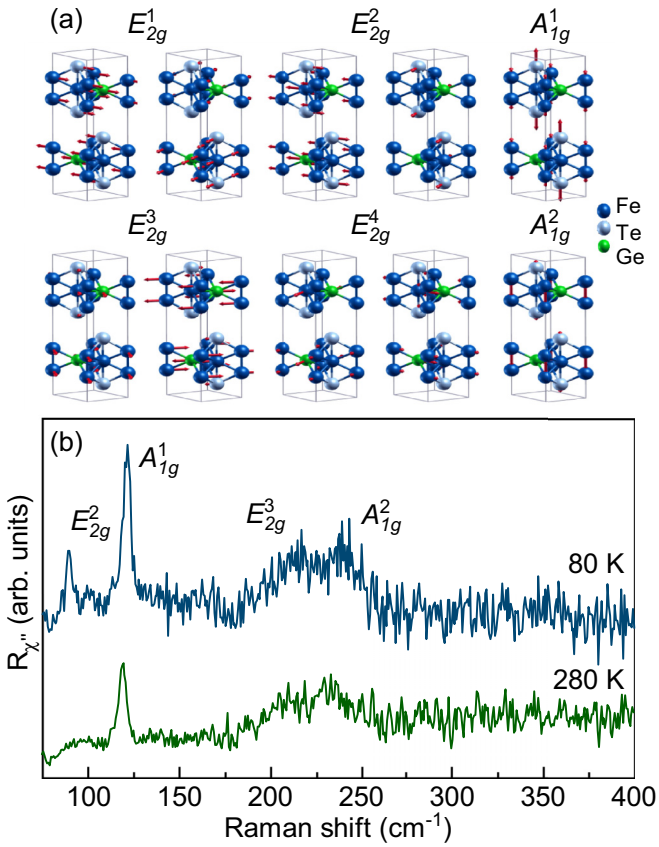

FIG. 1. (a) Displacement patterns of A_{1g} and E_{2g} symmetry modes. (b) Raman spectra of $Fe_{3-x}GeTe_2$ single crystal measured at different temperatures in a parallel polarization configuration.

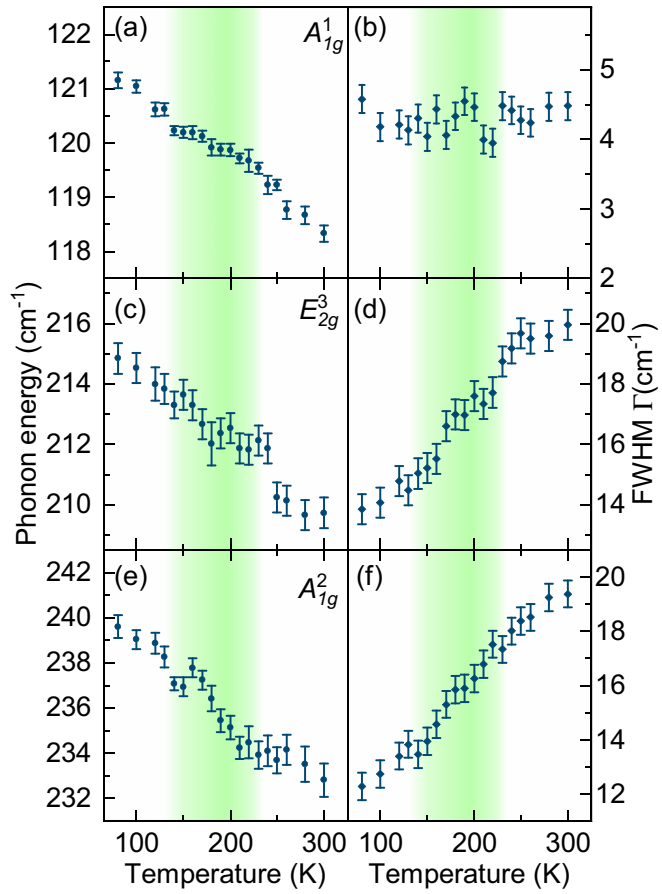

FIG. 2. Energy and linewidth temperature dependence of A^1_{1g} [(a) and (b)], E^3_{2g} [(c) and (d)], and A^2_{1g} [(e) and (f)] phonon modes in $Fe_{3-x}GeTe_2$.

broadening, the Voigt line shape was used for the data analysis [27,28]. The modeling procedure is described in detail in Appendix B and presented in Fig. 6. Figure 2 shows the temperature evolution of the energy and linewidth of the A^1_{1g}, E^3_{2g}, and A^2_{1g} modes between 80 and 300 K. Upon heating the sample, both the energy and linewidth of A^1_{1g} and A^2_{1g} symmetry modes exhibit a small but sudden discontinuity at about 150 K [Figs. 2(a) and 2(e)]. An apparent discontinuity in energy of all analyzed Raman modes is again present at temperatures around 220 K. In the same temperature range the linewidths of these Raman modes show a clear deviation from the standard anharmonic behavior [27–31].

Apart from the anomalies in the phonon spectra, a closer inspection of the temperature-dependent Raman spectra measured in the parallel polarization configuration reveals a pronounced evolution of the Raman continuum [Fig. 3(a)]. For the analysis we have used a simple model including a damped Lorentzian and linear term, $\chi''_{\text{cont}} \propto a\Gamma\omega/(\omega^2 + \Gamma^2) + b\omega$ [32], where a, b, and Γ are temperature-dependent parameters. Figure 3(b) summarizes the results of the analysis with the linear term omitted (most likely originating from a luminescence). At approximately the same temperatures, where phonon properties exhibit discontinuities, the continuum temperature dependence manifests nonmonotonic behavior. The maximum positions of the curve were obtained by integrating those shown in Fig. 3(b). The inset of Fig. 3(b) shows the temperature evolution of their displacements. This analysis confirms the presence of discontinuities in the electronic continuum at temperatures around 150 and 220 K, which leaves a trace in the phonon behavior around these temperatures (Fig. 2). While we do not have evidence for the Kondo effect in the $Fe_{3-x}GeTe_2$ crystals we measured, a modification of the electronic background at FM ordering due to localization or the Kondo effect cannot be excluded.

The temperature evolutions of the phonon self-energies and the continuum observed in the Raman spectra of $Fe_{3-x}GeTe_2$ suggest the presence of phase transition(s). Magnetization measurements of the samples were performed as described in Ref. [13], revealing a FM-PM transition at 150 K. Thus, the discontinuity in the observed phonon properties around this temperature can be traced back to the weak to moderate spin-phonon coupling. The question remains open regarding the anomaly observed at about 220 K. As previously reported, the Curie temperature of the $Fe_{3-x}GeTe_2$ single crystals grown by the CVT method is between 220 and 230 K [11,12,14], varying with the vacancy concentration, i.e., a decrease in the vacancy content will result an increment of T_C [15]. On the other hand, the $Fe_{3-x}GeTe_2$ crystals grown by the self-flux method usually have a lower Curie temperature, since the

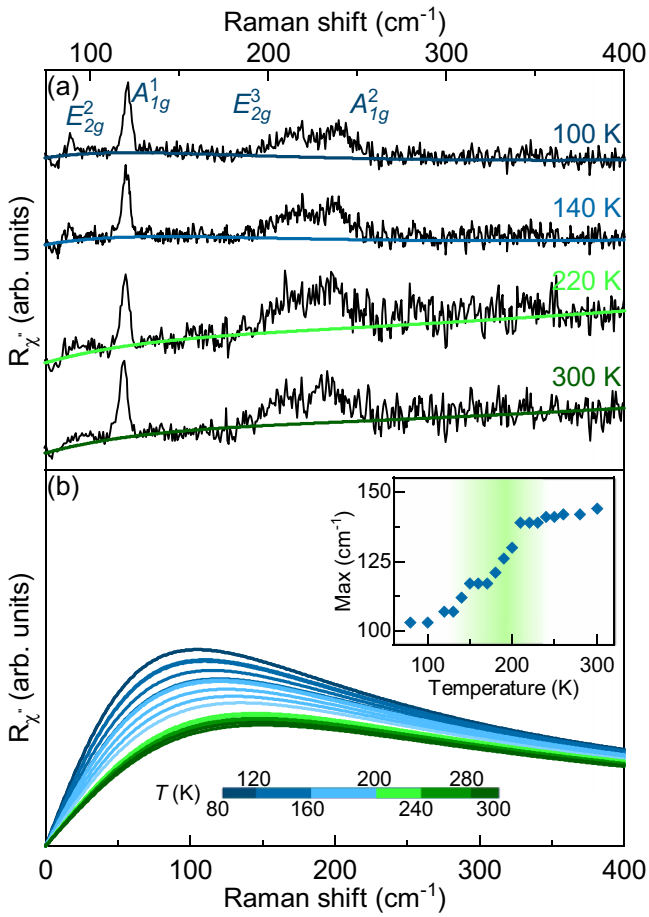

FIG. 3. (a) Raman spectra of $Fe_{3-x}GeTe_2$ at four temperatures measured in a parallel polarization configuration. Solid lines represent the theoretical fit to the experimental data. (b) Temperature evolution of the electronic continuum after omitting the linear term. Inset: Displacement of the maximum of fitted curves.

vacancy content is higher [13,15]. Crystals used in the Raman scattering experiment presented here were grown by the self-flux method with a Fe vacancy content of $x \approx 0.36$ [13]. This is in good agreement with our EDS results of $x = 0.4 \pm 0.1$, giving rise to the FM-PM transition at 150 K. Nevertheless,

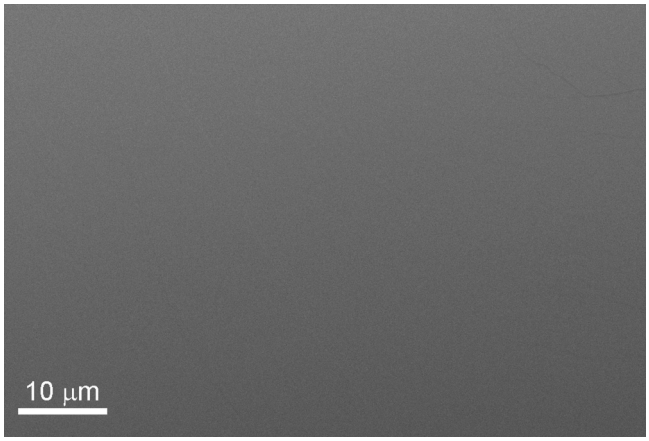

FIG. 4. SEM image of a $Fe_{3-x}GeTe_2$ single crystal.

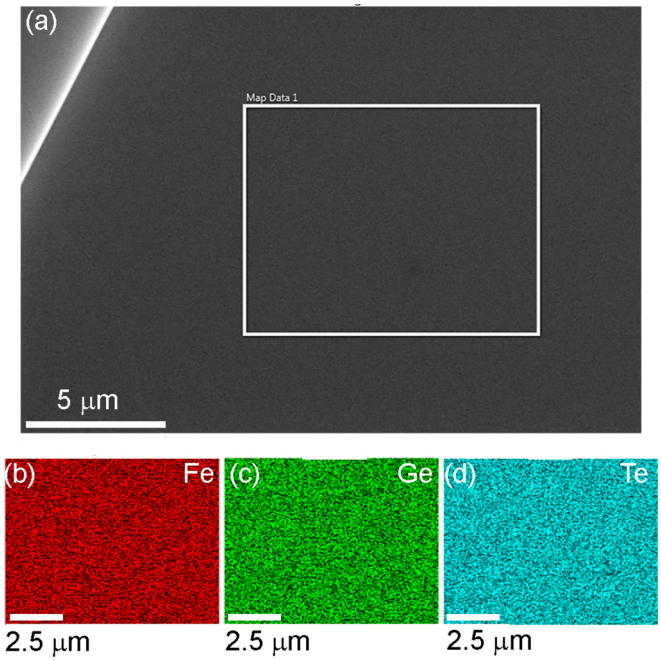

FIG. 5. EDS mapping on a $Fe_{3-x}GeTe_2$ single crystal. (a) Secondary electron image of the crystal with the mapping performed within the rectangle. (b)–(d) Associated EDS maps for Fe, Ge, and Te, respectively.

an inhomogeneous distribution of vacancies may result the formation of vacancy depleted "islands" which in turn would result in an anomaly at 220 K similar to the one observed in our Raman data. However, the EDS data (see Fig. 5) do not support this possibility. At this point we can only speculate that while the long-range order temperature is shifted to a lower temperature by the introduction of vacancies, short-range correlations may develop at 220 K.

IV. CONCLUSION

We have studied the lattice dynamics of flux-grown $Fe_{3-x}GeTe_2$ single crystals by means of Raman spectroscopy and DFT. Four out of eight Raman active modes, two A_{1g} and two E_{2g}, have been observed and assigned. DFT calculations are in good agreement with experimental results. The temperature dependence of the A^1_{1g}, E^3_{2g}, and A^2_{1g} mode properties reveals a clear fingerprint of spin-phonon coupling, at a temperature of around 150 K. Furthermore, the anomalous behavior in the energies and linewidths of the observed phonon modes is present in the Raman spectra at temperatures around 220 K with the discontinuity also present in the electronic continuum. Its origin still remains an open question, and requires further analysis.

ACKNOWLEDGMENTS

The work was supported by the Serbian Ministry of Education, Science and Technological Development under Projects No. III45018 and No. OI171005. DFT calculations were performed using computational resources at Johannes Kepler University, Linz, Austria. Materials synthesis was supported

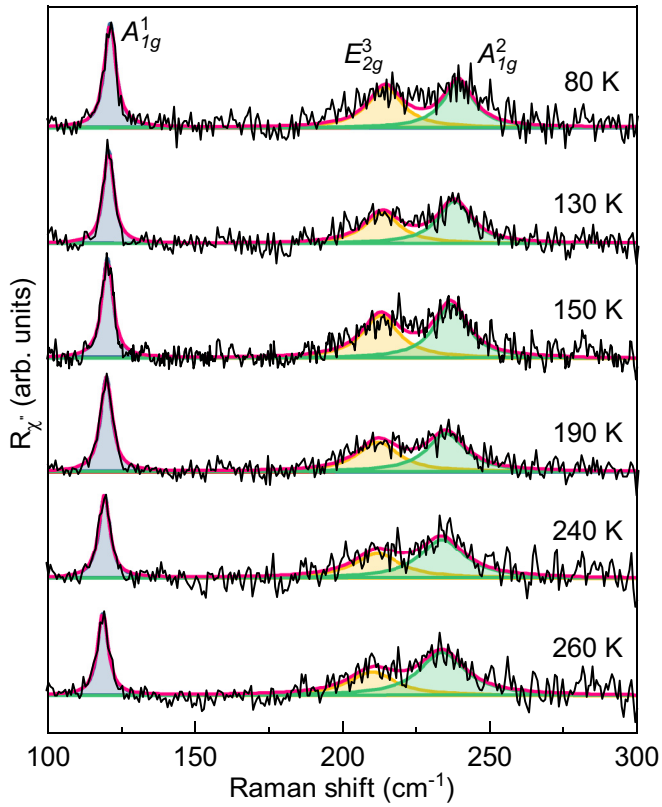

FIG. 6. Modeled Raman spectra of $Fe_{3-x}GeTe_2$ single crystal, after subtracting continuum contributions, obtained at various temperatures. For experimental data modeling, the Voigt line shape was used.

TABLE II. Top panel: Comparison of calculated energies of Raman active phonons using relaxed (R) and experimental [nonrelaxed (NR)] lattice parameters for the magnetic (M) and nonmagnetic phase (NM), given in cm^{-1}. Obtained experimental values in the magnetic phase at a temperature of 80 K are given in the last column. Bottom panel: Comparison of calculated energies of infrared optical phonons of $Fe_{3-x}GeTe_2$.

Raman active modes					
	Calculations				
Sym.	NM-R	M-R	NM-NR	M-NR	Experiment (M)
E^1_{2g}	28.4	49.6	33.9	50.2	
E^1_{1g}	79.2	70.2	71.7	70.3	
E^2_{2g}	115.5	121.0	100.0	122.2	89.2
A^1_{1g}	151.7	139.2	131.7	137.2	121.1
E^2_{1g}	225.5	206.0	194.3	209.5	
E^3_{2g}	238.0	232.6	204.9	228.6	214.8
A^2_{1g}	272.0	262.6	235.7	233.4	239.6
E^4_{2g}	362.0	337.6	315.4	334.7	
Infrared active modes					
A^1_{2u}	70.7	96.6	73.5	92.7	
E^1_{1u}	112.5	121.2	89.4	121.6	
A^2_{2u}	206.0	162.5	183.1	153.7	
E^2_{1u}	226.4	233.6	192.1	231.3	
A^3_{2u}	271.8	248.6	240.8	241.0	
E^3_{1u}	361.1	336.6	314.7	334.7	

by the US Department of Energy, Office of Basic Energy Sciences as part of the Computation Material Science Program (Y.L. and C.P.). Electron microscopy was performed at Jozef Stefan Institute, Ljubljana, Slovenia under Slovenian Research Agency Contract No. P1-0099 (B.V.). This work has received funding from the European Union's Horizon 2020 research and innovation program under the Marie Sklodowska-Curie Grant Agreement No. 645658 (DAFNEOX Project).

APPENDIX A: ELECTRON MICROSCOPY

In order to examine the uniformity of $Fe_{3-x}GeTe_2$, Scanning electron microscopy (SEM) was performed on as-cleaved crystals. It can be seen from Fig. 4 that the crystals maintain uniformity for several tens of microns. Furthermore, the elemental composition was obtained using EDS mapping, as shown in Fig. 5. The atomic percentage, averaged over ten measurements, is 47%, 17%, and 36% (±2%) for Fe, Ge, and Te, respectively, with the vacancy content $x = 0.4 \pm 0.1$. The maps associated with the selected elements appear homogeneous, as they are all present uniformly with no apparent islands or vacancies.

APPENDIX B: DATA MODELING

In order to obtain the temperature dependence of the energies and linewidths of the observed $Fe_{3-x}GeTe_2$ phonon modes, the Raman continuum, shown in colored lines in Fig. 3(a), was subtracted for simplicity from the raw Raman susceptibility data (black line). The spectra obtained after the subtraction procedure are presented in Fig. 6 (black line) for various temperatures. Because of the finite resolution of the spectrometer and the fact that line shapes of all the observed phonons are symmetric, the Voigt line shape ($\Gamma_G = 0.8$ cm^{-1}) was used for data modeling. Blue, yellow, and green lines in Fig. 6 represent fitting curves for A^1_{1g}, E^3_{2g}, and A^2_{1g} phonon modes, respectively, whereas the overall spectral shape is shown in the red line.

APPENDIX C: EXPERIMENTAL DETAILS

Before being placed in a vacuum and being cleaved, the sample was glued to a copper plate with GE varnish in order to achieve good thermal conductivity and prevent strain effects. Silver paste, as a material with high thermal conductivity, was used to attach the copper plate with the sample to the cryostat. The laser beam spot, focused through an Olympus long-range objective of × 50 magnification, was approximately 6 μm in size, with a power less than 1 mW at the sample surface. A TriVista 557 triple spectrometer was used in the subtractive mode, with a diffraction grating combination of 1800/1800/2400 grooves/mm and the entrance and second intermediate slit set to 80 μm, in order to enhance stray light rejection and attain good resolution.

APPENDIX D: CALCULATIONS

In Table II the results of DFT calculations are presented for magnetic (M) and nonmagnetic (NM) relaxed and experimental lattice parameters. For comparison, the experimental results are shown in the last column. Since the lattice parameters strongly depend on the Fe atom deficiency, the best agreement with experimental results gives the magnetic nonrelaxed solution.

[1] N. Sivadas, M. W. Daniels, R. H. Swendsen, S. Okamoto, and D. Xiao, Magnetic ground state of semiconducting transition-metal trichalcogenide monolayers, Phys. Rev. B **91**, 235425 (2015).

[2] K. S. Novoselov, A. K. Geim, S. V. Morozov, D. Jiang, Y. Zhang, S. V. Dubonos, I. V. Grigorieva, and A. A. Firsov, Electric field rffect in atomically thin carbon films, Science **306**, 666 (2004).

[3] Q. H. Wang, K. Kalantar-Zadeh, A. Kis, J. N. Coleman, and M. S. Strano, Electronics and optoelectronics of two-dimensional transition metal dichalcogenides, Nat. Nanotechnol. **7**, 699 (2012).

[4] C. Gong, L. Li, Z. Li, H. Ji, A. Stern, Y. Xia, T. Cao, W. Bao, C. Wang, Y. Wang, Z. Q. Qiu, R. J. Cava, S. G. Louie, J. Xia, and X. Zhang, Discovery of intrinsic ferromagnetism in two-dimensional van der Waals crystals, Nature (London) **546**, 265 (2017).

[5] B. Huang, G. Clark, E. Navarro-Moratalla, D. R. Klein, R. Cheng, K. L. Seyler, D. Zhong, E. Schmidgall, M. A. McGuire, D. H. Cobden, W. Yao, D. Xiao, P. Jarillo-Herrero, and X. Xu, Layer-dependent ferromagnetism in a van der Waals crystal down to the monolayer limit, Nature (London) **546**, 270 (2017).

[6] M. A. McGuire, H. Dixit, V. R. Cooper, and B. C. Sales, Coupling of crystal structure and magnetism in the layered, ferromagnetic insulator CrI_3, Chem. Mater. **27**, 612 (2015).

[7] H. L. Zhuang, Y. Xie, P. R. C. Kent, and P. Ganesh, Computational discovery of ferromagnetic semiconducting single-layer $CrSnTe_3$, Phys. Rev. B **92**, 035407 (2015).

[8] G. T. Lin, H. L. Zhuang, X. Luo, B. J. Liu, F. C. Chen, J. Yan, Y. Sun, J. Zhou, W. J. Lu, P. Tong, Z. G. Sheng, Z. Qu, W. H. Song, X. B. Zhu, and Y. P. Sun, Tricritical behavior of the two-dimensional intrinsically ferromagnetic semiconductor $CrGeTe_3$, Phys. Rev. B **95**, 245212 (2017).

[9] L. D. Casto, A. J. Clune, M. O. Yokosuk, J. L. Musfeldt, T. J. Williams, H. L. Zhuang, M.-W. Lin, K. Xiao, R. G. Hennig, B. C. Sales, J.-Q. Yan, and D. Mandrus, Strong spin-lattice coupling in $CrSiTe_3$, APL Mater. **3**, 041515 (2015).

[10] M.-W. Lin, H. L. Zhuang, J. Yan, T. Z. Ward, A. A. Puretzky, C. M. Rouleau, Z. Gai, L. Liang, V. Meunier, B. G. Sumpter, P. Ganesh, P. R. C. Kent, D. B. Geohegan, D. G. Mandrus, and K. Xiao, Ultrathin nanosheets of $CrSiTe_3$: A semiconducting two-dimensional ferromagnetic material, J. Mater. Chem. C **4**, 315 (2016).

[11] J.-X. Zhu, M. Janoschek, D. S. Chaves, J. C. Cezar, T. Durakiewicz, F. Ronning, Y. Sassa, M. Mansson, B. L. Scott, N. Wakeham, E. D. Bauer, and J. D. Thompson, Electronic correlation and magnetism in the ferromagnetic metal Fe_3GeTe_2, Phys. Rev. B **93**, 144404 (2016).

[12] B. Chen, J. H. Yang, H. D. Wang, M. Imai, H. Ohta, C. Michioka, K. Yoshimura, and M. H. Fang, Magnetic properties of layered itinerant electron ferromagnet Fe_3GeTe_2, J. Phys. Soc. Jpn. **82**, 124711 (2013).

[13] Y. Liu, V. N. Ivanovski, and C. Petrovic, Critical behavior of the van der Waals bonded ferromagnet $Fe_{3-x}GeTe_2$, Phys. Rev. B **96**, 144429 (2017).

[14] H.-J. Deiseroth, K. Aleksandrov, C. Reiner, L. Kienle, and R. K. Kremer, Fe_3GeTe_2 and Ni_3GeTe_2 - Two new layered transition-metal compounds: Crystal structures, HRTEM investigations, and magnetic and electrical properties, Eur. J. Inorg. Chem. **2006**, 1561 (2006).

[15] A. F. May, S. Calder, C. Cantoni, H. Cao, and M. A. McGuire, Magnetic structure and phase stability of the van der Waals bonded ferromagnet $Fe_{3-x}GeTe_2$, Phys. Rev. B **93**, 014411 (2016).

[16] V. Yu. Verchenko, A. A. Tsirlin, A. V. Sobolev, I. A. Presniakov, and A. V. Shevelkov, Ferromagnetic order, strong magnetocrystalline anisotropy, and magnetocaloric effect in the layered telluride $Fe_{3-\delta}GeTe_2$, Inorg. Chem. **54**, 8598 (2015).

[17] J. Yi, H. Zhuang, Q. Zou, Z. Wu, G. Cao, S. Tang, S. A. Calder, P. R. C. Kent, D. Mandrus, and Z. Gai, Competing antiferromagnetism in a quasi-2D itinerant ferromagnet: Fe_3GeTe_2, 2D Mater. **4**, 011005 (2016).

[18] Y. Zhang, H. Lu, X. Zhu, S. Tan, W. Feng, Q. Liu, W. Zhang, Q. Chen, Y. Liu, X. Luo, D. Xie, L. Luo, Z. Zhang, and X. Lai, Emergence of Kondo lattice behavior in a van der Waals itinerant ferromagnet, Fe_3GeTe_2, Sci. Adv. **4**, eaao6791 (2018).

[19] Y. Liu, E. Stavitski, K. Attenkofer, and C. Petrovic, Anomalous Hall effect in the van der Waals bonded ferromagnet $Fe_{3-x}GeTe_2$, Phys. Rev. B **97**, 165415 (2018).

[20] H. L. Zhuang, P. R. C. Kent, and R. G. Hennig, Strong anisotropy and magnetostriction in the two-dimensional Stoner ferromagnet Fe_3GeTe_2, Phys. Rev. B **93**, 134407 (2016).

[21] C. Tan, J. Lee, S.-G. Jung, T. Park, S. Albarakati, J. Partridge, M. R. Field, D. G. McCulloch, L. Wang, and C. Lee, Hard magnetic properties in nanoflake van der Waals Fe_3GeTe_2, Nat. Commun. **9**, 1554 (2018).

[22] P. Giannozzi *et al.*, QUANTUM ESPRESSO: A modular and open-source software project for quantum simulations of materials, J. Phys.: Condens. Matter **21**, 395502 (2009).

[23] P. E. Blöchl, Projector augmented-wave method, Phys. Rev. B **50**, 17953 (1994).

[24] G. Kresse and D. Joubert, From ultrasoft pseudopotentials to the projector augmented-wave method, Phys. Rev. B **59**, 1758 (1999).

[25] J. P. Perdew, K. Burke, and M. Ernzerhof, Generalized Gradient Approximation Made Simple, Phys. Rev. Lett. **77**, 3865 (1996).

[26] S. Grimme, Semiempirical GGA-type density functional constructed with a long-range dispersion correction, J. Comput. Chem. **27**, 1787 (2006).

[27] A. Milosavljević, A. Šolajić, J. Pešić, Y. Liu, C. Petrovic, N. Lazarević, and Z. V. Popović, Evidence of spin-phonon coupling in $CrSiTe_3$, Phys. Rev. B **98**, 104306 (2018).

[28] A. Baum, A. Milosavljević, N. Lazarević, M. M. Radonjić, B. Nikolić, M. Mitschek, Z. I. Maranloo, M. Šćepanović, M. Grujić-Brojčin, N. Stojilović, M. Opel, A. Wang,

C. Petrovic, Z. V. Popović, and R. Hackl, Phonon anomalies in FeS, Phys. Rev. B **97**, 054306 (2018).

[29] M. Opačić, N. Lazarević, M. M. Radonjić, M. Šćepanović, H. Ryu, A. Wang, D. Tanasković, C. Petrovic, and Z. V. Popović, Raman spectroscopy of $K_xK_{2-y}Se_2$ single crystals near the ferromagnet–paramagnet transition, J. Phys.: Condens. Matter **28**, 485401 (2016).

[30] Z. V. Popović, N. Lazarević, S. Bogdanović, M. M. Radonjić, D. Tanasković, R. Hu, H. Lei, and C. Petrovic, Signatures of the spin-phonon coupling in $Fe_{1+y}Te_{1-x}Se_x$ alloys, Solid State Commun. **193**, 51 (2014).

[31] Z. V. Popović, M. Šćepanović, N. Lazarević, M. Opačić, M. M. Radonjić, D. Tanasković, H. Lei, and C. Petrovic, Lattice dynamics of $BaFe_2X_3$ (X = S, Se) compounds, Phys. Rev. B **91**, 064303 (2015).

[32] T. P. Devereaux and R. Hackl, Inelastic light scattering from correlated electrons, Rev. Mod. Phys. **79**, 175 (2007).

Probing charge density wave phases and the Mott transition in $1T$-TaS_2 by inelastic light scattering

S. Djurdjić Mijin,[1] A. Baum,[2] J. Bekaert,[3] A. Šolajić,[1] J. Pešić,[1] Y. Liu,[4,*] Ge He,[2] M. V. Milošević,[3] C. Petrovic,[4] Z. V. Popović,[1,5] R. Hackl,[2] and N. Lazarević[1]

[1]*Center for Solid State Physics and New Materials, Institute of Physics Belgrade, University of Belgrade, Pregrevica 118, RS-11080 Belgrade, Serbia*

[2]*Walther Meissner Institut, Bayerische Akademie der Wissenschaften, D-85748 Garching, Germany*

[3]*Department of Physics, University of Antwerp, Groenenborgerlaan 171, B-2020 Antwerp, Belgium*

[4]*Condensed Matter Physics and Materials Science Department, Brookhaven National Laboratory, Upton, New York 11973-5000, USA*

[5]*Serbian Academy of Sciences and Arts, Knez Mihailova 35, RS-11000 Belgrade, Serbia*

(Received 10 March 2021; revised 14 June 2021; accepted 16 June 2021; published 22 June 2021)

We present a polarization-resolved, high-resolution Raman scattering study of the three consecutive charge density wave (CDW) regimes in $1T$-TaS_2 single crystals, supported by *ab initio* calculations. Our analysis of the spectra within the low-temperature commensurate (C-CDW) regime shows $P\bar{3}$ symmetry of the system, thus excluding the previously proposed triclinic stacking of the "star-of-David" structure, and promoting trigonal or hexagonal stacking instead. The spectra of the high-temperature incommensurate (IC-CDW) phase directly project the phonon density of states due to the breaking of the translational invariance, supplemented by sizable electron-phonon coupling. Between 200 and 352 K, our Raman spectra show contributions from both the IC-CDW and the C-CDW phases, indicating their coexistence in the so-called nearly commensurate (NC-CDW) phase. The temperature dependence of the symmetry-resolved Raman conductivity indicates the stepwise reduction of the density of states in the CDW phases, followed by a Mott transition within the C-CDW phase. We determine the size of the Mott gap to be $\Omega_{\mathrm{gap}} \approx 170$–190 meV, and track its temperature dependence.

DOI: 10.1103/PhysRevB.103.245133

I. INTRODUCTION

Quasi-two-dimensional transition metal dichalcogenides (TMDs), such as the various structures of $TaSe_2$ and TaS_2, have been in the focus of various scientific investigations over the last 30 years, mostly due to the plethora of charge density wave (CDW) phases [1,2]. Among all TMD compounds $1T$-TaS_2 stands out because of its unique and rich electronic phase diagram [3–6]. It experiences phase transitions at relatively high temperatures, making it easily accessible for investigation and, mainly for the hysteresis effects, attractive for potential applications such as data storage [7], information processing [8], or voltage-controlled oscillators [9].

The cascade of phase transitions as a function of temperature includes the transition from the normal metallic to the incommensurate CDW (IC-CDW) phase, the nearly commensurate CDW (NC-CDW) phase, and the commensurate CDW (C-CDW) phase occurring at around $T_{\mathrm{IC}} = 554$ K, $T_{\mathrm{NC}} = 355$ K, and in the temperature range from $T_{\mathrm{C}\downarrow} = 180$ K to $T_{\mathrm{C}\uparrow} = 230$ K, respectively. Recent studies indicate the possibility of yet another phase transition in $1T$-TaS_2 at $T_H = 80$ K, named the hidden CDW state [10–12]. This discovery led to a new boost in attention for $1T$-TaS_2.

Upon lowering the temperature to $T_{\mathrm{IC}} = 554$ K, the normal metallic state structure, described by the space group $P\bar{3}m1$ (D^d_{3d}) [13], transforms into the IC-CDW state. As will be demonstrated here, the IC-CDW domains shrink upon further temperature reduction until they gradually disappear, giving place to the C-CDW ordered state. This region in the phase diagram between 554 and roughly 200 K is characterized by the coexistence of the IC-CDW and C-CDW phases and is often referred to as NC-CDW. At the transition temperature T_C, IC-CDW domains completely vanish [14] and a new lattice symmetry is established. There is a general consensus about the formation of "star-of-David" clusters with in-plane $\sqrt{13}a \times \sqrt{13}a$ lattice reconstruction, whereby 12 Ta atoms are grouped around the 13th Ta atom [15,16]. In the absence of any external strain fields, this can be achieved in two equivalent ways (by either clockwise or counterclockwise rotations) thus yielding domains [17]. Despite extensive investigations, both experimental and theoretical, it remains an open question whether the stacking of star-of-David clusters is triclinic, trigonal, hexagonal, or a combination thereof [15,16,18–20]. The C-CDW phase is believed to be an insulator [3,21–23] with a gap of around 100 meV [13]. Very recent theoretical studies based on density-functional theory (DFT) find an additional ordering pattern along the crystallographic c axis. The related gap has a width of approximately 0.5 eV along k_z and becomes gapped at the Fermi energy E_{F} in the C-CDW phase [24,25].

Nearly all of the previously reported results for optical phonons in $1T$-TaS_2 are based on Raman spectroscopy on the C-CDW phase and on temperature-dependent measurements in a narrow range around the NC-CDW to C-CDW phase transition [13,15,18–20]. In this paper we present temperature-dependent polarization-resolved Raman

*Present address: Los Alamos National Laboratory, Los Alamos, New Mexico 87545, USA.

measurements in the temperature range from 4 to 370 K covering all three CDW regimes of $1T$-TaS_2. Our analysis of the C-CDW phase confirms the symmetry to be $P\bar{3}$, while the NC-CDW phase is confirmed as a mixed regime of commensurate and incommensurate domains. The Raman spectra of the IC-CDW phase mainly project the phonon density of states due to the breaking of translation invariance and sizable electron-phonon coupling. The growth of the CDW gap upon cooling, followed by the opening of the Mott gap, is traced via the initial slope of the symmetry-resolved spectra. The size of 170–190 meV and the temperature dependence of the Mott gap are directly determined from high-energy Raman data.

II. EXPERIMENTAL AND NUMERICAL METHODS

The preparation of the studied $1T$-TaS_2 single crystals is described elsewhere [26–29]. Calibrated customized Raman scattering equipment was used to obtain the spectra. Temperature-dependent measurements were performed with the sample attached to the cold finger of a He-flow cryostat. The sample was cooled down to the lowest temperature and then heated. In either case the rates were less than ± 1 K/min. All measurements were performed in a high vacuum of approximately 5×10^{-5} Pa.

The 575-nm laser line of a diode-pumped Coherent GENESIS MX-SLM solid state laser was used as an excitation source. Additional measurements with the 458- and 514-nm laser lines were performed with a Coherent Innova 304C argon ion laser. The absorbed power was set at 4 mW. All spectra shown are corrected for the sensitivity of the instrument and the Bose factor, yielding the imaginary part of the Raman susceptibility $R\chi''$, where R is an experimental constant. An angle of incidence of $\Theta_i = 66.0 \pm 0.4^\circ$ and atomically flat cleaved surfaces enable us to measure at energies as low as 5 cm^{-1} without a detectable contribution from the laser line since the directly reflected light does not reach the spectrometer. The corresponding laser spot has an area of roughly 50×100 μm^2 which prevents us from observing the possible emergence of the domains [17,30]. The inelastically scattered light is collected along the surface normal (crystallographic c axis) with an objective lens having a numerical aperture of 0.25. In the experiments presented here, the linear polarizations of the incident and scattered light are denoted as $\mathbf{e}_i$ and $\mathbf{e}_s$, respectively. For $\mathbf{e}_i$ horizontal to the plane of incidence there is no projection on the crystallographic c axis. For the low numerical aperture of the collection optics $\mathbf{e}_s$ is always perpendicular to the c axis. Low-energy data up to 550 cm^{-1} were acquired in steps of $\Delta\Omega = 1$ cm^{-1} with a resolution of $\sigma \approx 3$ cm^{-1}. The symmetric phonon lines were modeled using Voigt profiles where the width of the Gaussian part is given by σ. For spectra up to higher energies the step width and resolution were set at $\Delta\Omega = 50$ cm^{-1} and $\sigma \approx 20$ cm^{-1}, respectively. The Raman tensors for the D_{3d} point group are given in Table I. Accordingly, parallel linear polarizations project both A_{1g} and E_g symmetries, while crossed linear polarizations only project E_g. The pure A_{1g} response then can be extracted by subtraction.

We have performed DFT calculations as implemented in the ABINIT package [31]. We have used the Perdew-Burke-Ernzerhof (PBE) functional, an energy cutoff of 50 Ha for the plane-wave basis, and we have included spin-orbit coupling by means of fully relativistic Goedecker pseudopotentials [32,33], where Ta-$5d^3 6s^2$ and S-$3s^2 3p^4$ states are treated as valence electrons. The crystal structure was relaxed so that forces on each atom were below 10 μeV/Å and the total stress on the unit cell below 1 bar, yielding lattice parameters $a = 3.44$ Å and $c = 6.83$ Å. Subsequently, the phonons and the electron-phonon coupling (EPC) were obtained from density-functional perturbation theory (DFPT) calculations, also within ABINIT [34]. Here, we have used an $18 \times 18 \times 12$ **k**-point grid for the electron wave vectors and a $6 \times 6 \times 4$ **q**-point grid for the phonon wave vectors. For the electronic occupation we employed Fermi-Dirac smearing with broadening factor $\sigma_{FD} = 0.01$ Ha, which is sufficiently high to avoid unstable phonon modes related to the CDW phases.

TABLE I. Raman tensors for trigonal systems (point group D_{3d}).

$$A_{1g} = \begin{pmatrix} a & 0 & 0 \\ 0 & a & 0 \\ 0 & 0 & b \end{pmatrix} \quad {}^1E_g = \begin{pmatrix} c & 0 & 0 \\ 0 & -c & d \\ 0 & d & 0 \end{pmatrix} \quad {}^2E_g = \begin{pmatrix} 0 & -c & -d \\ -c & 0 & 0 \\ -d & 0 & 0 \end{pmatrix}$$

III. RESULTS AND DISCUSSION

A. Lattice dynamics of the charge-density wave regimes

Temperature-dependent symmetry-resolved Raman spectra of $1T$-TaS_2 are presented in Fig. 1. It is obvious that their evolution with temperature is divided into three distinct ranges (IC-CDW, NC-CDW, and C-CDW) as indicated. The lattice dynamics for each of these ranges will be treated separately in the first part of the section. In the second part we address the electron dynamics.

1. C-CDW phase

At the lowest temperatures $1T$-TaS_2 exists in the commensurate C-CDW phase. Here, the atoms form so-called star-of-David clusters. Different studies report either triclinic stacking of these clusters leading to $P\bar{1}$ unit cell symmetry [16], or trigonal or hexagonal stacking and $P\bar{3}$ unit cell symmetry [15,18–20]. A factor group analysis predicts 57 A_g Raman-active modes with an identical polarization dependence for $P\bar{1}$ unit cell symmetry, and alternatively 19 A_g+19 E_g Raman-active modes for $P\bar{3}$ unit cell symmetry [13] Our polarized Raman scattering measurements at $T = 4$ K, measured in two scattering channels, together with the corresponding cumulative fits are shown in Fig. 2. As it can be seen, we have observed modes of two different symmetries in the related scattering channels. This result indicates trigonal or hexagonal stacking of the star-of-David clusters. The symmetric phonon lines can be described by Voigt profiles, the best fit of which is shown as blue (for parallel light polarizations) and red (crossed polarizations) lines. After fitting Voigt profiles to the Raman spectra, 38 phonon modes were singled out. Following the selection rules for A_g and E_g symmetry modes, 19 were assigned as A_g and 19 as E_g symmetry, meaning all expected modes could be identified. The contribution from each mode to the cumulative fit is presented in Fig. 2 as green

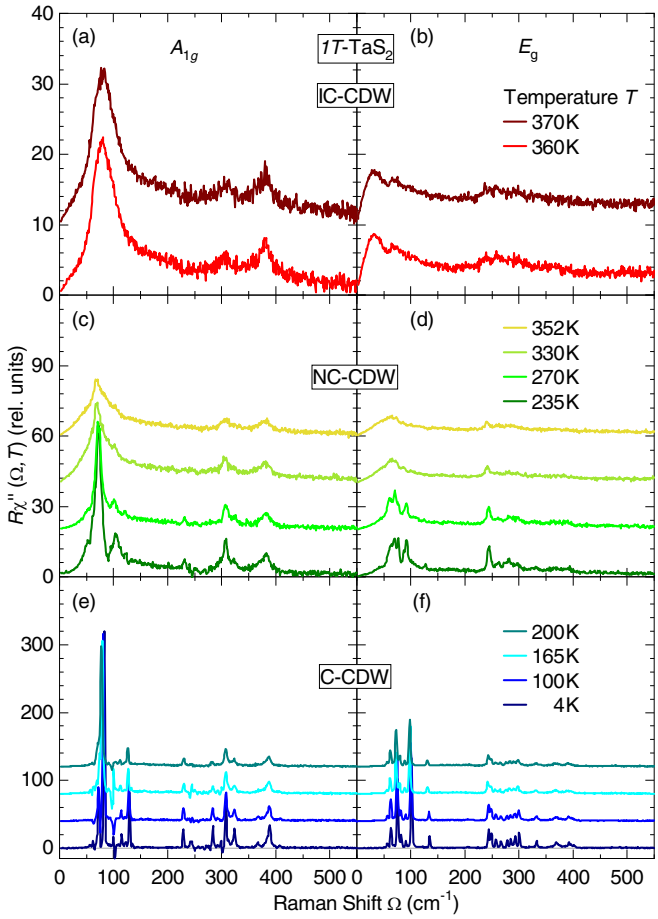

FIG. 1. Symmetry-resolved Raman spectra of $1T$-TaS_2 at temperatures as indicated. Both C-CDW (blue lines) and IC-CDW (red lines) domains yield significant contributions to the Raman spectra of the NC-CDW phase (green lines).

TABLE II. A_{1g} and E_g Raman mode energies experimentally obtained at $T = 4$ K.

n_o	ω_{A_g} (cm^{-1})	ω_{E_g} (cm^{-1})
1	62.6	56.5
2	73.3	63.3
3	83.4	75.3
4	114.9	82.0
5	121.9	90.5
6	129.5	101.1
7	228.7	134.8
8	244.1	244.0
9	271.9	248.9
10	284.2	257.5
11	298.6	266.6
12	307.2	278.3
13	308.2	285.0
14	313.0	292.9
15	321.2	300.5
16	324.2	332.7
17	332.0	369.2
18	367.2	392.6
19	388.4	397.7

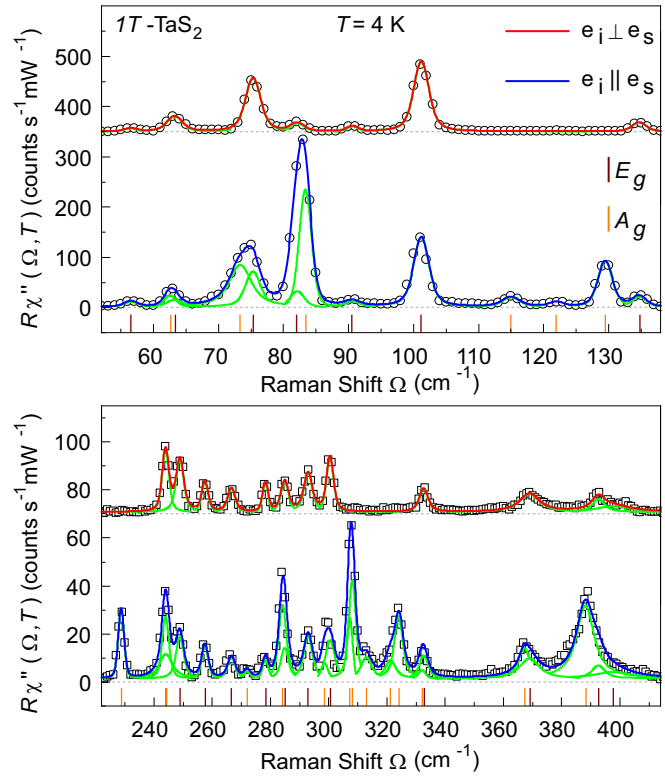

FIG. 2. Raman spectra at $T = 4$ K, i.e., in the C-CDW phase, for parallel and crossed light polarizations. Red and blue solid lines represent fits of the experimental data using Voigt profiles. Spectra are offset for clarity. The short vertical lines depict central frequencies obtained from the data analysis. The exact energy values are presented in Table II.

lines, whereas the complete list of the corresponding phonon energies can be found in Table II.

2. *IC-CDW phase*

At the highest experimentally accessible temperatures $1T$-TaS_2 adopts the IC-CDW phase. Data collected by Raman scattering at $T = 370$ K, containing all symmetries, are shown as a blue solid line in Fig. 3. As $1T$-TaS_2 is metallic in this phase [25] we expect the phonon lines to be superimposed on a continuum of electron-hole excitations which we approximate using a Drude spectrum shown as a dashed line [35,36].

Since the IC-CDW phase arises from the normal metallic phase, described by space group $P\bar{3}m1$ [13,37], it is interesting to compare our Raman results on the IC-CDW phase to an *ab initio* calculation of the phonon dispersion in the normal phase, shown as an inset in Fig. 3. Four different optical modes were obtained at Γ: E_u at 189 cm^{-1} (double degenerate), E_g at 247 cm^{-1} (double degenerate), A_{2u} at 342 cm^{-1}, and A_{1g} at 346 cm^{-1}. A factor group analysis shows that two of these are Raman active, namely E_g and A_{1g} [13].

We observe that the calculated phonon eigenvalues of the simple metallic phase at Γ do not closely match the observed peaks in the experimental spectra of the IC-CDW phase. Rather, these correspond better to the calculated phonon density of states (PDOS), depicted in Fig. 3. There are essentially three different ways to project the PDOS in a Raman

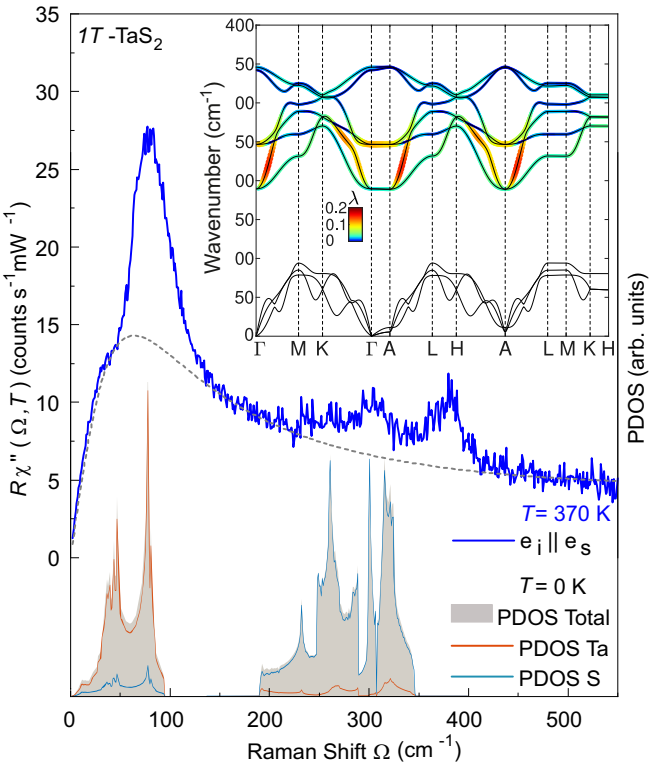

FIG. 3. Raman response for parallel light polarizations in the IC-CDW phase at 370 K (blue line). The dashed line depicts the possible electronic continuum. The contributions of the Ta (dark brown) and S atoms (light brown) to the calculated PDOS (gray area) are shown below. The inset shows the calculated phonon dispersion of $1T$-TaS_2 in the simple metallic phase, with the electron-phonon coupling (λ) of the optical branches indicated through the color scale.

experiment and to overcome the $q \approx 0$ selection given by the small momentum of visible light: (i) scattering on impurities [38], (ii) enhanced electron-phonon coupling [39], and (iii) breaking of the translational symmetry in the IC-CDW phase. (i) We rule out chemical impurity scattering, expected to exist at all temperatures, as the low-temperature spectra (Fig. 2) show no signs thereof. (ii) The additional scattering channel may come from the electron-phonon coupling (EPC). The calculated EPC, λ, in the optical modes (inset of Fig. 3) is limited, yet not negligible, reaching maxima of $\sim$0.2 in the lower optical branches around the Brillouin zone (BZ) points Γ and A. The calculated atom-resolved PDOS shows the acoustic modes to be predominantly due to Ta and the optical modes due to S, as a result of their difference in atomic mass. The acoustic modes display several dips that are signatures of the latent CDW phases, for which the EPC cannot be reliably determined. Significant EPC in the optical modes of $1T$-TaS_2 is furthermore supported by experimental results linking a sharp increase in the resistivity above the IC-CDW transition temperature to the EPC [37]. It also corroborates calculated [14] and experimentally obtained [13] values of the CDW gap, which correspond to intermediate to strong EPC [37]. (iii) Although EPC certainly contributes we believe that the majority of the additional scattering channels can be traced back to the incommensurate breaking of the translational invariance upon entering IC-CDW. Thus the "weighted" PDOS is projected into the Raman spectrum [see Figs. 1(a) and 1(b)]. These "weighting" factors depend on the specific symmetries along the phonon branches as well as the "new periodicity" and go well beyond the scope of this paper.

3. NC-CDW phase

The nearly commensurate phase is seen as a mixed phase consisting of regions of commensurate and incommensurate CDWs [40,41]. This coexistence of high- and low-temperature phases is observable in our temperature-dependent data as shown in Fig. 1. The spectra for the IC-CDW (red curves) and C-CDW phase (blue curves) are distinctly different, as also visible in the data shown above (Figs. 2 and 3). The spectra of the NC-CDW phase (235 K $< T <$ 352 K) comprise contributions from both phases. As 352 K is the highest temperature at which the contributions from the C-CDW phase can be observed in the spectra, we suggest that the phase transition temperature from IC-CDW to NC-CDW phase is somewhere in between 352 and 360 K. This conclusion is in good agreement with experimental results regarding this transition [4–6].

B. Gap evolution

The opening of a typically momentum-dependent gap in the electronic excitation spectrum is a fundamental property of CDW systems which has also been observed in $1T$-TaS_2 [13,37,42]. Here, in addition to the CDW, a Mott transition at the onset of the C-CDW phase leads to an additional gap opening in the bands close to the Γ point [21,43]. Symmetry-resolved Raman spectroscopy can provide additional information here using the momentum resolution provided by the selection rules. To this end, we look at the initial slopes of the electronic part of the spectra.

As shown in Figs. 4(a)–4(c), different symmetries project individual parts of the BZ [36,44]. The vertices given by the hexagonal symmetry of $1T$-TaS_2 are derived in Appendix C. The A_{1g} vertex mainly highlights the area around the Γ point while the E_g vertices predominantly project the BZ boundaries. The opening of a gap at the Fermi level reduces N_F, leading to an increase of the resistivity in the case of $1T$-TaS_2. This reduction of N_F manifests itself also in the Raman spectra which, to zeroth order, are proportional to N_F [35,44]. As a result, the initial slope changes as shown Figs. 4(d) and 4(e), which zoom in on the low-energy region of the spectra from Fig. 1. The initial slope of the Raman response is $R \lim_{\Omega\to 0} \frac{\partial \chi''}{\partial \Omega} \propto N_F \tau_0$, where R incorporates only experimental factors [44]. The electronic relaxation $\Gamma_0^* \propto (N_F \tau_0)^{-1}$ is proportional to the dc resistivity $\rho(T)$ [45]. If a gap opens up there is vanishing intensity at $T = 0$ below the gap edge for an isotropic gap. At finite temperature there are thermally excited quasiparticles which scatter. Thus, there is a linear increase at low energies [35]. The black lines in Figs. 4(d)–4(g) represent the initial slopes and their temperature dependences. The lines comprise carrier relaxation and gap effects, and we focus only on the relative changes.

Starting in the IC-CDW phase at $T = 370$ K [Fig. 4(d)] the initial slope is higher for the E_g spectrum than for A_{1g} symmetry. While the CDW gap started to open already at

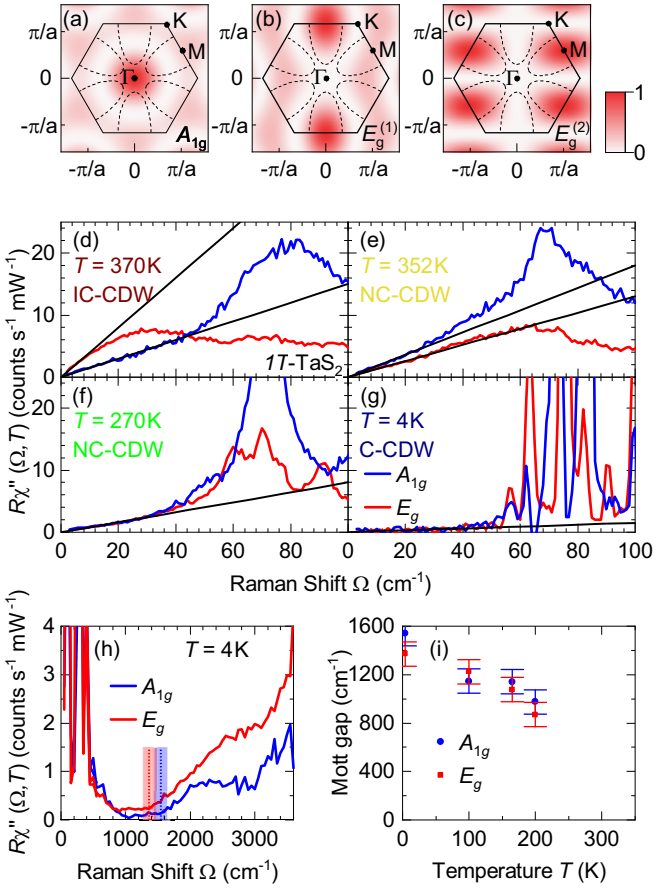

FIG. 4. Evolution of the gaps. (a)–(c) Squared Raman vertices and Fermi surface of $1T$-TaS_2 for the indicated symmetries in the normal phase above T_{IC}. The derivation of Raman vertices is presented in Appendix C. (d)–(g) Low-energy Raman spectra for A_{1g} symmetry (blue) and E_g symmetries (red) at temperatures as indicated. The spectra shown are zooms on the data shown in Fig. 1. The black lines highlight the initial slope of the spectra. (h) High-energy spectra at 4 K. Vertical dashed lines and colored bars indicate the approximate size and error bars of the Mott gap for the correspondingly colored spectrum. (i) Temperature dependence of the Mott gap Δ_μ ($\mu = A_{1g}, E_g$).

554 K around the M points [43], which are highlighted by the E_g vertex, the Fermi surface projected by the E_g vertex continues to exist. Thus, we may interpret the different slopes as a manifestation of a momentum-dependent gap in the IC-CDW phase and assume overall intensity effects to be symmetry independent for all temperatures. At $T = 352$ K [Fig. 4(e)] the slope for E_g symmetry is substantially reduced to below the A_{1g} slope due to a strong increase of the CDW gap in the commensurate regions [43] which emerge upon entering the NC-CDW phase. Further cooling also decreases the slope for the A_{1g} spectrum, as the Mott gap around the Γ point starts to open within the continuously growing C-CDW domains [40,41]. Below $T = 270$ K the initial slopes are identical for both symmetries and decrease with temperature. Apparently, the Mott gap opens up on the entire Fermi surface in direct correspondence with the increase of the resistivity by approximately an order of magnitude [3]. Finally, at the lowest temperature close to 4 K the initial slopes drop to almost zero

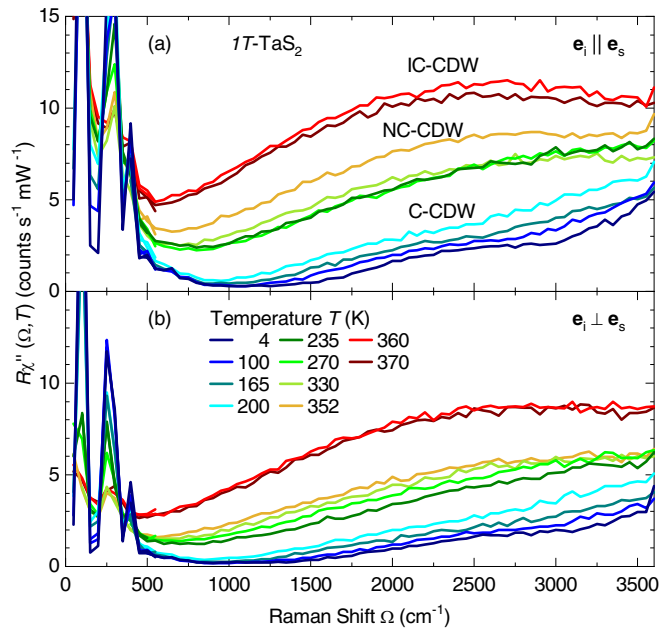

FIG. 5. Raman spectra up to high energies for (a) parallel and (b) crossed polarizations of the incident and scattered light at temperatures as given in the legend.

[Fig. 4(g)], indicating vanishing conductivity or fully gapped bands in the entire BZ.

Concomitantly, and actually more intuitive for the opening of a gap, we observe the loss of intensity in the Raman spectra below a threshold at an energy Ω_{gap}. Below 30 cm^{-1} the intensity is smaller than 0.2 counts$(mW\ s)^{-1}$ [Fig. 4(g)] and still smaller than 0.3 counts$(mW\ s)^{-1}$ up to 1500 cm^{-1} [Fig. 4(h)]. For a superconductor or a CDW system the threshold is given by 2Δ, where Δ is the single-particle gap, and a pileup of intensity for higher energies, $\Omega > 2\Delta$ [44]. A pileup of intensity cannot be observed here. Rather, the overall intensity is further reduced with decreasing temperature as shown in Figs. 5 and 6 in Appendixes A and B. In particular, the reduction occurs in distinct steps between the phases and continuous inside the phases with the strongest effect in the C-CDW phase below approximately 210 K (Fig. 5). In a system as clean as $1T$-TaS_2 the missing pileup in the C-CDW phase is surprising and argues for an alternative interpretation.

In a Mott system, the gap persists to be observable but the pileup is not a coherence phenomenon and has not been observed yet. In fact, the physics is quite different, and the conduction band is split symmetrically about the Fermi energy E_F into a lower and a upper Hubbard band. Thus in the case of Mott-Hubbard physics the experimental signatures are more such as those expected for an insulator or semiconductor having a small gap, where at $T = 0$ there is a range without intensity and an interband onset with a band-dependent shape. At finite temperature there are thermal excitations inside the gap. For $1T$-TaS_2 at the lowest accessible temperature, both symmetries exhibit a flat, nearly vanishing electronic continuum below a slightly symmetry-dependent threshold (superposed by the phonon lines at low energies). Above the threshold a weakly structured increase is observed. We interpret this onset as the distance of the lower

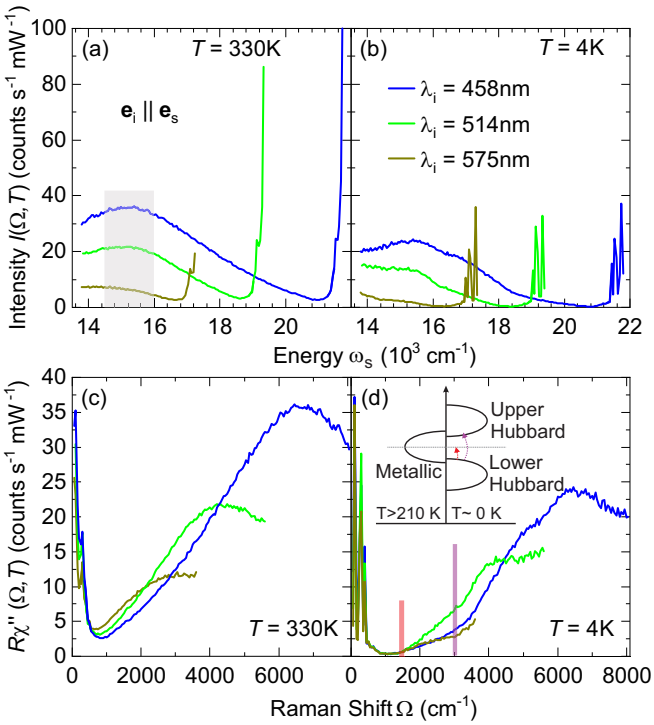

FIG. 6. Luminescence contribution to the Raman data. (a), (b) Intensity as a function of the absolute frequency for (a) $T = 330$ K and (b) $T = 4$ K. The approximate peak maximum of the contribution attributed to luminescence is highlighted by the gray shaded area. (c), (d) Raman susceptibility calculated from (a) and (b), respectively, shown as a function of frequency (Raman) shift. The luminescence peak appears at different Raman shifts depending on the wavelength of the laser light. At $T = 4$ K the spectra are identical up to 1600 cm^{-1} for all laser light wavelengths.

Hubbard band from the Fermi energy E_F or half of the distance between the lower and the upper Hubbard band, shown as vertical dashed lines at 1350–1550 cm^{-1} $\equiv$ 170–190 meV [Fig. 4(h)]. The energy is in good agreement with gap obtained from the in-plane angle-resolved photoemission spectroscopy (ARPES) [43], scanning tunneling spectroscopy [46], and infrared spectroscopy [13] which may be compared directly with our Raman results measured with in-plane polarizations. Upon increasing the temperature the size of the gap shrinks uniformly in both symmetries [Fig. 4(i)] and may point to an onset above the C-CDW phase transition, consistent with the result indicated by the initial slope. However, we cannot track the development of the gap into the NC-CDW phase as an increasing contribution of luminescence (see Appendix B) overlaps with the Raman data.

Recently, it was proposed on the basis of DFT calculations that $1T$-TaS_2 orders also along the c axis perpendicular to the planes in the C-CDW state [24,25]. This quasi-one-dimensional (1D) coupling is unexpectedly strong and the resulting metallic band is predicted to have a width of approximately 0.5 eV. For specific relative ordering of the star of David patterns along the c axis this band develops a gap of 0.15 eV at E_F [25], which is intriguingly close to the various experimental observations. However, since our light polarizations are strictly in plane, we have to conclude that the gap observed here (and presumably in the other experiments) is an in-plane gap. Our experiment cannot detect an out-of-plane gap. Thus, neither a quasimetallic dispersion along the c axis nor a gap in this band along k_z may be excluded in the C-CDW phase. However, there is compelling evidence for a Mott-like gap in the layers rather than a CDW gap.

IV. CONCLUSIONS

We have presented a study of the various charge density wave regimes in $1T$-TaS_2 by inelastic light scattering, supported by *ab initio* calculations. The spectra of lattice excitations in the commensurate CDW (C-CDW) phase determine the unit cell symmetry to be $P\bar{3}$, indicating trigonal or hexagonal stacking of the "star-of-David" structure. The high-temperature spectra of the incommensurate CDW (IC-CDW) state are dominated by a projection of the phonon density of states caused by either a significant electron-phonon coupling or, more likely, the superstructure. The intermediate nearly commensurate (NC-CDW) phase is confirmed to be a mixed regime of commensurate and incommensurate regions contributing to the phonon spectra below an onset temperature $T_{NC} \approx 352$–360 K, in good agreement with previously reported values. At the lowest measured temperatures, the observation of a virtually clean gap without a redistribution of spectral weight from low to high energies below T_C argues for the existence of a Mott metal-insulator transition at a temperature of order 100 K. The magnitude of the gap is found to be $\Omega_{gap} \approx 170$–190 meV and has little symmetry, thus momentum, dependence, in agreement with earlier ARPES results [37]. At 200 K, on the high-temperature end of the C-CDW phase, the gap shrinks to ~60% of its low-temperature value. Additionally, the progressive filling of the CDW gaps by thermal excitations is tracked via the initial slope of the spectra, and indicates that the Mott gap opens primarily on the parts of the Fermi surface closest to the Γ point.

Our results demonstrate the potential of using inelastic light scattering to probe the momentum dependence and energy scale of changes in the electronic structure driven by low-temperature collective quantum phenomena. This opens perspectives to investigate the effect of hybridization on collective quantum phenomena in heterostructures composed of different 2D materials, e.g., alternating T and H monolayers as in the $4Hb$-TaS_2 phase [47].

ACKNOWLEDGMENTS

The authors acknowledge funding provided by the Institute of Physics Belgrade through the grant by the Ministry of Education, Science and Technological Development of the Republic of Serbia. The work was supported by the Science Fund of the Republic of Serbia, PROMIS, No. 6062656, StrainedFeSC, and by Research Foundation-Flanders (FWO). J.B. acknowledges support of a postdoctoral fellowship of the FWO, and of the Erasmus + program for staff mobility and training (KA107, 2018) for a research stay at the Institute of Physics Belgrade, during which part of the work was carried out. The computational resources and services used for the first-principles calculations in this work were provided by the VSC (Flemish Supercomputer Center), funded by the

FWO and the Flemish Government – department EWI. Work at Brookhaven is supported by the U.S. DOE under Contract No. DESC0012704. A.B. and R.H. acknowledge support by the German research foundation (DFG) via Projects No. Ha2071/12-1 and No. 107745057 – TRR 80 and by the DAAD via the project-related personal exchange program PPP with Serbia Grant No. 57449106.

APPENDIX A: RAW DATA

Figure 5 shows Raman spectra at temperatures ranging from $T = 4$ to 370 K for parallel [Fig. 5(a)] and crossed [Fig. 5(b)] in-plane light polarizations. The spectra were measured in steps of $\Delta\Omega = 50\ \mathrm{cm}^{-1}$ and a resolution of $\sigma \approx 20\ \mathrm{cm}^{-1}$. Therefore neither the shapes nor the positions of the phonon lines below 500 cm^{-1} may be resolved. All spectra reach a minimum in the range from 500 to 1600 cm^{-1}. At energies above 500 cm^{-1} the overall intensities are strongly temperature dependent and decreasing with decreasing temperature. Three clusters of spectra are well separated according to the phases they belong to.

In the C-CDW phase ($T \leqslant 200$ K, blue lines) the spectra start to develop substructures at 1500 and 3000 cm^{-1}. The spectra at 200 K increase almost linearly with energy. The spectra of the NC- and IC-CDW phases exhibit a broad maximum centered in the region of 2200–3200 cm^{-1} which may be attributed to luminescence (see Appendix B). For clarification we measured a few spectra with various laser lines for excitation.

APPENDIX B: LUMINESCENCE

Figure 6 shows Raman spectra measured with parallel light polarizations for three different wavelengths λ_i of the incident laser light. Figures 6(a) and 6(b) depict the measured intensity I (without the Bose factor) as a function of the absolute frequency $\tilde{\nu}$ of the scattered light.

At high temperature [$T = 330$ K, Fig. 6(a)] a broad peak can be seen for all λ_i which is centered at a fixed frequency of 15 200 cm^{-1} of the scattered photons (gray shaded area). The peak intensity decreases for increasing λ_i (decreasing energy). Correspondingly, this peak's center depends on the laser wavelength in the spectra shown as a function of the Raman shift [Fig. 6(c)]. This behavior indicates that the origin of this excitation is likely to be luminescence where transitions at fixed absolute final frequencies are expected.

At low temperature [Fig. 6(b)] we can no longer find a structure at a fixed absolute energy. Rather, as already indicated in the main part, the spectra develop additional, yet weak, structures which are observable in all spectra but are particularly pronounced for blue excitation. For green and yellow excitation the spectral range of the spectrometer, limited to 732 nm, is not wide enough for a deeper insight into the luminescence contributions (at energies different from those at high temperature) and no maximum common to all three spectra is observed. If these spectra are plotted as a function of the Raman shift, the changes in slope at 1500 and 3000 cm^{-1} are found to be in the same position for all λ_i, values thus arguing for inelastic scattering rather than luminescence. Since we do currently not have the appropriate experimental tools for an in-depth study, our interpretation is preliminary although supported by the observations in Fig. 6(d).

As shown in the inset of Fig. 6(d) we propose a scenario on the basis of Mott physics. In the C-CDW phase the reduced bandwidth is no longer the largest energy and the Coulomb repulsion U becomes relevant [22] and splits the conduction band into a lower and upper Hubbard band. We assume that the onset of scattering at 1500 cm^{-1} corresponds to the distance of the highest energy of the lower Hubbard band to the Fermi energy E_F. The second onset corresponds then to the distance between the highest energy of the lower Hubbard band and the lowest energy of the upper Hubbard band. An important question needs to be answered: Into which unoccupied states right above E_F does the first process scatter electrons? We may speculate that some DOS is provided by the metallic band dispersing along k_z or by the metallic domain walls between the different types of ordering patterns along the c axis observed recently by tunneling spectroscopy [46]. These quasi-1D domain walls would provide the states required for the onset of scattering at high energy but are topologically too small for providing enough density of states for a measurable intensity at low energy [Fig. 4(g)] in a location-integrated experiment such as Raman scattering.

APPENDIX C: DERIVATION OF THE RAMAN VERTICES

Phenomenologically, the Raman vertices can be derived based on lattice symmetry, which are proportional to the Brillouin zone harmonics. They are a set of functions that exhibit the symmetry and periodicity of the lattice structure proposed by Allen [48]. These functions make the k-space sums and energy integrals more convenient than that of the Cartesian basis or the spherical harmonics basis, especially for those materials who have anisotropic and/or multiple Fermi pockets. The three Cartesian components of the Fermi velocity v_k are recommended to generate this set of functions since they inherit the symmetry and periodicity of the crystal lattice naturally. However, in most cases, we do not know the details of band dispersion. A phenomenological method is needed to construct such a set of basis functions. Here, we demonstrate a method based on the group theory. The Brillouin zone harmonics can be obtained by the projection operation on specific trial functions.

For a certain group G with symmetry elements R and symmetry operators $\hat{P}_R$, it can be described by several irreducible representations Γ_n, where n labels the representation. For each irreducible representation, there are corresponding basis functions $\Phi^j_{\Gamma_n}$ that can be used to generate representation matrices for a particular symmetry. Here, j labels the component or partner of the representations. For an arbitrary function F, we have

$$F = \sum_{\Gamma_n} \sum_j f_j^{\Gamma_n} \Phi^j_{\Gamma_n}. \tag{C1}$$

According to the group theory, we can always define a projection operator by the relation [49]

$$\hat{P}^{\Gamma_n} = \frac{d}{N} \sum_R \chi^{\Gamma_n}(R) * \hat{P}_R, \tag{C2}$$

TABLE III. Symmetry operations $\hat{P}_R$ and corresponding character table of theD_{3d} point group.

$\hat{P}_R$	x'	y'	z'	$\chi^{\Gamma_n}(R)$	
				A_{1g}	E_g
E	x	y	z	1	2
C_3^1	$-\frac{1}{2}x+\frac{\sqrt{3}}{2}y$	$-\frac{\sqrt{3}}{2}x-\frac{1}{2}y$	z	1	-1
C_3^{-1}	$-\frac{1}{2}x-\frac{\sqrt{3}}{2}y$	$\frac{\sqrt{3}}{2}x-\frac{1}{2}y$	z	1	-1
C_2'	x	$-y$	$-z$	1	0
C_2''	$-\frac{1}{2}x+\frac{\sqrt{3}}{2}y$	$\frac{\sqrt{3}}{2}x+\frac{1}{2}y$	$-z$	1	0
C_2'''	$-\frac{1}{2}x-\frac{\sqrt{3}}{2}y$	$-\frac{\sqrt{3}}{2}x+\frac{1}{2}y$	$-z$	1	0
I	$-x$	$-y$	$-z$	1	2
S_6^1	$\frac{1}{2}x-\frac{\sqrt{3}}{2}y$	$\frac{\sqrt{3}}{2}x+\frac{1}{2}y$	$-z$	1	-1
S_6^{-1}	$\frac{1}{2}x+\frac{\sqrt{3}}{2}y$	$-\frac{\sqrt{3}}{2}x+\frac{1}{2}y$	$-z$	1	-1
σ_v'	$-x$	y	z	1	0
σ_v''	$\frac{1}{2}x-\frac{\sqrt{3}}{2}y$	$-\frac{\sqrt{3}}{2}x-\frac{1}{2}y$	z	1	0
σ_v'''	$\frac{1}{2}x+\frac{\sqrt{3}}{2}y$	$\frac{\sqrt{3}}{2}x-\frac{1}{2}y$	z	1	0

that satisfies the relation

$$\hat{P}^{\Gamma_n}F=\sum_j f_j^{\Gamma_n}\Phi_{\Gamma_n}^j, \tag{C3}$$

where d is the dimensionality of the irreducible representation Γ_n, N is the number of symmetry operators in the group, and $\chi^{\Gamma_n}(R)$ is the character of the matrix of symmetry operator R in irreducible representation Γ_n. By projection operation on a certain irreducible representation Γ_n, we can directly get its basis functions $\Phi_{\Gamma_n}^j$.

The basis functions are not unique. In specific physical problems, it is useful to use physical insight to guess an appropriate arbitrary function to find the basis functions for specific problems. $1T$-TaS_2 belongs to the D_{3d} point group. There are 12 symmetry operators in this group, i.e., E, C_3^1, C_3^{-1}, C_2', C_2'', C_2''', I, S_6^1, S_6^{-1}, σ_v', σ_v'', σ_v'''. The coordinate transformations after symmetry operations and the corresponding character table are listed in Table III.

In order to simulate the periodicity of the Brillouin zone, trigonometric functions are used as trial functions. According to the parity of the irreducible representations, we can choose an appropriate trigonometric function, e.g., a sine function for odd parity representation and cosine function for even parity representation. The combinations of them are also available.

Here, we use $F=\cos(k_x a)$ as a trial function, where a is the in-plane crystal constant. The basis function of A_{1g} can be derived as

$$\Phi_{A_{1g}}(\mathbf{k})=\frac{1}{3}\left[\cos(k_x a)+2\cos\left(\frac{1}{2}k_x a\right)\cos\left(\frac{\sqrt{3}}{2}k_y a\right)\right]. \tag{C4}$$

With the same method, we obtain a basis function of E_g as

$$\Phi_{E_g^1}(\mathbf{k})=\frac{2}{3}\left[\cos(k_x a)-\cos\left(\frac{1}{2}k_x a\right)\cos\left(\frac{\sqrt{3}}{2}k_y a\right)\right]. \tag{C5}$$

Since the E_g is a two-dimensional representation, the projection operation provides only one of the two basis functions of the corresponding subspace. The second function is found based on the subspace invariance under the symmetry operations (e.g., if we operate $\Phi_{E_g^1}$ with C_3^1 symmetry, the result can be presented as a linear combination of $\Phi_{E_g^1}$ and $\Phi_{E_g^2}$). Thus we obtain

$$\Phi_{E_g^2}(\mathbf{k})=2\sin\left(\frac{1}{2}k_x a\right)\sin\left(\frac{\sqrt{3}}{2}k_y a\right). \tag{C6}$$

[1] J. C. Tsang, J. E. Smith, M. W. Shafer, and S. F. Meyer, Raman spectroscopy of the charge-density-wave state in $1T$- and $2H$-$TaSe_2$, Phys. Rev. B **16**, 4239 (1977).

[2] C. J. Sayers, H. Hedayat, A. Ceraso, F. Museur, M. Cattelan, L. S. Hart, L. S. Farrar, S. Dal Conte, G. Cerullo, C. Dallera, E. Da Como, and E. Carpene, Coherent phonons and the interplay between charge density wave and Mott phases in $1T$-$TaSe_2$, Phys. Rev. B **102**, 161105(R) (2020).

[3] A. J. Wilson, J. F. D. Salvo, and S. Mahajan, Charge-density waves and superlattices in the metallic layered transition metal dichalcogenides, Adv. Phys. **24**, 117 (1975).

[4] C. B. Scruby, P. M. Williams, and G. S. Parry, The role of charge density waves in structural transformations of $1T$-TaS_2, Philos. Mag. **31**, 255 (1975).

[5] R. E. Thomson, B. Burk, A. Zettl, and J. Clarke, Scanning tunneling microscopy of the charge-density-wave structure in $1T$-TaS_2, Phys. Rev. B **49**, 16899 (1994).

[6] W. Wen, C. Dang, and L. Xie, Photoinduced phase transitions in two-dimensional charge-density-wave $1T$-TaS_2, Chin. Phys. B **28**, 058504 (2019).

[7] D. Svetin, I. Vaskivskyi, S. Brazovskii, Mertelj, and D. Mihailovic, Three-dimensional resistivity and switching between correlated electronic states in $1T$-TaS_2, Sci. Rep. **7**, 46048 (2017).

[8] D. Svetin, I. Vaskivskyi, P. Sutar, E. Goreshnik, J. Gospodaric, T. Mertelj, and D. Mihailovic, Transitions between photoinduced macroscopic quantum states in $1T$-TaS_2 controlled by substrate strain, Appl. Phys. Express **7**, 103201 (2014).

[9] G. Liu, B. Debnath, T. R. Pope, T. T. Salguero, R. K. Lake, and A. A. Balandin, A charge-density wave oscillator based on an integrated tantalum disulfide-boron nitride-graphene device operating at room temperature, Nat. Nanotechnol. **11**, 845 (2016).

[10] R. Salgado, A. Mohammadzadeh, F. Kargar, A. Geremew, C.-Y. Huang, M. A. Bloodgood, S. Rumyantsev, T. T. Salguero, and A. A. Balandin, Low-frequency noise spectroscopy of charge-density-wave phase transitions in vertical quasi-2D $1T$-TaS_2 devices, Appl. Phys. Express **12**, 037001 (2019).

[11] Z. X. Wang, Q. M. Liu, L. Y. Shi, S. J. Zhang, T. Lin, T. Dong, D. Wu, and N. L. Wang, Photoinduced hidden CDW state and relaxation dynamics of $1T$-TaS_2 probed by time-resolved terahertz spectroscopy, arXiv:1906.01500.

[12] L. Stojchevska, I. Vaskivskyi, T. Mertelj, P. Kusar, D. Svetin, S. Brazovskii, and D. Mihailovic, Ultrafast switching to a stable

hidden quantum state in an electronic crystal, Science **344**, 177 (2014).

[13] L. V. Gasparov, K. G. Brown, A. C. Wint, D. B. Tanner, H. Berger, G. Margaritondo, R. Gaál, and L. Forró, Phonon anomaly at the charge ordering transition in $1T$-TaS_2, Phys. Rev. B **66**, 094301 (2002).

[14] O. R. Albertini, R. Zhao, R. L. McCann, S. Feng, M. Terrones, J. K. Freericks, J. A. Robinson, and A. Y. Liu, Zone-center phonons of bulk, few-layer, and monolayer $1T$-TaS_2: Detection of commensurate charge density wave phase through Raman scattering, Phys. Rev. B **93**, 214109 (2016).

[15] S. Uchida and S. Sugai, Infrared and raman studies on a commensurate CDW states in transition metal dichalcogenides, Physica B+C **105**, 393 (1981).

[16] R. Brouwer and F. Jellinek, The low-temperature superstructures of $1T$-$TaSe_2$ and $2H$-$TaSe_2$, Physica B+C **99**, 51 (1980).

[17] A. Zong, X. Shen, A. Kogar, L. Ye, C. Marks, D. Chowdhury, T. Rohwer, B. Freelon, S. Weathersby, R. Li, J. Yang, J. Checkelsky, X. Wang, and N. Gedik, Ultrafast manipulation of mirror domain walls in a charge density wave, Sci. Adv. **4**, eaau5501 (2018).

[18] J. R. Duffay and R. D. Kirby, Raman scattering from $1T$-TaS_2, Solid State Commun. **20**, 617 (1976).

[19] T. Hirata and F. S. Ohuchi, Temperature dependence of the Raman spectra of $1T$-TaS_2, Solid State Commun. **117**, 361 (2001).

[20] S. L. L. M. Ramos, R. Plumadore, J. Boddison-Chouinard, S. W. Hla, J. R. Guest, D. J. Gosztola, M. A. Pimenta, and A. Luican-Mayer, Suppression of the commensurate charge density wave phase in ultrathin $1T$-TaS_2 evidenced by Raman hyperspectral analysis, Phys. Rev. B **100**, 165414 (2019).

[21] B. Sipos, A. F. Kusmartseva, A. Akrap, H. Berger, L. Forró, and E. Tutis, From Mott state to superconductivity in $1T$-TaS_2, Nat. Mater. **7**, 960 (2008).

[22] P. Fazekas and E. Tosatti, Electrical, structural and magnetic properties of pure and doped $1T$-TaS_2, Philos. Mag. B **39**, 229 (1979).

[23] E. Martino, A. Pisoni, L. Ćirić, A. Arakcheeva, H. Berger, A. Akrap, C. Putzke, P. J. W. Moll, I. Batistić, E. Tutiš, L. Forró, and K., Preferential out-of-plane conduction and quasi-one-dimensional electronic states in layered $1T$-TaS_2, npj 2D Mater. Appl. **4**, 7 (2020).

[24] P. Darancet, A. J. Millis, and C. A. Marianetti, Three-dimensional metallic and two-dimensional insulating behavior in octahedral tantalum dichalcogenides, Phys. Rev. B **90**, 045134 (2014).

[25] S.-H. Lee, J. S. Goh, and D. Cho, Origin of the Insulating Phase and First-Order Metal-Insulator Transition in $1T$-TaS_2, Phys. Rev. Lett. **122**, 106404 (2019).

[26] Y. Ma, Y. Hou, C. Lu, L. Li, and C. Petrovic, Possible origin of nonlinear conductivity and large dielectric constant in the commensurate charge-density-wave phase of $1T$-TaS_2, Phys. Rev. B **97**, 195117 (2018).

[27] L. J. Li, W. J. Lu, X. D. Zhu, L. S. Ling, Z. Qu, and Y. P. Sun, Fe-doping induced superconductivity in the charge-density-wave system $1T$-TaS_2, Europhys. Lett. **98**, 29902 (2012).

[28] Y. Liu, R. Ang, W. J. Lu, W. H. Song, L. J. Li, and Y. P. Sun, Superconductivity induced by Se-doping in layered charge-density-wave system $1T$-$TaS_{2-x}Se_x$, Appl. Phys. Lett. **102**, 192602 (2013).

[29] R. Ang, Y. Miyata, E. Ieki, K. Nakayama, T. Sato, Y. Liu, W. J. Lu, Y. P. Sun, and T. Takahashi, Superconductivity and bandwidth-controlled Mott metal-insulator transition in $1T$-$TaS_{2-x}Se_x$, Phys. Rev. B **88**, 115145 (2013).

[30] M. Bovet, D. Popović, F. Clerc, C. Koitzsch, U. Probst, E. Bucher, H. Berger, D. Naumović, and P. Aebi, Pseudogapped Fermi surfaces of $1T$-TaS_2 and $1T$-$TaSe_2$: A charge density wave effect, Phys. Rev. B **69**, 125117 (2004).

[31] X. Gonze, B. Amadon, P.-M. Anglade, J.-M. Beuken, F. Bottin, P. Boulanger, F. Bruneval, D. Caliste, R. Caracas, M. Côté, T. Deutsch, L. Genovese, P. Ghosez, M. Giantomassi, S. Goedecker, D. Hamann, P. Hermet, F. Jollet, G. Jomard, S. Leroux *et al.*, ABINIT: First-principles approach to material and nanosystem properties, Comput. Phys. Commun. **180**, 2582 (2009).

[32] S. Goedecker, M. Teter, and J. Hutter, Separable dual-space Gaussian pseudopotentials, Phys. Rev. B **54**, 1703 (1996).

[33] M. Krack, Pseudopotentials for H to Kr optimized for gradient-corrected exchange-correlation functionals, Theor. Chem. Acc. **114**, 145 (2005).

[34] X. Gonze, D. C. Allan, and M. P. Teter, Dielectric Tensor, Effective Charges, and Phonons in α-Quartz by Variational Density-Functional Perturbation Theory, Phys. Rev. Lett. **68**, 3603 (1992).

[35] A. Zawadowski and M. Cardona, Theory of Raman scattering on normal metals with impurities, Phys. Rev. B **42**, 10732 (1990).

[36] N. Lazarević and R. Hackl, Fluctuations and pairing in Fe-based superconductors: Light scattering experiments, J. Phys.: Condens. Matter **32**, 413001 (2020).

[37] K. Rossnagel, On the origin of charge-density waves in select layered transition-metal dichalcogenides, J. Phys.: Condens. Matter **23**, 213001 (2011).

[38] R. Shuker and R. W. Gammon, Raman-Scattering Selection-Rule Breaking and the Density of States in Amorphous Materials, Phys. Rev. Lett. **25**, 222 (1970).

[39] A. Baum, A. Milosavljević, N. Lazarević, M. M. Radonjić, B. Nikolić, M. Mitschek, Z. I. Maranloo, M. Šćepanović, M. Grujić-Brojčin, N. Stojilović, M. Opel, A. Wang, C. Petrovic, Z. V. Popović, and R. Hackl, Phonon anomalies in FeS, Phys. Rev. B **97**, 054306 (2018).

[40] A. Spijkerman, J. L. de Boer, A. Meetsma, G. A. Wiegers, and S. van Smaalen, X-ray crystal-structure refinement of the nearly commensurate phase of $1T$-TaS_2 in $(3+2)$-dimensional superspace, Phys. Rev. B **56**, 13757 (1997).

[41] R. He, J. Okamoto, Z. Ye, G. Ye, H. Anderson, X. Dai, X. Wu, J. Hu, Y. Liu, W. Lu, Y. Sun, A. N. Pasupathy, and A. W. Tsen, Distinct surface and bulk charge density waves in ultrathin $1T$-TaS_2, Phys. Rev. B **94**, 201108(R) (2016).

[42] G. Grüner, The dynamics of charge-density waves, Rev. Mod. Phys. **60**, 1129 (1988).

[43] C. Sohrt, A. Stange, M. Bauer, and K. Rossnagel, How fast can a Peierls–Mott insulator be melted?, Faraday Discuss. **171**, 243 (2014).

[44] T. P. Devereaux and R. Hackl, Inelastic light scattering from correlated electrons, Rev. Mod. Phys. **79**, 175 (2007).

[45] M. Opel, R. Nemetschek, C. Hoffmann, R. Philipp, P. F. Müller, R. Hackl, I. Tüttő, A. Erb, B. Revaz, E. Walker, H. Berger, and L. Forró, Carrier relaxation, pseudogap, and superconducting

gap in high-T_c cuprates: A Raman scattering study, Phys. Rev. B **61**, 9752 (2000).

[46] J. Skolimowski, Y. Gerasimenko, and R. Žitko, Mottness Collapse without Metallization in the Domain Wall of the Triangular-Lattice Mott Insulator $1T$-TaS_2, Phys. Rev. Lett. **122**, 036802 (2019).

[47] A. Ribak, R. M. Skiff, M. Mograbi, P. K. Rout, M. H. Fischer, J. Ruhman, K. Chashka, Y. Dagan, and A. Kanigel, Chiral superconductivity in the alternate stacking compound $4Hb$-TaS_2, Sci. Adv. **6**, eaax9480 (2020).

[48] P. B. Allen, Fermi-surface harmonics: A general method for nonspherical problems. Application to Boltzmann and Eliashberg equations, Phys. Rev. B **13**, 1416 (1976).

[49] M. S. Dresselhaus, G. Dresselhaus, and A. Jorio, *Group Theory* (Springer, Berlin, 2008).

Inorganic Chemistry

pubs.acs.org/IC Article

Short-Range Order in VI_3

Sanja Djurdjić Mijin, A. M. Milinda Abeykoon, Andrijana Šolajić, Ana Milosavljević, Jelena Pešić, Yu Liu, Cedomir Petrovic, Zoran V. Popović, and Nenad Lazarević*

Cite This: https://dx.doi.org/10.1021/acs.inorgchem.0c02060 Read Online

ABSTRACT: We present a detailed investigation of the crystal structure of VI_3, a two-dimensional van der Waals material of interest for studies of low-dimensional magnetism. As opposed to the average crystal structure that features $R\bar{3}$ symmetry of the unit cell, our Raman scattering and X-ray atomic pair distribution function analysis supported by density functional theory calculations point to the coexistence of short-range ordered $P\bar{3}1c$ and long-range ordered $R\bar{3}$ phases. The highest-intensity peak, A^3_{1g}, exhibits a moderate asymmetry that might be traced back to the spin−phonon interactions, as in the case of CrI_3.

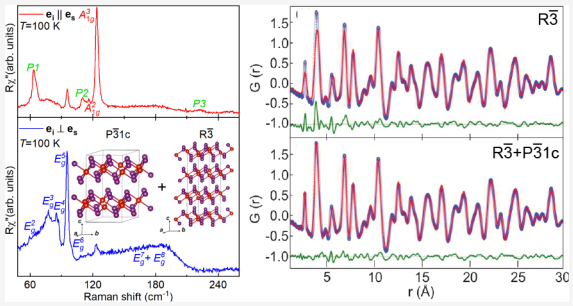

INTRODUCTION

A well-known family of transition metal trihalides (TMTs) MX_3 (X = Cr, B, or I) have received a great deal of attention due to potential existence of two-dimensional (2D) ferromagnetism,[1−6] which has been confirmed in CrI_3.[7,8] The similar crystal structure and magnetic properties of CrI_3 and VI_3 fostered a belief that the same might be found in the latter. In fact, magnetization measurements revealed the 2D ferromagnetic nature of VI_3 with a Currie temperature (T_c) of around 50 K.[9,10] Contrary to a layer-dependent ferromagnetism in CrI_3,[11] the first-principles calculations predict that ferromagnetism in VI_3 persists down to a single layer,[9] making it a suitable candidate for engineering 2D spintronic devices. Resistivity measurements showed VI_3 is an insulator with an optical band gap of ∼0.6 eV.[9,12]

Whereas laboratory X-ray diffraction studies reported three possible high-temperature VI_3 unit cell symmetries,[9,12−14] high-resolution synchrotron X-ray diffraction confirmed a rhombohedral $R\bar{3}$ space group.[10] A very recently published Raman spectroscopy study indicated that the VI_3 crystal structure can be described within the C_{2h} point group.[15] All results agree on the existence of a phase transition at a temperature of 79 K. However, the subtle[12] structural changes below 79 K are still under debate.

The long-range magnetic order in ultrathin 2D van der Waals (vdW) crystals stems from strong uniaxial anisotropy, in contrast to materials with isotropic exchange interactions where order parameters are forbidden.[16−18] 2D vdW magnetic materials are of interest both as examples of exotic magnetic order[19] and for potential applications in spintronic technology.[2,4,20,21]

Atomically thin flakes of $CrCl_3$ have a magnetic transition temperature that is different from that of bulk crystals possibly due to the different crystal structure of the monolayer and ultrathin crystals when compared to bulk.[22,23] Similar observations were made on CrI_3 monolayers.[22,24,25] It has been proposed[23] that the second anomaly in heat capacity in bulk $CrCl_3$ arises due to regions close to the surface that host a different crystal structure when compared to bulk;[26,27] however, due to the substantial mass fraction detected in heat capacity measurements, this could also reflect differences between the short-range order and long-range crystallographic order of Bragg planes. The short-range order is determined by the space group that is energetically favorable for a monolayer or a few layers, whereas the long-range crystallographic order is established over large packing lengths.

In this paper, we present an experimental Raman scattering study of the bulk VI_3 high-temperature structure, supported by density functional theory (DFT) calculations and the X-ray atomic pair distribution function (PDF) analysis. The comparison between the Raman experiment and DFT calculations for each of the previously reported space groups suggested that the high-temperature lattice vibrations of bulk VI_3 are consistent with a $P\bar{3}1c$ trigonal structure. Nine ($2A_{1g}$ + $7E_g$) of 12 observed peaks were assigned on the basis of factor group analysis (FGA) and DFT calculations. The PDF analysis indicated the coexistence of two crystallographic phases at two different interatomic distances, short-range ordered $P\bar{3}1c$ and

Received: July 12, 2020

long-range ordered $R\bar{3}$, as two segregated phases and/or as randomly distributed short-range ordered $P\bar{3}1c$ domains in the long-range ordered $R\bar{3}$ lattice. Raman data displayed a moderate asymmetry of the A_{1g}^3 phonon line. This behavior was attributed to the spin−phonon interaction, similar to the case for CrI_3. The additional peaks in our spectra obey A_g selection rules and can be described in terms of overtones, as well as the A_{2g} silent modes "activated" by the symmetry breaking.

■ EXPERIMENTAL AND COMPUTATIONAL DETAILS

The preparation of single-crystal VI_3 samples used in this study is presented elsewhere.[10] For the Raman scattering experiment, a Tri Vista 557 spectrometer was used in the backscattering micro-Raman configuration with a 1800/1800/2400 grooves/mm diffraction grating combination. A Coherent Ar^+/Kr^+ ion laser with a 514 nm line was used as an excitation source. Laser beam focusing was achieved through the microscope objective with 50× magnification. The direction of the incident (scattered) light coincides with the crystallographic c axis. The sample, cleaved in open air, was held inside a KONTI CryoVac continuous helium flow cryostat with a 0.5 mm thick window. Raman scattering measurements were performed under high vacuum (10^{-6} mbar). All of the obtained Raman spectra were corrected by the Bose factor. The spectrometer resolution is comparable to the Gaussian width of 1 cm^{-1}.

PDF and wide-angle X-ray scattering measurements were carried out in capillary transmission geometry using a PerkinElmer amorphous silicon area detector placed 206 and 983 mm downstream from the sample, respectively, at beamline 28-ID-1 (PDF) of National Synchrotron Light Source II at Brookhaven National Laboratory. The setup utilized a 74.3 keV (λ = 0.1668 Å) X-ray beam.

Two-dimensional diffraction data were integrated using the Fit2D software package.[28] Data reduction was performed to obtain experimental PDFs (Q_{max} = $26A^{-1}$) using the xPDFsuite software package.[29] The Rietveld and PDF analyses were carried out using GSAS-II[30] and PDFgui[31] software packages, respectively.

Density functional theory calculations were performed using the Quantum Espresso software package,[32] employing the PBE exchange-correlation functional[33] and PAW pseudopotentials.[34,35] All calculations are spin-polarized. The cutoff for wave functions and the charge density were set to 48 and 650 Ry, respectively. The k-points were sampled using the Monkhorst−Pack scheme, on a 6 × 6 × 6 Γ-centered grid for $R\bar{3}$ and $C2/m$ structures and a 12 × 12 × 8 grid for the $P\bar{3}1c$ structure. Optimization of the lattice parameters and atomic positions in the unit cell was performed until the interatomic forces were <10^{-6} Ry/Å. To obtain more accurate lattice parameters, treatment of the van der Waals interactions is included using the Grimme-D2 correction. The correlation effects are treated with the Hubbard U correction (LDA+U), using a rotationally invariant formulation implemented in QE,[36] where U = 3.68 eV. Band structure plots are calculated at 800 k-points on the chosen path over high-symmetry points. Phonon frequencies were calculated with the linear response method, as implemented in the -honon part of Quantum Espresso.

■ RESULTS AND DISCUSSION

The first reported results for VI_3, dating from the 1950s,[37−39] indicated that VI_3 adopts a honeycomb layer-type BiI_3 structure described with space group $R\bar{3}$, which is a structure common in TMTs, also found in the low-temperature phase of CrI_3.[6,40]

There have been several proposed unit cell symmetries for VI_3 in the literature: $R\bar{3}$,[12,13] $C2/m$,[14] and $P\bar{3}1c$.[9] Schematic representations of the $P\bar{3}1c$, $R\bar{3}$, and $C2/m$ crystal structures are depicted in Figure 1. The corresponding crystallographic unit cell parameters, previously reported, are listed in Table 1.

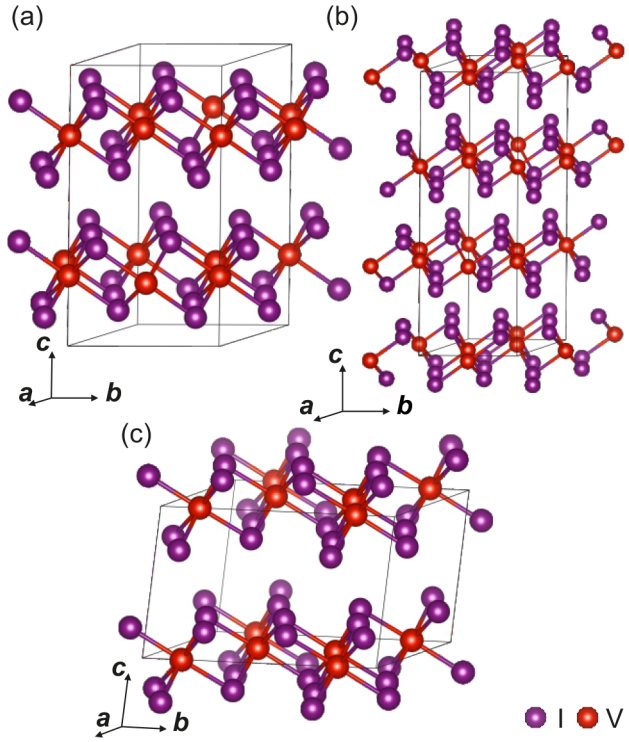

Figure 1. Schematic representation of the high-temperature (a) $P\bar{3}1c$, (b) $R\bar{3}$, and (c) $C2/m$ structures of VI_3. Black solid lines represent unit cells.

Each of the suggested symmetries implies a different distribution of Raman active modes.

According to FGA, eight ($4A_g$ + $4E_g$), 11 ($3A_{1g}$ + $8E_g$), and 12 ($6A_g$ + $6B_g$) Raman active modes are expected to be observed in the light scattering experiment for $R\bar{3}$, $P\bar{3}1c$, and $C2/m$ crystal structures, respectively. Wyckoff positions, irreducible representations, and corresponding tensors of Raman active modes for each space group are listed in Table 2.

The first step in determining the crystal symmetry from the light scattering experiment is to compare the expected and observed Raman active modes, shown in Figure 2. The red solid line represents the spectrum measured in the parallel polarization configuration, whereas the blue line corresponds to the cross polarization configuration. Five of 12 observed peaks emerge only in parallel, whereas five peaks and a broad peak-like structure can be observed for both polarization configurations. The emergence of the 123.4 cm^{-1} peak in the cross polarization can be understood as a "leakage" of the A_{1g}^3 mode due to a possible finite c axis projection and/or the presence of defects.

Now the peaks that appear only for the parallel polarization configuration can be assigned as either A_{1g} or A_g symmetry modes, assuming the light polarization direction along the main crystal axis of the $C2/m$ structure for the later. On the basis of the FGA for possible symmetry group candidates, the remaining Raman active modes can be either of E_g or B_g symmetry. The selection rules (Table 2) do not allow observation of the B_g symmetry modes for the parallel polarization configuration. Consequently, the peaks that can be observed in both scattering channels were recognized as E_g modes. The absence of B_g modes in the Raman spectra rules out the possibility of the $AlCl_3$ type of structure (space group $C2/m$). Two possible remaining crystal symmetries ($R\bar{3}$ and

https://dx.doi.org/10.1021/acs.inorgchem.0c02060
Inorg. Chem. XXXX, XXX, XXX−XXX

Table 1. Previously Reported Experimental and Calculated Unit Cell Parameters for $P\bar{3}1c$, $R\bar{3}$, and $C2/m$ Structures of VI_3

	$P\bar{3}1c$		$R\bar{3}$		$C2/m$	
	calcd	exp.[9]	calcd	exp.[12]	calcd	exp.[14]
a (Å)	6.87	6.89(10)	6.69	6.89(3)	7.01	6.84(3)
b (Å)	6.87	6.89(10)	6.69	6.89(3)	12.14	11.83(6)
c (Å)	13.224	13.289(1)	19.81	19.81(9)	7.01	6.95(4)
α (deg)	90	90	90	90	90	90
β (deg)	90	90	90	90	109.05	108.68
γ (deg)	120	120	120	120	90	90
cell volume (Å^3)	559.62	547.74(10)	767.71	814.09(8)	563.33	533.66(36)

Table 2. Wyckoff Positions of Atoms and Their Contributions to the Γ-Point Phonons for the $R\bar{3}$, $C2/m$, and $P\bar{3}1c$ Structures and the Raman Tensors for the Corresponding Space Groups

space group $P\bar{3}1c$		space group $R\bar{3}$		space group $C2/m$	
atom	irreducible representation	atom	irreducible representation	atom	irreducible representation
V (2a)	$A_{2g} + A_{2u} + E_g + E_u$	V (3a)		V (4g)	$A_g + A_u + 2B_g + 2B_u$
V (2c)	$A_{2g} + A_{2u} + E_g + E_u$	V (6c)	$A_g + A_u + E_g + E_u$	I (4i)	$2A_g + A_u + B_g + 2B_u$
I (12i)	$3A_{1g} + 3A_{1u} + 3A_{2g} + 3A_{2u} + 6E_g + 6E_u$	I (18f)	$3A_g + 3A_u + 3E_g + 3E_u$	I (8j)	$3A_g + 3A_u + 3B_g + 3B_u$

$$A_{1g} = \begin{pmatrix} a & & \\ & a & \\ & & b \end{pmatrix} \qquad A_g = \begin{pmatrix} a & & \\ & a & \\ & & b \end{pmatrix} \qquad A_g = \begin{pmatrix} a & & d \\ & c & \\ d & & b \end{pmatrix}$$

$$^1E_g = \begin{pmatrix} c & & \\ & -c & d \\ & d & \end{pmatrix} \; ^2E_g = \begin{pmatrix} & -c & -d \\ -c & & \\ d & & \end{pmatrix} \qquad ^1E_g = \begin{pmatrix} c & d & e \\ d & -c & f \\ e & f & \end{pmatrix} \; ^2E_g = \begin{pmatrix} d & -c & -f \\ -c & -d & e \\ -f & e & \end{pmatrix} \qquad B_g = \begin{pmatrix} & e & \\ e & & f \\ & f & \end{pmatrix}$$

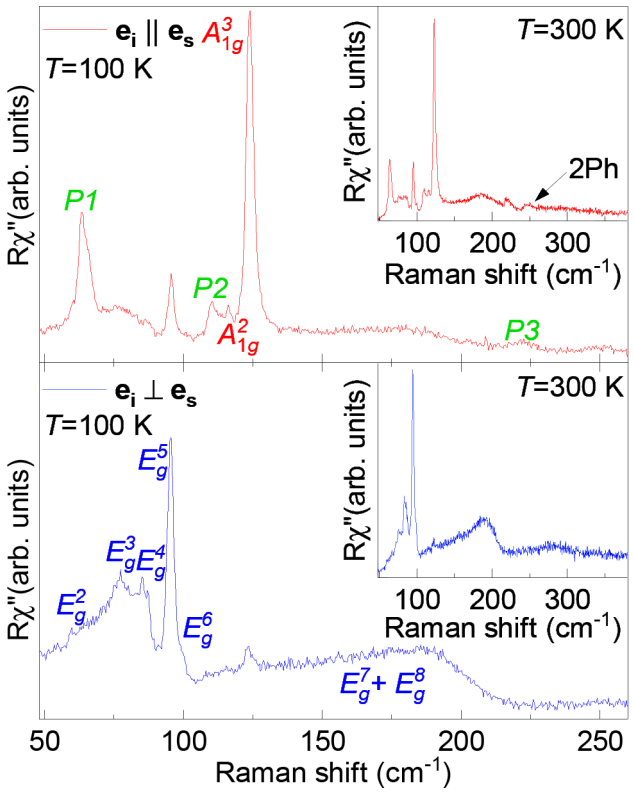

Figure 2. Raman spectra of the high-temperature VI_3 single-crystal structure measured in parallel (red solid line) and cross (blue solid line) polarization configurations at 100 K. Peaks observed in both spectra were identified as E_g modes, whereas peaks observed only in the red spectrum were assigned as A_{1g} modes. Additional peaks that obey pure A_{1g} symmetry are marked as $P1-P3$.

$P\bar{3}1c$) are difficult to single out on the basis of the Raman data symmetry analysis alone. To overcome this obstacle, the DFT method was applied for each of the suggested structures.

It was reported in the literature that $P\bar{3}1c$ VI_3 can have two possible electronic states[9,14,41−43] that both can be obtained using DFT+U calculations by varying the smearing and mixing parameters. This approach resulted in a Mott-insulator state having a lower energy making it the electronic ground state of VI_3. However, the total energy difference of these two states is small and will not be mentioned further because it is outside of the scope of our analysis. For the sake of completeness, both sets of phonon energies obtained through DFT calculations for these electronic states of the $P\bar{3}1c$ structure are listed in Table 3 together with the results for the $R\bar{3}$ and $C2/m$ space groups as well as the experimental results measured at 100 K.

Now one can see that, even though the Raman mode symmetries for the case of the $R\bar{3}$ crystal structure can describe our Raman spectra, there is a stronger mismatch in calculated and experimentally determined phonon energies when compared to the results obtained for the $P\bar{3}1c$ structure. The deviation is largest for the calculated A_g^1 mode. The closest mode in energy, which obeys the same symmetry rules as the calculated A_g^1, is a peak at ∼64.1 cm^{-1}, yielding a deviation of ∼30%. Also, the calculated energy of the A_g^4 mode could not be identified within our spectrum, with the closest experimental A_g peaks being within 20%. Such deviation in theory and experiment, >20%, indicates that the room-temperature phonon vibrations in VI_3 do not originate predominantly from the BiI_3 structure type either, leaving $P\bar{3}1c$ as the only candidate. This indication is further reinforced by the inability to connect the experimentally observed E_g modes at ∼77 and ∼86 cm^{-1} with the $R\bar{3}$-calculated modes.

Our experimental data (Table 3) are mostly supported by the phonon energies obtained for possible electronic states of

https://dx.doi.org/10.1021/acs.inorgchem.0c02060
Inorg. Chem. XXXX, XXX, XXX−XXX

Table 3. Comparison between Calculated Values of Raman Active Phonon Energies for Insulating and Half-Metallic States of the $P\bar{3}1c$ Structure and Experimentally Obtained Values (left)[a] and Phonon Symmetries and Calculated Phonon Energies for the $R\bar{3}$ and $C2/m$ Structures of VI_3[b]

space group $P\bar{3}1c$				space group $R\bar{3}$		space group $C2/m$	
symmetry	calcd (cm^{-1})	calcd (cm^{-1})	exp. (cm^{-1})	symmetry	calcd (cm^{-1})	symmetry	calcd (cm^{-1})
E_g^1	17.2	15.2	–	E_g^1	45.2	A_g^1	58.1
A_{2g}^1 (silent)	35.0	56.8		E_g^2	69.9	B_g^1	60.0
E_g^2	62.2	61.6	59.8	A_g^1	99.3	A_g^2	82.7
A_{2g}^2 (silent)	69.4	72.3		E_g^3	99.8	B_g^2	82.9
E_g^3	74.1	75.9	77.2	A_g^2	105.1	A_g^3	85.7
A_{1g}^1	83.3	84.2	–	A_g^3	135.5	B_g^3	88.9
E_g^4	84.9	86.6	86.7	A_g^4	167.9	A_g^4	99.3
E_g^5	91.5	98.4	95.2	E_g^4	176.8	B_g^4	99.3
A_{2g}^3 (silent)	92.2	96.3				A_g^5	122.3
E_g^6	97.4	108.3	100.4			B_g^5	149.9
A_{1g}^2	113.2	119.3	116.8			B_g^6	161.0
A_{1g}^3	117.1	123.9	123.4			A_g^6	164.0
A_{2g}^4 (silent)	121.3	147.8					
E_g^7	132.2	151.9	c				
E_g^8	149.4	166.9	c				
A_{2g}^5 (silent)	185.9	212.1					

[a]The experimental values were determined at 100 K. The experimental uncertainty is 0.3 cm^{-1}. [b]All calculations were performed at 0 K. [c]See the text for an explanation.

the $P\bar{3}1c$ trigonal structure with deviations of around 10% and 15%. Nine of 11 Raman modes were singled out and identified, with E_g^1 being not observable in our experimental setup due to its low energy. The A_{1g}^1 mode might be missing due to its low intensity and/or the finite spectrometer resolution. The most striking was the observation of the broad feature at ~180 cm^{-1}, persisting up to 300 K in both scattering channels. Whereas its line shape resembles those of the two-magnon type of excitation, we believe that scenario is unlikely for a ferromagnetic material. The energy region where the feature was observed may also suggest the possibility of a two-phonon type of excitation. However, their scattering cross sections are usually small and dominated by overtones, thus mostly observed for the parallel scattering configuration.[45] For example, such an excitation was observed at ~250 cm^{-1} (Figure 2). Finally, the observed feature also falls into the energy region where, as suggested by the numerical calculations, observation of the E_g^7 and E_g^8 modes is expected. We believe that it is actually a complex structure comprising E_g^7 and E_g^8 Raman modes, significantly broadened by the spin−phonon interaction, that is particularly strong on these phonon branches. The proximity of the two very broad, presumably asymmetric peaks hampers their precise assignment.

Closer inspection of other Raman peaks revealed that some of them also exhibit an asymmetric line shape. To further demonstrate this virtue, we have quantitatively analyzed the highest-intensity peak, A_{1g}^3, using the symmetric Voigt line shape and convolution of a Fano profile and a Gausian.[44−46] The asymmetric line shape (with a Fano parameter of $|q|$ = 12.3) gives a slightly better agreement with the experimental data, as depicted in Figure 3. Considering that the observed asymmetry in similar materials was shown to reflect the spin−phonon interaction,[46,47] we propose it as a possible scenario in VI_3, as well.

Our findings, based on the inelastic light scattering experiments, at first glance differ from those presented in ref 10. To resolve this discrepancy, we used synchrotron X-ray Rietveld and PDF analysis. Typically, the short-range order

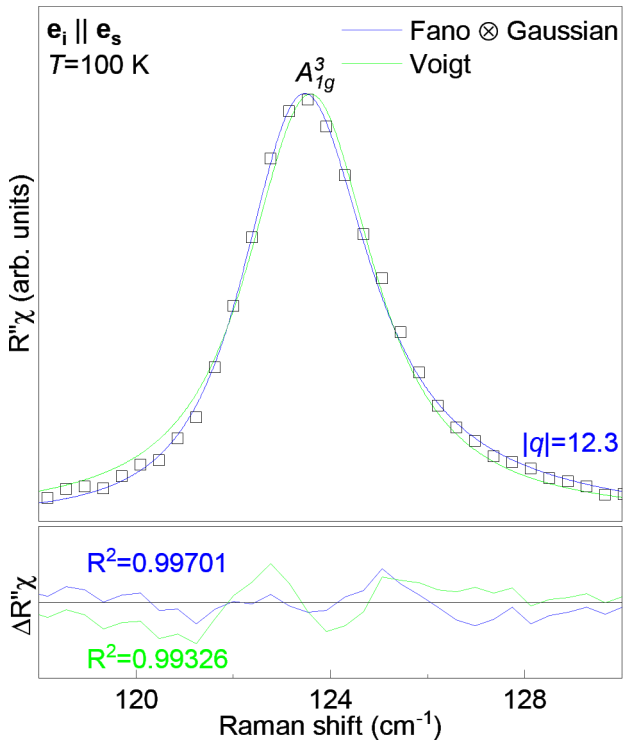

Figure 3. Quantitative analysis of the A_{1g}^3 mode. The blue solid line represents the line shape obtained as a convolution of the Fano line shape and the Gaussian, whereas the green one represents a Voigt profile fitted to experimental data (□). For details, see refs 44 and 45.

(SRO) contributes to diffuse scattering under the long-range order (LRO) Bragg peaks when they coexist. Because the diffuse scattering is subtracted as part of the background in the Rietveld refinement, this method is more sensitive to the average structure of materials. In contrast, PDF analysis is performed on the sine Fourier transform of the properly corrected diffraction patten, including both Bragg and diffuse

https://dx.doi.org/10.1021/acs.inorgchem.0c02060
Inorg. Chem. XXXX, XXX, XXX−XXX

components. PDF is a real space function that provides a histogram of interatomic distances, which contain information regarding all length scales.[48−51] The 1−10 and 11−30 Å PDF length scales are more sensitive to SRO and LRO, respectively. For the VI_3 system, the best Rietveld fit was obtained using the $R\bar{3}$ space group (Figure 4a), in agreement with that previously observed.[10] Not surprisngly, LRO obtained from the Rietveld refinement showed a good agreement on the PDF length scale of 10−30 Å. However, the $R\bar{3}$ space group gave a poor fit on the length scale of 1.5−15 Å with refined $\delta 1$ to account for correlated motion (Figure 4b). In contrast, $P\bar{3}1c$ gave a better fit to SRO, but a poor fit to LRO. The best PDF fits were obtained by refining a weighted two-phase structural model containing ∼25 wt % SRO $P\bar{3}1c$ and ∼75 wt % LRO $R\bar{3}$ phases. The refined correlation length of the SRO is ∼15−20 Å (Figure 4c). These results suggest two possible seanarios: (1) coexistence of two segregated phases, LRO $R\bar{3}$ and SRO $P\bar{3}1c$, and (2) randomly distributed short-range ordered $P\bar{3}1c$ domains in the long-range ordered $R\bar{3}$ lattice. A detailed structural analysis is required to pinpoint scenario 1 and/or 2, which is beyond the scope of this work.

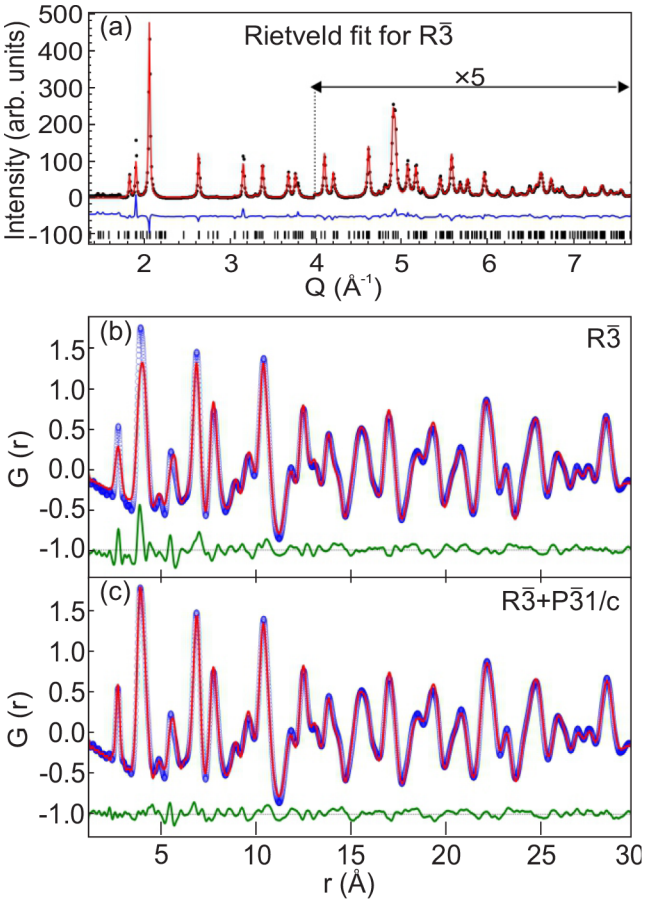

Figure 4. Best structural model fits to diffraction data. (a) Rietveld fit using the $R\bar{3}$ space group with black vertical bars indicating calculated peak positions. (b) PDF fit using the $R\bar{3}$ space group. (c) Two-phase PDF fit using $R\bar{3}$ and $P\bar{3}1c$ space groups to fit LRO and SRO, respectively. Black dots (XRD) and blue dots (PDF) represent experimental data, and red solid lines represent the model-based fits. The fit residues are shown at the bottom of each plot.

In addition to the peaks already assigned to Γ-point Raman active phonons of the $P\bar{3}1c$ crystal structure (Table 2), three additional peaks at 64.2 cm^{-1} ($P1$), 110.1 cm^{-1} ($P2$), and 220.6 cm^{-1} ($P3$) are observed (see Figure 2). According to the results of DFT, energies of these modes correspond well to those calculated for silent A_{2g}^2, A_{2g}^3, and A_{2g}^5 modes. Their observability in Raman data may come from the release of the symmetry selection rules by breaking of the (translation) symmetry as suggested by the PDF in both scenarios.[52−55] However, as previously discussed, these peaks obey A_{1g} selection rules, indicating the possibility for them to be overtones in nature. In this less likely scenario, the phonon−phonon coupling is enhanced by the spin−phonon interaction and/or by the structural imperfections, thus enhancing the Raman scattering rate for the two-phonon processes.[45] Hence, the observed Raman modes reflect the symmetry of phonon vibrations related to the SRO.[56,57] It is interesting to note that, besides a possible short-range crystallography that is different from the average, VI_3 might also feature short-range magnetic order above 79 K.[14]

CONCLUSION

In summary, room-temperature phonon vibrations of VI_3 stem from the $P\bar{3}1c$ symmetry of the unit cell. The PDF analysis suggested the coexistence of two phases, short-range ordered $P\bar{3}1c$ and long-range ordered $R\bar{3}$, as two segregated phases and/or as randomly distributed short-range ordered $P\bar{3}1c$ domains in the long-range ordered $R\bar{3}$ lattice. Nine of 12 observed peaks in the Raman spectra were assigned in agreement with $P\bar{3}1c$ symmetry calculations. Three additional peaks, which obey A_{1g} symmetry rules, could be explained as either overtones or as activated A_{2g} silent modes caused by a symmetry breaking. The asymmetry of one of the A_{1g} phonon modes, together with the anomalous behavior of E_g^7 and E_g^8, indicates strong spin−phonon coupling, which has already been reported in similar 2D materials.[46,58]

AUTHOR INFORMATION

Corresponding Author

Nenad Lazarević − *Institute of Physics Belgrade, University of Belgrade, 11080 Belgrade, Serbia;* orcid.org/0000-0001-6310-9511; Email: nenadl@ipb.ac.rs

Authors

Sanja Djurdjić Mijin − *Institute of Physics Belgrade, University of Belgrade, 11080 Belgrade, Serbia*

A. M. Milinda Abeykoon − *National Synchrotron Light Source II, Brookhaven National Laboratory, Upton, New York 11973, United States*

Andrijana Šolajić − *Institute of Physics Belgrade, University of Belgrade, 11080 Belgrade, Serbia*

Ana Milosavljević − *Institute of Physics Belgrade, University of Belgrade, 11080 Belgrade, Serbia*

Jelena Pešić − *Institute of Physics Belgrade, University of Belgrade, 11080 Belgrade, Serbia*

Yu Liu − *Condensed Matter Physics and Materials Science Department, Brookhaven National Laboratory, Upton, New York 11973-5000, United States;* orcid.org/0000-0001-8886-2876

Cedomir Petrovic − *Condensed Matter Physics and Materials Science Department, Brookhaven National Laboratory, Upton, New York 11973-5000, United States;* orcid.org/0000-0001-6063-1881

https://dx.doi.org/10.1021/acs.inorgchem.0c02060
Inorg. Chem. XXXX, XXX, XXX−XXX

Zoran V. Popović − *Institute of Physics Belgrade, University of Belgrade, 11080 Belgrade, Serbia; Serbian Academy of Sciences and Arts, 11000 Belgrade, Serbia*

Complete contact information is available at:
https://pubs.acs.org/10.1021/acs.inorgchem.0c02060

Notes

The authors declare no competing financial interest.

■ ACKNOWLEDGMENTS

The authors acknowledge funding provided by the Institute of Physics Belgrade, through a grant from the Ministry of Education, Science and Technological Development of the Republic of Serbia, Project F-134 of the Serbian Academy of Sciences and Arts, and the Science Fund of the Republic of Serbia, PROMIS, 6062656, StrainedFeSC. DFT calculations were performed using computational resources at Johannes Kepler University (Linz, Austria). Materials synthesis was supported by the U.S. DOE-BES, Division of Materials Science and Engineering, under Contract DE-SC0012704 (BNL). This research used beamline 28-ID-1 of National Synchrotron Light Source II, a U.S. DOE Office of Science User Facility operated for the DOE Office of Science by Brookhaven National Laboratory under Contract DE-S.

■ REFERENCES

(1) Seyler, K. L.; Zhong, D.; Klein, D. R.; et al. Ligand-field helical luminescence in a 2D ferromagnetic insulator. *Nat. Phys.* **2018**, *14*, 277−281.

(2) Klein, D. R.; MacNeill, D.; Lado, J. L.; Soriano, D.; Navarro-Moratalla, E.; Watanabe, K.; et al. Probing magnetism in 2D van der Waals crystalline insulators via electron tunneling. *Science* **2018**, *360*, 1218−1222.

(3) Huang, B.; Clark, G.; Klein, D. R.; MacNeill, D.; Navarro-Moratalla, E.; Seyler, K. L.; et al. Electrical control of 2D magnetism in bilayer CrI_3. *Nat. Nanotechnol.* **2018**, *13*, 544−548.

(4) Jiang, S.; Li, L.; Wang, Z.; Mak, K. F.; Shan, J. Controlling magnetism in 2D CrI_3 by electrostatic doping. *Nat. Nanotechnol.* **2018**, *13*, 549−553.

(5) McGuire, M. A.; Clark, G.; KC, S.; Chance, W. M.; Jellison, G. E.; Cooper, V. R.; Xu, X.; Sales, B. C. Magnetic behavior and spin-lattice coupling in cleavable van der Waals layered $CrCl_3$ crystals. *Phys. Rev. Materials* **2017**, *1*, 014001.

(6) Djurdjic-Mijin, S. D.; Šolajić, A.; Pešić, J.; Šćepanović, M.; Liu, Y.; Baum, A.; et al. Lattice dynamics and phase transition in CrI_3 single crystals. *Phys. Rev. B: Condens. Matter Mater. Phys.* **2018**, *98*, 104307.

(7) Thiel, L.; Wang, Z.; Tschudin, M.; Rohner, D.; Gutierrez-Lezama, I. G.; Ubrig, N.; et al. Probing magnetism in 2D materials at the nanoscale with single-spin microscopy. *Science* **2019**, *364*, 973−976.

(8) Lin, G. T.; Luo, X.; Chen, F. C.; Yan, J.; Gao, J. J.; Sun, Y.; et al. Critical behavior of two-dimensional intrinsically ferromagnetic semiconductor CrI_3. *Appl. Phys. Lett.* **2018**, *112*, 072405.

(9) Son, S.; Coak, M. J.; Lee, N.; Kim, J.; Kim, T. Y.; Hamidov, H.; et al. Bulk properties of the van der Waals hard ferromagnet VI_3. *Phys. Rev. B: Condens. Matter Mater. Phys.* **2019**, *99*, 041402.

(10) Liu, Y.; Abeykoon, M.; Petrovic, C. Critical behavior and magnetocaloric effect in VI_3. *Phys. Rev. Research* **2020**, *2*, 013013.

(11) Huang, B.; Clark, G.; Navarro-Moratalla, E.; Klein, D. R.; Cheng, R.; Seyler, K. L.; et al. Layer-dependent ferromagnetism in a van der Waals crystal down to the monolayer limit. *Nature* **2017**, *546*, 270−273.

(12) Kong, T.; Stolze, K.; Timmons, E. I.; Tao, J.; Ni, D.; Guo, S.; et al. VI_3 − a New Layered Ferromagnetic Semiconductor. *Adv. Mater.* **2019**, *31*, 1808074.

(13) Doležal, P.; Kratochvílová, M.; Holý, V.; Čermak, P.; Sechovský, V.; Dušek, M.; et al. Crystal structures and phase transitions of the van der Waals ferromagnet VI_3. *Phys. Rev. Materials* **2019**, *3*, 121401.

(14) Tian, S.; Zhang, J.-F.; Li, C.; Ying, T.; Li, S.; Zhang, X.; et al. Ferromagnetic van der Waals Crystal VI_3. *J. Am. Chem. Soc.* **2019**, *141*, 5326−5333.

(15) Wang, Y.-M.; Tian, S.-J.; Li, C.-H.; Jin, F.; Ji, J.-T.; Lei, H.-C.; Zhang, Q.-M. Raman scattering study of two-dimensional magnetic van der Waals compound VI_3. *Chin. Phys. B* **2020**, *29*, 056301.

(16) Lee, I.; Utermohlen, F. G.; Weber, D.; Hwang, K.; Zhang, C.; van Tol, J.; Goldberger, J. E.; Trivedi, N.; Hammel, P. C. Fundamental Spin Interactions Underlying the Magnetic Anisotropy in the Kitaev Ferromagnet CrI_3. *Phys. Rev. Lett.* **2020**, *124*, 017201.

(17) Xu, C.; Feng, J.; Xiang, H.; Bellaiche, L. Interplay between Kitaev interaction and single ion anisotropy in ferromagnetic CrI_3 and $CrGeTe_3$ monolayers. *npj Comput. Mater.* **2018**, *4*, 57.

(18) Mermin, N. D.; Wagner, H. Absence of Ferromagnetism or Antiferromagnetism in One- or Two-Dimensional Isotropic Heisenberg Models. *Phys. Rev. Lett.* **1966**, *17*, 1133−1136.

(19) Pershoguba, S. S.; Banerjee, S.; Lashley, J. C.; Park, J.; Ågren, H.; Aeppli, G.; Balatsky, A. V. Dirac Magnons in Honeycomb Ferromagnets. *Phys. Rev. X* **2018**, *8*, 011010.

(20) Liu, J.; Shi, M.; Mo, P.; Lu, J. Electrical-field-induced magnetic Skyrmion ground state in a two-dimensional chromium tri-iodide ferromagnetic monolayer. *AIP Adv.* **2018**, *8*, 055316.

(21) Jiang, S.; Li, L.; Wang, Z.; Shan, J.; Mak, K. Spin tunnel field-effect transistors based on two-dimensional van der Waals heterostructures. *Nature Electronics* **2019**, *2*, 159.

(22) Klein, D. R.; MacNeill, D.; Song, Q.; Larson, D. T.; Fang, S.; Xu, M.; Ribeiro, R. A.; Canfield, P. C.; Kaxiras, E.; Comin, R.; Jarillo-Herrero, P. Enhancement of interlayer exchange in an ultrathin two-dimensional magnet. *Nat. Phys.* **2019**, *15*, 1255−1260.

(23) Wang, Z.; Gibertini, M.; Dumcenco, D.; Taniguchi, T.; Watanabe, K.; Giannini, E.; Morpurgo, A. Determining the phase diagram of atomically thin layered antiferromagnet $CrCl_3$. *Nat. Nanotechnol.* **2019**, *14*, 1116.

(24) Ubrig, N.; Wang, Z.; Teyssier, J.; Taniguchi, T.; Watanabe, K.; Giannini, E.; Morpurgo, A. F.; Gibertini, M. Low-temperature monoclinic layer stacking in atomically thin CrI_3 crystals. *2D Mater.* **2020**, *7*, 015007.

(25) Sun, Z.; et al. Giant nonreciprocal second-harmonic generation from antiferromagnetic bilayer CrI_3. *Nature* **2019**, *572*, 497−501.

(26) McGuire, M. A.; Clark, G.; KC, S.; Chance, W. M.; Jellison, G. E.; Cooper, V. R.; Xu, X.; Sales, B. C. Magnetic behavior and spin-lattice coupling in cleavable van der Waals layered $CrCl_3$ crystals. *Phys. Rev. Materials* **2017**, *1*, 014001.

(27) Kuhlow, B. Magnetic Ordering in $CrCl_3$ at the Phase Transition. *physica status solidi (a)* **1982**, *72*, 161−168.

(28) Hammersley, A. P.; Svensson, S. O.; Hanfland, M.; Fitch, A. N.; Hausermann, D. Two-dimensional detector software: From real detector to idealised image or two-theta scan. *High Pressure Res.* **1996**, *14*, 235−248.

(29) Yang, X.; Juhas, P.; Farrow, C. L.; Billinge, S. J. L. *xPDFsuite: an end-to-end software solution for high throughput pair distribution function transformation, visualization and analysis*; 2014.

(30) Toby, B. H.; Von Dreele, R. B. *GSAS-II*: the genesis of a modern open-source all purpose crystallography software package. *J. Appl. Crystallogr.* **2013**, *46*, 544−549.

(31) Farrow, C. L.; Juhas, P.; Liu, J. W.; Bryndin, D.; Božin, E. S.; Bloch, J.; Proffen, T.; Billinge, S. J. L. PDFfit2 and PDFgui: computer programs for studying nanostructure in crystals. *J. Phys.: Condens. Matter* **2007**, *19*, 335219.

(32) Giannozzi, P.; et al. QUANTUM ESPRESSO: a modular and open-source software project for quantum simulations of materials. *J. Phys.: Condens. Matter* **2009**, *21*, 395502.

(33) Perdew, J. P.; Burke, K.; Ernzerhof, M. Generalized Gradient Approximation Made Simple. *Phys. Rev. Lett.* **1996**, *77*, 3865−3868.

(34) Blöchl, P. E. Projector augmented-wave method. *Phys. Rev. B: Condens. Matter Mater. Phys.* **1994**, *50*, 17953−17979.
(35) Kresse, G.; Joubert, D. From ultrasoft pseudopotentials to the projector augmented-wave method. *Phys. Rev. B: Condens. Matter Mater. Phys.* **1999**, *59*, 1758−1775.
(36) Cococcioni, M.; de Gironcoli, S. Linear response approach to the calculation of the effective interaction parameters in the LDA + U method. *Phys. Rev. B: Condens. Matter Mater. Phys.* **2005**, *71*, 035105.
(37) Juza, D.; Giegling, D.; Schäfer, H. Über die Vanadinjodide VJ_2 und VJ_3. *Z. Anorg. Allg. Chem.* **1969**, *366*, 121−129.
(38) Berry, K. O.; Smardzewski, R. R.; McCarley, R. E. Vaporization reactions of vanadium iodides and evidence for gaseous vanadium(IV) iodide. *Inorg. Chem.* **1969**, *8*, 1994−1997.
(39) Klemm, W.; Krose, E. Die Kristallstrukturen von $ScCl_3$, $TiCl_3$ und VCl_3. *Z. Anorg. Chem.* **1947**, *253*, 218−225.
(40) Liu, Y.; Petrovic, C. Three-dimensional magnetic critical behavior in CrI_3. *Phys. Rev. B: Condens. Matter Mater. Phys.* **2018**, *97*, 014420.
(41) He, J.; Ma, S.; Lyu, P.; Nachtigall, P. Unusual Dirac half-metallicity with intrinsic ferromagnetism in vanadium trihalide monolayers. *J. Mater. Chem. C* **2016**, *4*, 2518−2526.
(42) Wang, Y.-P.; Long, M.-Q. Electronic and magnetic properties of van der Waals ferromagnetic semiconductor VI_3. *Phys. Rev. B: Condens. Matter Mater. Phys.* **2020**, *101*, 024411.
(43) Li, Y.; Liu, Y.; Wang, C.; Wang, J.; Xu, Y.; Duan, W. Electrically tunable valleytronics in quantum anomalous Hall insulating transition metal trihalides. *Phys. Rev. B: Condens. Matter Mater. Phys.* **2018**, *98*, 201407.
(44) Lazarević, N.; Popović, Z. V.; Hu, R.; Petrovic, C. Evidence for electron-phonon interaction in $Fe_{1-x}M_xSb_2$ (M = Co and Cr $0 \leq x \leq 0.5$) single crystals. *Phys. Rev. B: Condens. Matter Mater. Phys.* **2010**, *81*, 144302.
(45) Baum, A.; Milosavljević, A.; Lazarević, N.; Radonjić, M. M.; Nikolić, B.; Mitschek, M.; Maranloo, Z. I.; Šćepanović, M.; Grujić-Brojčin, M.; Stojilović, N.; Opel, M.; Wang, A.; Petrovic, C.; Popović, Z. V.; Hackl, R. Phonon anomalies in FeS. *Phys. Rev. B: Condens. Matter Mater. Phys.* **2018**, *97*, 054306.
(46) Milosavljević, A.; Šolajic, A.; Pešić, J.; Liu, Y.; Petrovic, C.; Lazarević, N.; Popović, Z. V. Evidence of spin-phonon coupling in $CrSiTe_3$. *Phys. Rev. B: Condens. Matter Mater. Phys.* **2018**, *98*, 104306.
(47) McCarty, K. F.; Radousky, H. B.; Hinks, D. G.; Zheng, Y.; Mitchell, A. W.; Folkerts, T. J.; Shelton, R. N. Electron-phonon coupling in superconducting $Ba_{0.6}K_{0.4}BiO_3$: A Raman scattering study. *Phys. Rev. B: Condens. Matter Mater. Phys.* **1989**, *40*, 2662−2665.
(48) Proffen, T.; Page, K. L.; McLain, S. E.; Clausen, B.; Darling, T. W.; TenCate, J. A.; Lee, S.-Y.; Ustundag, E. Atomic pair distribution function analysis of materials containing crystalline and amorphous phases. *Z. Kristallogr.* **2005**, *220*, 1002−1008.
(49) Bordet, P. Application of the pair distribution function analysis for the study of cultural heritage materials. *C. R. Phys.* **2018**, *19*, 561−574.
(50) Bozin, E. S.; Yin, W. G.; Koch, R. J.; Abeykoon, M.; Hor, Y. S.; Zheng, H.; Lei, H. C.; Petrovic, C.; Mitchell, J. F.; Billinge, S. J. L. Local orbital degeneracy lifting as a precursor to an orbital-selective Peierls transition. *Nat. Commun.* **2019**, *10*, 3638.
(51) Egami, T.; Billinge, S. J. L. *Underneath the Bragg Peaks: Structural Analysis of Complex Materials*; 2003; p 16.
(52) Jin, F.; Lazarević, N.; Liu, C.; Ji, J.; Wang, Y.; He, S.; Lei, H.; Petrovic, C.; Yu, R.; Popović, Z. V.; Zhang, Q. Phonon anomalies and magnetic excitations in $BaFe_2Se_2O$. *Phys. Rev. B: Condens. Matter Mater. Phys.* **2019**, *99*, 144419.
(53) Moskovits, M.; Dilella, D. Surface-enhanced Raman spectroscopy of benzene and benzene-d6 adsorbed on silver. *J. Chem. Phys.* **1980**, *73*, 6068−6075.
(54) Dubroka, A.; Humlíček, J.; Abrashev, M. V.; Popović, Z. V.; Sapiña, F.; Cantarero, A. Raman and infrared studies of $La_{1-y}Sr_yMn_{1-x}M_xO_3$ (M = Cr,Co,Cu,Zn,Sc or Ga): Oxygen disorder and local vibrational modes. *Phys. Rev. B: Condens. Matter Mater. Phys.* **2006**, *73*, 224401.
(55) Souza Filho, A. G.; Faria, J. L. B.; Guedes, I.; Sasaki, J. M.; Freire, P. T. C.; Freire, V. N.; Mendes Filho, J.; Xavier, M. M.; Cabral, F. A. O.; de Araújo, J. H.; da Costa, J. A. P. Evidence of magnetic polaronic states in $La_{0.70}Sr_{0.30}Mn_{1-x}Fe_xO_3$manganites. *Phys. Rev. B: Condens. Matter Mater. Phys.* **2003**, *67*, 052405.
(56) Lekgoathi, M.; Kock, L. Effect of short and long range order on crystal structure interpretation: Raman and powder X-ray diffraction of $LiPF_6$. *Spectrochim. Acta, Part A* **2016**, *153*, 651−654.
(57) Wolverton, C.; Zunger, A.; Lu, Z.-W. Long-versus short-range order in Ni_3V and Pd_3V alloys. *Phys. Rev. B: Condens. Matter Mater. Phys.* **1994**, *49*, 16058.
(58) Webster, L.; Liang, L.; Yan, J.-A. Distinct spin-lattice and spin-phonon interactions in monolayer magnetic CrI_3. *Phys. Chem. Chem. Phys.* **2018**, *20*, 23546−23555.

https://dx.doi.org/10.1021/acs.inorgchem.0c02060
Inorg. Chem. XXXX, XXX, XXX−XXX

10-6

Raman Spectroscopy Study on phase transition in CrI_3 single crystals

Sanja Đurđić[1], Andrijana Šolajić[1], Jelena Pešić[1], Maja Šćepanović[1], Y. Liu[2], Andreas Baum[3,4], Čeda Petrović[2], Nenad Lazarević[1], Zoran V. Popović[1,5]
[1]*Institute of Physics, Pregrevica 118, Belgrade, Serbia,* [2]*Brookhaven National Laboratory, Upton, New York 11973-5000, USA,* [3]*Walther Meissner Institut, Bayerische Akademie der Wissenschaften, 85748 Garching, Germany,* [4]*Fakultät für Physik E23, Technische Universität München, 85748 Garching, Germany,* [5]*Serbian Academy of Sciences and Arts, Knez Mihailova 35, 11000 Belgrade, Serbia*

By virtue of their unique properties and the potential for a wide spectrum of applications, such as the development of functional van derWaals heterostructures, CrI_3 among the other two dimensional materials, has received significant attention in the most recent studies on the ferromagnetic semiconductors. In this study we represent the vibrational properties of CrI_3 single crystals investigated using Raman spectroscopy together with the density functional theory (DFT) calculations. Experimental results show that first-order phase transition from the low-temperature ($R\bar{3}$) to the high-temperature ($C2/m$) phase occurs at 180K with no evidence of the two-phase coexistence. All observed modes, in both phases, are in good agreement with DFT calculations.

7-5

Probing subsequent charge density waves in 1T-TaS_2 by inelastic light scattering

S. Djurdjić-Mijin,[1] J. Bekaert,[2] A. Šolajić,[1] J. Pešić,[1] Y. Liu,[3]
M. V. Milosevic, [2] C. Petrovic,[3] N. Lazarević,[1] and Z. V. Popović [1,4]
[1]*Center for Solid State Physics and New Materials, Institute of Physics Belgrade, University of Belgrade, Pregrevica 118, 11080 Belgrade, Serbia,* [2]*Department of Physics, University of Antwerp, Groenenborgerlaan 171, B-2020 Antwerp, Belgium,* [3]*Condensed Matter Physics and Materials Science Department, Brookhaven National Laboratory, Upton, New York 11973-5000, USA,* [4]*Serbian Academy of Sciences and Arts, Knez Mihailova 35, 11000 Belgrade, Serbia*

Two-dimensional layered transition-metal dichalcogenides (TMDs) have attracted attention for over 30 years mostly due to multiple charge-density wave (CDW) states that had been observed. Prime candidate is 1T-TaS_2 because of its unique and opulent electronic phase diagram. It experiences various phase transitions at high temperature, starting from the normal metallic to the incommensurate charge-density wave (IC-CDW) phase transition, at T= 554 K. At T=355 K 1T-TaS_2 CDW state changes to nearly-commensurate CDW (NC-CDW) phase, eventually leading to commensurate CDW (C-CDW) phase at approximately T= 180 K. Recent discoveries indicate the possibility of yet another phase transition in 1T-TaS_2 at T= 80 K. The new state is identified as hidden CDW (H-CDW) state, and can be induced using ultra-fast laser pulse. We present a detailed Raman spectroscopy study on CDW transitions. Our data indicate the coexistence of different CDW states, as well as strong electron-phonon interaction in the IC-CDW state. The experimental results presented in this work are supported by density functional theory (DFT) calculations.

The vibrational properties of CrI_3 single crystals

S. Djurdjić-Mijin,[1] A. Šolajić,[1] J. Pešić,[1] M. Šćepanović,[1] Y. Liu,[2] A. Baum,[3,4] C. Petrovic,[2]
N. Lazarević,[1] and Z. V. Popović [1,5]

[1]*Center for Solid State Physics and New Materials, Institute of Physics Belgrade, University of Belgrade,Pregrevica 118, 11080 Belgrade, Serbia*
[2]*Condensed Matter Physics and Materials Science Department, Brookhaven National Laboratory,Upton, New York 11973-5000, USA*
[3]*Walther Meissner Institut, Bayerische Akademie der Wissenschaften, 85748 Garching, Germany*
[4]*Fakultät für Physik E23, Technische Universität München, 85748 Garching, Germany*
[5]*Serbian Academy of Sciences and Arts, Knez Mihailova 35, 11000 Belgrade, Serbia*

Abstract. CrI_3 is a two-dimensional layered material and a ferromagnetic [1] with Curie temperature of 61K [1,2] and first order phase transition that occurs at 220K [3,4]. This class of materials has recently gained a lot of intention due to numerous potential applications. Here we represent our work consisting of both experimental and theoretical Raman scattering study of CrI_3 lattice dynamics. Based on our results we can distinguish two different phases for CrI_3 with monoclinic ($C2/m$) being the high-temperature and rhombohedral ($\bar{R}3$) phase being the low-temperature phase. Abrupt changes to the spectra were found at the first order phase transition which was located at $T_s \approx$ 180 K, lower than in previous studies. In contrast to the prior reports we found no sign of phase coexistence over temperature range exceeding 5 K [5].

REFERENCES

[1] E. Navarro-Moratalla, B. Huang, G. Clark *et al.*, Layer dependent ferromagnetism in a van der Waals crystal down to the monolayer limit, Nature (London) **546**, 270 (2017).
[2] J. F. Dillon, Jr. and C. E. Olson, Magnetization, resonance, and optical properties of the ferromagnet CrI3, J. Appl. Phys. **36**, 1259 (1965).
[3] M. A. McGuire, H. Dixit, V. R. Cooper, and B. C. Sales, Coupling of crystal structure and magnetism in the layered, ferromagnetic insulator CrI3, Chem. Mater. **27**, 612 (2015).
[4] D. T. Larson and E. Kaxiras, Raman Spectrum of CrI3: An *ab initio* study, Phys. Rev. B **98**, 085406 (2018).
[5] S. Djurdjić-Mijin, A. Šolajić, J. Pešić, M. Šćepanović, Y. Liu, A. Baum, C. Petrovic, N. Lazarević, and Z. V. Popović, Lattice dynamics and phase transition in CrI3 single crystals, Phys. Rev. B **98**, 104307 (2018.)

Lattice dynamics and phase transitions in $Fe_{3-x}GeTe_2$

A. Milosavljević[a], A. Šolajić[a], S. Djurdjić Mijin[a], J. Pešić[a], B. Višić[a], Y. Liu[b], C. Petrovic[b], N. Lazarević[a] and Z. V. Popović[c]

[a]*Center for Solid State Physics and New Materials, Institute of Physics Belgrade, University of Belgrade, Pregrevica 118, 11080 Belgrade, Serbia*
[b]*Condensed Matter Physics and Materials Science Department, Brookhaven National Laboratory, Upton, New York 11973-5000, USA*
[c]*Center for Solid State Physics and New Materials, Institute of Physics Belgrade, University of Belgrade, Pregrevica 118, 11080 Belgrade, Serbia and Serbian Academy of Sciences and Arts, Knez Mihailova 35, 11000 Belgrade, Serbia*

Abstract. A new class of magnetic van der Waals bonded materials has recently become of great interest, as a suitable candidates for various applications. Whereas $CrXTe_3$ (X = Si, Ge, Sn) and CrX_3 (X = Cl, Br, I) classes maintain low phase transition temperatures even in a monolayer regime, $Fe_{3-x}GeTe_2$ has a high bulk transition temperature, between 220 and 230 K, making it a promising applicant.

Here we present DFT calculations of lattice dynamics and Raman spectroscopy measurements of the van der Waals bonded ferromagnet $Fe_{3-x}GeTe_2$ [1]. Four out of eight Raman active modes are observed and assigned, in agreement with numerical calculations. The energies and linewidths of the observed modes display an unconventional temperature dependence at about 150 and 220 K, followed by the nonmonotonic evolution of the Raman continuum. Whereas the former can be related to the magnetic phase transition, the origin of the latter anomaly remains an open question.

REFERENCES

1. A. Milosavljević, A. Šolajić, S. Djurdjić-Mijin, J. Pešić, B. Višić, Yu Liu, C. Petrovic, N. Lazarević, and Z. V. Popović. "Lattice dynamics and phase transitions in $Fe_{3-x}GeTe_2$." Physical Review B 99, no. 21 (2019): 214304.

Република Србија
Универзитет у Београду
Физички факултет
Број индекса: 2018/8017
Датум: 08.10.2021.

На основу члана 29. Закона о општем управном поступку и службене евиденције издаје се

УВЕРЕЊЕ О ПОЛОЖЕНИМ ИСПИТИМА

Сања Ђурђић Мијин, име једног родитеља Горан, рођена 29.09.1993. године, Београд, Савски венац, Република Србија, уписана школске 2018/2019. године на докторске академске студије, школске 2020/2021. године уписана на статус финансирање из буџета, студијски програм Физика, током студија положила је испите из следећих предмета:

Р.бр.	Шифра	Назив предмета	Оцена	ЕСПБ	Фонд часова**	Датум
1.	ДС15КМ3	Методе квантне теорије поља у физици кондензоване материје	10 (десет)	15	I:(8+0+0)	06.02.2019.
2.	ДС15КМ1	Спектроскопске технике у физици кондензоване материје	10 (десет)	15	I:(8+0+0)	10.09.2019.
3.	ДС15ФРНД1	Рад на докторату 1. део	П.	30	I:(0+0+12) II:(0+0+12)	
4.	ДС15ПФ4	Луминесцентне појаве у танким филмовима	10 (десет)	15	III:(8+0+0)	22.06.2020.
5.	ДС15ПФ7	Пројектовање оптичких система	10 (десет)	15	III:(8+0+0)	24.09.2020.
6.	ДС15ФРНД2	Рад на докторату 2. део	П.	30	III:(0+0+12) IV:(0+0+12)	
7.	ДС15ФРНД4	Рад на докторату 4. део	П.	15	I:(0+0+20)	
8.	ДС15ФРНД3	Рад на докторату 3. део	П.	15	V:(0+0+20)	

* - еквивалентиран/признат испит.
** - Фонд часова је у формату (предавања+вежбе+остало).

Општи успех: 10,00 (десет и 00/100) , по годинама студија (10,00, 10,00, /).

Овлашћено лице факултета

Република Србија
Универзитет у Београду
Физички факултет
Д.Бр.2018/8017
Датум: 08.10.2021. године

На основу члана 161 Закона о општем управном поступку и службене евиденције издаје се

УВЕРЕЊЕ

Ђурђић Мијин (Горан) Сања, бр. индекса 2018/8017, рођена 29.09.1993. године, Београд, Савски венац, Република Србија, уписана школске 2020/2021. године, у статусу: финансирање из буџета; тип студија: докторске академске студије; студијски програм: Физика.

Према Статуту факултета студије трају (број година): три.
Рок за завршетак студија: у двоструком трајању студија.

Ово се уверење може употребити за регулисање војне обавезе, издавање визе, права на дечији додатак, породичне пензије, инвалидског додатка, добијања здравствене књижице, легитимације за повлашћену вожњу и стипендије.

Овлашћено лице факултета

Република Србија
Универзитет у Београду
Физички факултет
Д.Бр.2018/8017
Датум: 08.10.2021. године

На основу члана 161 Закона о општем управном поступку и службене евиденције издаје се

УВЕРЕЊЕ

Ђурђић Мијин (Горан) Сања, бр. индекса 2018/8017, рођена 29.09.1993. године, Београд, Савски венац, Република Србија, уписана школске 2020/2021. године, у статусу: финансирање из буџета; тип студија: докторске академске студије; студијски програм: Физика.

Према Статуту факултета студије трају (број година): три.
Рок за завршетак студија: у двоструком трајању студија.

Ово се уверење може употребити за регулисање војне обавезе, издавање визе, права на дечији додатак, породичне пензије, инвалидског додатка, добијања здравствене књижице, легитимације за повлашћену вожњу и стипендије.

Овлашћено лице факултета

УНИВЕРЗИТЕТ У БЕОГРАДУ ФИЗИЧКИ ФАКУЛТЕТ
UNIVERSITY OF BELGRADE FACULTY OF PHYSICS
Студентски трг 12, 11000 Београд, П.П. 44, Тел: 011-7158-151, Факс: 011-3282-619
Studentski trg 12, 11000 Belgrade, Serbia, POB 44, Tel: +381-11-7158-151, Fax: +381-11-3282-619
www.ff.bg.ac.rs e-mail: *dekanat@ff.bg.ac.rs*

Број 2292016
Београд, 05. 09. 2016. године

На основу члана 161. Закона о општем управном поступку и члана 4. Правилника о садржају и облику образаца јавних исправа које издају више школе, факултети и универзитети, по захтеву, Ђурђић (Горан) Сање издаје се следеће

У В Е Р Е Њ Е

ЂУРЂИЋ (ГОРАН) САЊА рођен- а 29. 09. 1993. године у Београду, Савски венац, Република Србија уписан-а школске 2012/2013. године на четворогодишње основне академске студије, Студијски програм: **Примењена и компјутерска физика**, положио-ла је испите предвиђене наставним планом и програмом и завршио-ла студије на Физичком факултету 15. јула 2016. године, са средњом оценом 9,57 (девет и 57/100) у току студија и постигнутим укупним бројем 242 ЕСПБ (двестачетрдесетдва ЕСП бодова) и тиме стекао-ла високу стручну спрему и стручни назив

ДИПЛОМИРАНИ ФИЗИЧАР

Уверење се издаје на лични захтев, а служи као доказ о завршеној високој стручној спреми до издавања дипломе.

Д Е К А Н
ФИЗИЧКОГ ФАКУЛТЕТА

Проф. др Јаблан Дојчиловић

С. Маскић

Универзитет у Београду
Физички факултет
Број индекса: 2016/7038
Број: 2202017
Датум: 10.07.2017.

На основу члана 161 Закона о општем управном поступку ("Службени лист СРЈ", бр. 33/97, 31/2001 и "Службени гласник РС", бр. 30/2010) и службене евиденције, Универзитет у Београду - Физички факултет, издаје

У В Е Р Е Њ Е

Сања Ђурђић

име једног родитеља Горан, ЈМБГ 2909993715064, рођена 29.09.1993. године, Београд, општина Београд-Савски Венац, Република Србија, уписана школске 2016/17. године, дана 05.07.2017. године завршила је мастер академске студије на студијском програму Теоријска и експериментална физика, у трајању од једне године, обима 60 (шездесет) ЕСПБ бодова, са просечном оценом 10,00 (десет и 00/100).

На основу наведеног издаје јој се ово уверење о стеченом високом образовању и академском називу **мастер физичар.**

Декан

Проф. др Јаблан Дојчиловић

ДОКТОРСКЕ СТУДИЈЕ

ПРЕДЛОГ ТЕМЕ ДОКТОРСКЕ ДИСЕРТАЦИЈЕ КОЛЕГИЈУМУ ДОКТОРСКИХ СТУДИЈА

Школска година 2020/2021

Подаци о студенту

Име	Sanja
Презиме	Đurđić Mijin
Број индекса	8017/2018

Научна област дисертације: Fizika kondenzovane materije

Подаци о ментору докторске дисертације

Име	Nenad
Презиме	Lazarević

Научна област	Fizika kondenzovane materije
Звање	Viši naučni saradnik
Институција	Institut za fiziku

Предлог теме докторске дисертације

Наслов

Neelastično rasejanje svetlosti na kvazi-2D materijalima

Уз пријаву теме докторске дисертације Колегијуму докторских студија, потребно је приложити следећа документа:

1. Семинарски рад (дужине до 10 страница)
2. Кратку стручну биографију писану у трећем лицу једнине
3. Фотокопију индекса са докторских студија

Потпис ментора

Датум 06.07.2021.

Потпис студента

Мишљење Колегијума докторских студија

Након образложења теме докторске дисертације Колегијум докторских студија је тему

прихватио

није прихватио ☒

Датум

29.09.2021

Продекан за науку Физичког факултета